CHAPTER 4

Effect of Material Ductility on Restrained Volume Change Induced Cracking and Interfacial Delamination

Starting with this Chapter, the focus will shift from "material engineering" to "repair system durability assessment", as shown in the middle triangle in Figure 1.10. This chapter addresses one of the major durability concerns in concrete repairs, i.e. repair cracking and repair/old interfacial delamination due to restrained volume change and lack of dimensional compatibility. To begin, the causes and effects of typical concrete deterioration processes will be discussed. Cracking, especially, is the biggest single factor affecting the durability of concrete repair because it often initiates a repair deterioration process and causes premature repair deterioration. Experimental studies were carried out to characterize free drying shrinkage properties of HES-ECC at various RHs, and to determine its restrained shrinkage cracking properties using the steel ring test. Furthermore, in order to fully understand the interaction between the repair and concrete substrate, experimental, numerical and analytical studies were conducted on a simulated repair system subjected to drying shrinkage. The influence of repair material ductility, as

well as substrate surface preparation, on the performance of the repaired system was identified. This research departs from the traditional emphasis on isolated repair material properties testing, and moves toward the age-dependent interaction between the new repair and old concrete. This research proposes and demonstrates, on a laboratory scale, a new repair technology that relies on the repair material's ductility and dimensional compatibility with existing concrete to minimize cracking and interfacial delamination.

4.1 Introduction

Concrete repair is a complex process with unique challenges that differ from those associated with new concrete construction, as discussed in Chapter 1. The durability of a concrete repair depends, to a large degree, on the correct choice and application of repair materials[1]. The concrete repair must successfully integrate new materials with existing concrete to form a composite system capable of resisting service loads and various environmental factors.

Concrete repair failure results from a combination of physical, chemical and mechanical processes, as illustrated in Figure 4.1. Generally the repair deterioration process starts with cracking and repair/old interfacial delamination due to restrained volume change such as drying shrinkage or thermal deformation, when there exists a dimensional incompatibility between the repair and existing concrete. Cracking and delamination are insidious causes of many repair durability problems[2,3,4,5]. The presence of cracks dramatically alters the transport properties of the repair material[6,7,8,9,10,11], facilitates the ingress of aggressive agents into the repaired system, and eventually causes premature deterioration and repair failure such as corrosion and disintegration. Large

cracks accelerate chloride penetration into the concrete and initiate corrosion of reinforcements, especially in regions where deicing salts are applied in winter or in marine environments[12,13]. Corrosion damage has even been observed on epoxy coated reinforcing bars in bridge decks with such cracks[14,15]. In overlay repair applications, delamination of concrete bridge overlays from the substrate deck is one of two primary causes of ultimate overlay failure[16]. The loss of structural integrity impairs load transfer between the repair and old concrete structure. Both cracking and interfacial delamination caused by restrained volume change can reduce the durability and load-carrying capacity of the repaired structure.

The ability of the repair material to withstand restrained volume change without cracking and interfacial delamination depends on the dimensional compatibility between the repair material and existing concrete[17,18,19,20,21]. Table 4.1 lists the properties generally required of patch repair material to achieve structural compatibility[2,22]. Among these properties, dimensional compatibility includes strain capacity, drying shrinkage, coefficient of thermal expansion, creep, modulus of elasticity, and Poisson's ratio. An ideal repair material should undergo zero shrinkage, and have the same amount of thermal deformation, creep, modulus of elasticity and Poisson's ratio as the existing surrounding concrete. However in reality, shrinkage always takes place in a new repair as soon as it is installed, and is considered as the most adverse factor[3,4,5,23,24,25,26,27,28] among those described above that promotes dimensional incompatibility of cement-based repair materials.

The shrinkage of a newly installed repair is immediately restrained by the substrate old concrete, which already underwent shrinkage years ago. Consequently,

tensile stress is developed in the repair layer, and a combination of tensile and shear stresses are built up along the interface between the repair and the concrete substrate. As schematically illustrated in Figure 4.2, tensile stress at the repair/substrate interface is the y-direction stress that opens the interface (delaminates the interface in the y-direction). Shear stress at the repair/substrate interface is the x-direction stress that causes the repair layer to slide along the surface of the substrate (delaminates the interface in the x-direction). These stresses can cause repair surface cracking, and/or interface delamination (Figure 4.2).

A detailed discussion of stress distribution and failure mechanism in a concrete repair system undergoing drying shrinkage can be found in Wittmann and Martinola, 2003[29]. The immediate moisture loss of the cementitious repair material through its exposed surface results in moisture gradients along the repair cross section normal to the exposed repair surface. The highest tensile stresses occur in the exposed repair surface where the moisture gradients are at a maximum, and the tensile stresses increase as the drying process proceeds. Depending on the repair material properties and the severity of the moisture gradients, the maximum tensile stresses can easily surpass the tensile strength (or the maximum tensile strains surpass the tensile strain capacity) of the repair material. As a result, cracks will first occur at the repair surface, and propagate further down through the repair cross section as the drying process proceeds. Simultaneously, the surface crack enlarges. The moisture gradients will also result in the tendency of warping of the repair layer at both ends, causing a combination of tensile and shear stresses at the repair/old interface and potential repair delamination.

It should also be noted that the interaction between the new repair and the existing concrete is a time-dependent process[30,31]. Repair material shrinkage, creep, elastic modulus, tensile strength, and the repair/old interfacial bond are all age-dependent properties, and develop at different rates once the new repair is installed. Cracking and interfacial debonding time and extent are determined by competition among these age-dependent parameters.

In the past decades, there have been significant efforts on reducing repair shrinkage cracking through improving repair material properties such as: (a) reducing material free shrinkage, (b) increasing compressive/tensile strength, and (c) enhancing its bond strength with concrete. Reduced cement-based repair material shrinkage is often achieved by using shrinkage control admixture, expansive cement, short random fibers, lower water/cement ratio, proper and thorough compaction to eliminate air bubbles, large coarse aggregates, or fly ash. In terms of the curing and construction methods, an earlier and longer curing time, the use of sprayed liquid aliphatic alcohol as an evaporation retardant onto the repair surface upon finishing, the use of effective curing procedures including the application of a single pack, membrane (thick) liquid ready-to-use curing compound, and early (sometimes within 8 hours) saw cutting of joints, are important procedures in reducing shrinkage cracking. Increased compressive/tensile strength of cement-based repair materials, e.g. high strength concrete, is typically achieved through a very dense microstructure by employing low water/cement ratios[32], silica fume and fly ash[33], and a well-graded particle size distribution[34].

These efforts, although meaningful, have resulted in only marginal improvements. Cracking due to restrained volume change is still a prevalent phenomenon, and remains

as a big challenge to the repair industry. For example, high strength concrete is particularly more susceptible to cracking due to its high brittleness, high elastic modulus, and small creep deformation[35]. Secondly, containing more finely ground particles than regular concrete, high strength concrete typically has increased autogeneous shrinkage and thermal volume changes. Finally, increasing repair material strength might delay repair cracking, as long as the restrained shrinkage induced tensile stress remains below the material tensile strength over time. However, it poses an elevated risk of interfacial debonding because higher levels of shear and tensile stress build-up at the new/repair interface, which otherwise could have been relieved through cracking in the repair layer. On the other hand, accelerating interfacial bond development may delay the debonding process, but makes the repair more prone to cracking because debonding reduces the level of constraints and partially relieves the tensile stress in the repair. Reducing repair material shrinkage appears to be the most effective method. However, most efforts can only reduce the shrinkage to slightly below 0.01%. This puts a significant demand on the tensile capacity (about 0.01%) for most of the currently available concrete repair materials. In reality, shrinkage is not the only factor that contributes to the deformation of the concrete repair. When thermal effects, structural loading, and other factors are combined, it is highly possible that the total imposed deformation of the repair will surpass its deformation capacity, and cracking and/or debonding will inevitably follow.

The limitations in current approaches to reducing concrete repair failure are that they do not fundamentally address the inherent brittleness of concrete materials. With such brittleness, the potential of preventing cracking by reducing concrete volume change to a level less than the material's deformation capacity is low and unreliable[5,36,37]. These

shortcomings point to an urgent need for developing a new material technology that effectively reduces the cracking potential through removal of material brittleness, and eventually eliminates restrained volume change induced cracking and interfacial delamination in concrete repairs.

4.2 Proposed Approach

To ensure dimensional compatibility within the repaired system, the repair material should possess deformation capacity that fully accommodates the imposed deformation due to a combination of factors, without debonding or fracturing locally. These criteria should be satisfied at all ages throughout the repair's life. In this sense, a repair material can be considered truly dimensionally compatible with existing concrete if the following characteristics are satisfied at all ages: (a) high tensile train capacity, (b) adequate bonding with concrete, (c) similar thermal coefficient and creep as concrete, and (d) same or lower elastic modulus as concrete.

Li and Stang[8] illustrated the effect of the inelastic tensile strain capacity of cementitious material on the cracking behavior of a 2-D slab geometry of length L, restrained at both ends. For brittle or quasi-brittle repair material with tension softening behavior, the cracking potential under restrained shrinkage is defined as:

$$p = (\varepsilon_{sh} - (\varepsilon_e + \varepsilon_{cp})) \tag{4.1}$$

where ε_{sh} is the material's shrinkage strain, ε_e is its elastic tensile strain capacity, and ε_{cp} is its tensile creep strain. A high positive value of p signifies a strong potential for cracking due to restrained shrinkage. In this case, a single crack forms in the repair material with crack width w proportional to the cracking potential p

$$w = L((\varepsilon_{sh} - (\varepsilon_e + \varepsilon_{cp}))/(1 - L/2l_{ch}) \quad \text{for } (\varepsilon_e + \varepsilon_{cp}) \le \varepsilon_{sh} \le w_c / L \tag{4.2}$$

$$w = L(\varepsilon_{sh} - \varepsilon_{cp}) \text{ for } \varepsilon_{sh} \ge w_c / L \tag{4.3}$$

where w is crack width, l_{ch} is Hillerborg's material characteristic length[9]:

$$l_{ch} = EG_f / \sigma_t^2 \tag{4.4}$$

The variables E, G_f , σ_t, w_c stand for the material's Young's modulus, fracture energy, tensile strength, and critical crack opening. A linear tension-softening law is assumed where strength retention decreases from σ_t to 0 as the crack width opens from zero to w_c. Equation 4.2 indicates that crack width w depends on the cracking potential p, the degree of brittleness $L/2l_{ch}$, and the repair dimension L[10]. For instance, highly brittle material such as high strength concrete, which has a relatively small characteristic lengths (l_{ch}), is expected to exhibit more severe cracking with larger crack width. Like other brittle concrete or quasi-brittle fiber-reinforced concrete materials, the crack width of high strength concrete will increase with increasing structural dimensions.

For a repair layer, the boundary conditions are different than those described above. Restraints are applied at the base of the slab rather than at the ends. This difference results in a number of distributed cracks along the repair layer instead of one single crack. For most of the repair materials that are brittle, traction-free cracks will open with a crack width proportional to the cracking potential p. Through the formation and free-opening of these surface cracks, stresses formerly built-up in the repair layer and especially at the interface, can be relaxed. By these means, interface delamination tendency is greatly reduced.

Fibers have been used in concrete repairs to control drying shrinkage and service load-related cracking. For tension-softening FRC materials, shrinkage induced stresses

can result in surface cracking similar to concrete. However, since the cracks are not traction-free because they are bridged by fibers, some amount of tensile and shear stresses remain in the repair layer. As a result, interface delamination can be more prominent in FRC repairs than in concrete or mortar repairs. This phenomenon was first observed by Kabele[38] through a numerical study of a similar repair system.

To suppress both repair surface cracking and repair/old interface delamination, the repair material needs to exhibit "inelastic straining" to accommodate its shrinkage deformation, thus relieving the stresses built-up under restrained drying shrinkage conditions. By these means, surface crack width and interface delamination can both be minimized. Inelastic straining in the form of microcrack damage has been demonstrated in newly developed HES-ECC in Chapter 2. This material has been optimized for high inelastic tensile strain capacity ε_i and tight microcrack width at minimum fiber content. For HES-ECC, the cracking potential[10] is modified as

$$p = (\varepsilon_{sh} - (\varepsilon_e + \varepsilon_i + \varepsilon_{cp}) \tag{4.5}$$

The formation of many fine microcracks in HES-ECC can be regarded as inelastic straining on the macroscopic repaired-system-size scale. The large value of ε_i (>3%) for HES-ECC both in early and late ages results in a highly negative cracking potential p in Equation 4.5. A negative cracking potential p indicates that localized fracture due to restrained shrinkage will be inhibited. Instead, the repair material will undergo inelastic straining by developing multiple microcracks with controlled crack width. Therefore, HES-ECC is suggested as a promising material for durable repair jobs by minimizing repair surface cracking and interface delamination.

4.3 Free Shrinkage of HES-ECC

4.3.1 Background

Drying shrinkage refers to the strain caused by the loss of water from the hardened cementitious material[39]. It is a cement paste property; aggregates have a restraining influence on the volume change that takes place within the cement paste. Proposed mechanisms for causes of drying shrinkage of cement paste include: (a) capillary stress, (b) disjoining pressure, and c) surface tension. The importance of these mechanisms depends on the relative humidity (RH).

Capillary Stress

Within a small capillary pore in the hardened concrete cementitious matrix, water is partially under the influence of surface interactions exerted by the pore walls[39]. Therefore, the water cannot evaporate unless RH is lowered by an amount depending on the pore radius (r), given by the Kelvin equation[39]:

$$\ln(RH) = K(\frac{2\gamma}{r}) \tag{4.6}$$

where γ is the surface free energy (surface tension) of the water, and K is a constant with units of (m^3/J).

The Kelvin equation[40] describes the maximum radius of pores that are saturated with water as a function of RH and time t. Pores in a cementitious composite are water saturated even when the water vapor partial pressure is lower than the saturated water vapor partial pressure, due to the effect of capillary condensation. As illustrated in Figure 4.3, at and below 40% RH all pores are empty according to the Kelvin equation due to the fact that no pores with a radius smaller than 1 nm exist in a cementitious material[41]. For RH below 40%, the removal of hydrostatic stress should be accompanied by a

relaxation in the solid and an increase in length. Although such behavior is observed in materials with a rigid skeleton (e.g., porous glass), it is obscured in cement paste by the slower concomitant loss of water from micropores (subsequently discussed).

Disjoining Pressure

Water is adsorbed on the surfaces of C-S-H, and the thickness of the adsorbed water layer increases with increasing humidity. The assembly of colloidal particles in C-S-H attracts adjacent particles through Van der Waals' forces and brings the adjacent surfaces closer. Adsorption of water between C-S-H surfaces creates a disjoining pressure, which is the combination of steric force and electrostatic force. Disjoining pressure increases with increasing relative humidity and thickness of the adsorbed water between particles. Once surpassing the Van der Waals' attractions, it will force the particles apart and result in a dilation of the composite material. During hydration, C-S-H is formed in the dilated state and the micropores are filled with water. Upon first drying, the decreasing disjoining pressure, due to a lowered relative humidity, will cause the particles to be drawn together by the Van der Waals' forces, resulting in a volume decrease. Disjoining pressure is only a significant factor when RH > 40%.

Surface Free Energy

When RH < 40%, capillary stress and disjoining pressure are no longer operating; drying shrinkage is explained by significant changes in surface free energy as the most strongly adsorbed water is removed. The change in solid volume with changing surface energy γ can be described by the Bangham equation:

$$\frac{\Delta l}{l} = k\Delta\gamma \tag{4.7}$$

where $\Delta l/l$ is the observed relative length change, $\Delta\gamma$ is the change in surface free energy during adsorption, and k is a constant. $\Delta\gamma$ is dependent on RH, and can be expressed as[42,43,44]:

$$\Delta\gamma(RH) = -\frac{R \cdot T}{M \cdot A}\int_0^P \frac{u}{P} dP \tag{4.8}$$

Where R is the universal gas constant, T is absolute temperature, M is mol volume of water, A is specific surface area, P is water vapor partial pressure that depends on RH, and u is adsorbed water volume.

Hygral deformation at a given RH can be experimentally measured as the difference between the steady state drying shrinkage value of the dry state, and the steady state drying shrinkage value at the given RH. The total hygral deformation of a cementitious material can be described by the Munich model, which was originally developed for cement paste[45,46], and later found to also work for concrete[47] and an ordinary ECC (M45)[48], whose cementitious matrix contains Portland type I cement, ASTM class F fly ash, and fine silica sand. This model assumes that the capillary stress is approximately independent of RH[49,50]. Therefore, the total hygral deformation can be described as the deformation due to a change in surface energy of C-S-H gel particles, plus the deformation due to the disjoining pressure between C-S-H gel surfaces when RH > 40%.

$$\varepsilon_{hyg,total}(RH) = \varepsilon_{hyg,surface-energy}(RH) + \varepsilon_{hyg,disjoining-pressure}(RH > 40) \tag{4.9}$$

According to Equation 4.7, the first term of Equation 4.9 can be expressed as:

$$\varepsilon_{hyg,surface-energy}(RH) = \lambda \cdot \Delta\gamma(RH) \tag{4.10}$$

where λ is a function of the stiffness of the porous material[51].

The second term of Equation 4.9 can expressed as:

$$\varepsilon_{hyg,disjoining-pressure}(RH_x) = c \cdot (RH_x - RH_{40})^2 + d \cdot (RH_x - RH_{40}),$$

$$for\ RH \geq RH_{40} = 40\% \tag{4.11}$$

where c and d are empirical parameters.

Combining Equations 4.8, 4.9, 4.10, and 4.11, the total hygral deformation can be rewritten as:

$$\varepsilon_{hyg,total} = \lambda \cdot (A \cdot \ln(RH) + B) + c \cdot (RH_x - RH_{40})^2 + d \cdot (RH_x - RH_{40}),$$

when $RH \geq RH_{40} = 40\%$

$$\varepsilon_{hyg,total} = \lambda \cdot (A \cdot \ln(RH) + B),$$

when $RH < RH_{40} = 40\%$ (4.12)

In this study, the total hygral deformation of HES-ECC at different RHs will be experimentally determined to characterize its free drying shrinkage properties. Additionally, by fitting Equation 4.12 to the experimental data, the parametric values of λ, *A, B, c,* and *d* can be determined for the physical model that describes the hygral deformation of HES-ECC.

4.3.2 Materials and Experimental Procedure

HES-ECC and HES-Concrete (control mix) are investigated in this study. Their mixing proportions and mechanical properties are summarized in Table 4.2, 4.3 and 4.4. The HES-Concrete mixture consisted of coarse aggregate (CA) with 10 mm (0.4 in) nominal grain size, Portland type III cement (C), sand (S) and water (W). Superplasticizer (SP) was used to achieve sound workability. Accelerating admixtures (AC) were also included to accelerate the material's strength development and setting

processes. HES-Concrete specimens were tested to have average compressive strength (f_c') of 49.9 MPa (7234 psi) at the age of 7 days, and 54.2 MPa (7860 psi) at the age of 28 days. Under uniaxial tensile loading, HES-Concrete is a brittle material with sudden fracture failure on a single crack plane.

The HES-ECC mixture, developed in Chapter 2, is comprised of Type III Portland cement (C), water (W), silica sand (S) with 110 μm (3.94×10^{-3} in) nominal grain size, polystyrene beads with a size of 4 mm (0.157 in) as aggregates, superplasticizer, accelerating admixtures, and 2% (V_f) polyvinyl-alcohol (PVA) fibers. These PVA fibers had length of 12 mm (0.472 in) and diameter of 40 μm (1.54×10^{-3} in). The HES-ECC is self-consolidating in the fresh state. The polystyrene beads serve as deliberately introduced initial flaws to assist in triggering the multiple microcracks[6] during tensioning of the composite. As measured in Chapter 2, the HES-ECC mixture had average compressive strength of 47.5 MPa (6885 psi) at the age of 7 days, and 55.6 MPa (8063 psi) at the age of 28 days. Its average Young's modulus was 20.6 GPa (2986 ksi) at the age of 7 days, and 23.2 GPa (3365 ksi) at the age of 28 days, which was lower than that of HES-Concrete (26.2 GPa (3803 ksi) at 7 days; 27.8 GPa (4025 ksi) at 28 days) due to the absence of coarse aggregates (CA). A lower modulus repair material is desirable in that it limits the tensile stress induced by restrained drying shrinkage. The HES-ECC mixture also has a tensile strain capacity between 3 – 6% at all ages.

Free drying shrinkage tests were conducted on HES-ECC and HES-Concrete (control) prism specimens with dimensions of 200 mm (7.9 in.) × 40 mm (1.6 in.) × 40 mm (1.6 in.), in accordance with ASTM C157/C157-99 and C596-01[52] standards. The test setup is shown in Figure 4.4. Twenty-one specimens for each mix were cast and

demolded after 24 hours. After storage at 100% relative humidity (RH) for two days, the specimens reached hydral equilibrium. Three specimens of each mix were then stored in RH = 0%, 12%, 33%, 66%, 75%, 85%, and 93% by using saturated salt solutions in different desiccators[53,54]. The drying shrinkage deformation of the HES-ECC specimens was then measured as a function of drying time, until hygral equilibrium was reached. After all specimens had reached hygral equilibrium, the specimens stored at 0% RH were dried in an oven at 105 °C (221 °F) until a constant mass was achieved. The specimens were then removed from the oven and allowed to cool down to room temperature 20±1 °C (66-70 °F). After the specimens reached thermal equilibrium with room temperature, the length changes were determined as the shrinkage values at RH = 0%.

4.3.3 Experimental Results and Discussion

The hygral deformation of HES-ECC and HES-Concrete is calculated as the difference between the steady state drying shrinkage value in the dry state (0% RH) and the steady state drying shrinkage value at specific RHs. These data are plotted as a function of RH in Figure 4.5, together with the measured hygral deformation values of an ordinary ECC (ECC 45) and a concrete mix (both are Portland type I cement based) from Weimann and Li, 2003[48]. The parametric values of HES-ECC, HES-Concrete, ordinary ECC and concrete[48] are summarized in Table 4.5. The good fit between theoretical (Equation 4.12) and experimental data demonstrated that the drying shrinkage of HES-ECC can be explained by the contraction due to the increase in surface free energy of C-S-H particles, as well as the decrease in disjoining pressure between the surfaces of C-S-H, the latter mechanism only operating above 40% RH. These results clarified that the

drying shrinkage behavior of HES-ECC is governed by the same mechanisms as concrete materials and Type I cement based ECC M45.

The experimental results reveal that the drying shrinkage of HES-ECC is approximately twice that of the HES-Concrete control mix, and 15% higher than the ordinary ECC. This is due to the very high cement content, finer cement particles, and absence of large volume of coarse aggregates and fly ash in the HES-ECC mix. Nonetheless, Figure 4.5 shows that the shrinkage strain of HES-ECC is below 0.3%, which is one order of magnitude lower than its tensile strain capacity 3-6%. This implies that when the drying shrinkage of HES-ECC is restrained, the material's ductility can accommodate shrinkage deformation by forming multiple microcracks at its strain hardening stage without localized fracture failure. Once microcracked, the effective modulus of the HES-ECC will be substantially reduced, as seen in the reduced slope of the tensile stress-strain curve in the strain-hardening stage (Figure 2.27), thus further suppressing tensile stress build-up in the repair material due to continued restrained shrinkage. This predicted behavior is verified in further experimental studies where HES-ECC drying shrinkage deformation is restrained. These investigations are described in the next sections.

4.4 Restrained Shrinkage Ring Test

4.4.1 Materials and Experimental Procedure

Due to its simplicity and versatility, the ring test has become often used over the last two decades to measure restrained shrinkage cracking of concrete materials and fiber reinforced cementitious composites[55,56,57]. It was adopted in this study to

investigate the number and width of shrinkage-induced cracks in HES-ECC compared to a control HES-Concrete with the mixing proportion shown in Table 4.2.

The restrained shrinkage ring test followed AASHTO[58] PP-34. Figure 4.6 shows the test set-up and specimen dimensions. For each specimen, a 25.4 mm (1 in.) thick layer of HES-ECC or HES-Concrete material was cast around a rigid steel ring. A plastic covered paper cylinder was used as an outer mold during casting. The outer mold was removed 6 hours after casting and the specimen was then exposed to 45 ± 5% RH and 20±1 °C (66-70 °F). It should be noted that the curing conditions for the ring tests are different from the free drying shrinkage test, which was described earlier in Section 4.3. The purpose of the early demolding and short (6 hours) curing time in the ring tests is to simulate the early re-opening conditions in field application, while the free shrinkage tests employ curing conditions based on the ASTM C157/C157-99 and C596-01 standards to characterize HES-ECC shrinkage strain at various RHs.

Once exposed to the ambient relative humidity and temperature conditions, the drying shrinkage deformation of the HES-ECC and HES-Concrete, when restrained by the steel ring, results in internal radial pressure. Consequently, the HES-ECC and HES-Concrete layers are subjected to a circumferential tensile stress state that can cause cracking. The cracking pattern, crack number and crack width were measured as a function of age with a portable microscope. Measurements were taken at three different locations along each crack and the average value was plotted. Three HES-ECC and three HES-Concrete specimens were tested.

4.4.2 Experimental Results and Discussion

Test results are summarized in Table 4.6 and Figure 4.7. For the three HES-Concrete control specimens, one localized crack was observed in each specimen. The average crack width of the three specimens was 310μm (0.012214 in.) at 2 days, 610 μm (0.024034 in.) at 4 days, 1210 μm (0.047674 in.) at 28 days and 1250 μm (0.049250 in.) at 60 days. For each of the three HES-ECC specimens, 25, 23, and 19 cracks were formed at 60 days, respectively. The average crack width was 40 μm (0.001576 in.) at 2 days, and remained at 50 μm (0.00197 in.) for the remaining 2 day to 60 day test period. The crack width of these HES-ECC microcracks was significantly lower than the crack width of HES-Concrete localized cracks, and the former retains its load carrying capacity after crack formation. Wang et al.[59] reported that as crack width increases from 100 μm to 500 μm, the permeability coefficient increases nearly seven orders of magnitudes from 1.0×10^{-11} m/sec to 1.0×10^{-4} m/sec. However, for crack widths under 100 μm, the permeability coefficient remains nearly identical to that of uncracked concrete, suggesting that for crack widths below this threshold there is no significant increase in permeability after cracking. The test results show that HES-ECC has significantly greater resistance to restrained shrinkage cracking than HES-Concrete, despite its higher free (drying) shrinkage value. This is due to the negative shrinkage cracking potential of HES-ECC, in contrast to the positive shrinkage cracking potential of HES-Concrete. This point will be discussed in detail in the next section.

The shrinkage deformation process in HES-ECC occurs during the strain-hardening stage, and the shrinkage crack width is an intrinsic material property independent of structural dimensions or the reinforcement ratio. Additionally, the

shrinkage crack width of HES-ECC becomes independent of age (drying time) once the material enters the strain-hardening stage. Further shrinkage deformation of HES-ECC will be accommodated by forming more microcracks with controlled crack width under 50 μm (0.00197 in.), instead of increasing the width of existing cracks (Figure 4.7). In contrast, continued shrinkage deformation of HES-Concrete with age is accommodated by forming of localized cracks with increasing crack width. The crack width of HES-Concrete is not only related to age (drying time), but also highly depends on structural dimensions – larger repair members tend to have larger shrinkage deformation that needs to be accommodated by crack opening, as experimentally demonstrated by Li and Stang (2004). Thus, while the restrained shrinkage tests in this study demonstrate a 25 fold reduction in the 60-day shrinkage crack width in HES-ECC compared with that in HES-Concrete, the advantage of ECC can be even more significant in field repair applications.

4.5 Restrained Shrinkage Test on a Simulated Repair System

The lack of widely agreed upon testing methods leaves repair materials subject to limited evaluations driven by manufacturers rather than by users[5]. Frequently, only the isolated properties of repair materials are emphasized, whereas the more important properties of the composite system are neglected. In this study, the restrained shrinkage test was conducted on a simulated repair system, which contains one layer of old concrete substrate and one layer of new repair material to simulate real repair conditions. The performance of the composite repair system as well as the interaction between the repair and concrete substrate were investigated.

4.5.1 Materials

Three different repair materials — HES-Concrete, HES-Steel Fiber Reinforced Concrete (HES-SFRC) with tension softening stress-strain curve, and HES-ECC – were investigated in this study. The HES-Concrete and HES-SFRC were employed as controls. All three materials use Portland type III cement to achieve high early strength. Their mixing proportions are summarized in Table 4.2. Six specimens of each mix were tested to achieve the material mechanical properties reported in Table 4.3.

The HES-Concrete and HES-ECC mixes were the same as those investigated in the free shrinkage test and restrained shrinkage ring test. The HES-SFRC mix had the same composition as HES-Concrete, except that it contained 1% (V_f, volume fraction) steel fibers. The steel fiber, with length of 30 mm (1.18 in) and diameter of 0.5 mm (0.02 in), had a smooth surface and hooked ends. The averaged 7-day and 28-day compressive strength of the HES-SFRC specimens were 51.5 MPa (7462 psi) and 56.9 MPa (8254 psi). Under tensile loading, HES-SFRC is a quasi-brittle material with a tension softening stress-strain response. The ultimate tensile strain capacity (ε_u) of both HES-Concrete and HES-SFRC is around 0.01%. The substrate concrete has the same material composition, except that it used ordinary concrete containing Portland type I cement while the HES-Concrete repair used Portland type III cement.

4.5.2 Repair Specimen Configuration and Surface Preparation

In this study, layered repair systems were experimentally investigated with the three types of repair materials described above; HES-Concrete, HES-SFRC and HES-ECC. Concrete substrates were initially cast with dimensions of 1600 mm × 100 mm ×

100 mm (63"× 4"× 4"), as shown in Figure 4.8. They were moisture-cured until the age of 28 days, and then left to dry in ambient conditions for an additional 150 days before the repair layers were placed. The additional 150 days allowed for any potential shrinkage in the substrates to occur before bonding the repairs. This procedure was followed to simulate the actual repair conditions of actual repair of old concrete structures.

The contact surfaces of the concrete substrates were roughened while the material was still in a fresh state by using a chisel to remove slurry cement from the external surfaces of coarse aggregates. The estimated roughness amplitude was 3.8 mm to 5.1 mm (0.15 to 0.20 in). Before placing the repair layer, the substrate surface was re-cleaned with a brush and high-pressure air to ensure a clean bonding surface, and was then dampened with water fog. The moisture level of the contact surface was critical to achieve bonding; excessive moisture in a contact surface may clog the pores and prevent absorption of the repair material. On the other hand, an overly dry substrate contact surface may absorb water from the repair material, resulting in an undesirable magnitude of shrinkage[60]. After dampening the surface, a 50 mm (2 in.)-thick repair layer made of each of the three repair materials was cast on top of the concrete substrate. The repair layers were moisture cured for 6 hours and then demolded. After demolding, the layered specimens were moved into a room with ambient conditions of 45 ± 5% RH and 20±1 °C (66-70 °F).

For each specimen, two dial gauges (Figure 4.8) were used to record the interface vertical separation distance at the ends of the specimens as a function of drying time after delamination began. Additionally, a portable microscope was used to measure the

delamination at 30 different locations along the interface, from which the delamination crack profile was derived. The microscope was also employed to observe crack pattern, crack number and crack width of the top surface of the repair layer, as a function of age. Both delamination and surface cracking were measured daily.

Free shrinkage testing was also carried out in order to measure the free shrinkage strain of the HES-Concrete, HES-SFRC and HES-ECC mixtures for the calculation of cracking potential p. The free shrinkage test specimens were made from the same batch as the repair layer mix for each of the three repair materials. Differing from the free shrinkage test in Section 4.3, these specimens were domolded as early as after 6 hours, and shrinkage began. The testing environment of the specimens were also modified to be the same as the layered repair specimens, with ambient condition of 15-21°C (60-70°F) and 45 ± 5% RH. The same curing, storing and testing environment were used for relating the free shrinkage test results to the observed behavior of the layered specimens.

4.5.3 Experimental Results and Discussion

Cracking Potential of Repair Materials

Three specimens were tested for HES-ECC, HES-Concrete and HES-SFRC and the average free shrinkage strain (ε_{sh}) values are summarized in Figure 4.9. The data show the shrinkage strain of each material at the age of 1d, 3d, 7d, 28d, and 60d. HES-ECC has the highest shrinkage strain value because of higher cement content and the absence of large coarse aggregates, while the HES-SFRC has the lowest shrinkage strain value because of the constraining effect of steel fibers.

The cracking potential p for HES-Concrete, HES-SFRC and HES-ECC can be estimated based on measured values of ε_{sh} and ε_i according to Equation 4.1 and 4.5, and is summarized in Table 4.7. The other parametric values (ε_e and ε_{cp}) were not measured in this study, but were adopted by estimation as the ε_e and ε_{cp} of normal concrete and SFRC from Li[61]. Although HES-ECC had the highest free shrinkage, its negative p-value verifies that it had entered the strain hardening stage under restrained drying shrinkage, and will experience microcracking damage without fracture localization. In contrast, HES-Concrete and HES-SFRC are subject to tensile fracturing due to their positive p-values.

It should be noted that the cracking potential p was calculated assuming a boundary condition that is generally different from what repairs experience within structures. In repair conditions, restraints are applied at the base of the repair and the restraint level might be lower, depending on the stiffness of the substrate, presence of reinforcements, boundary conditions, etc. However, the calculated p values in Table 4.7 provide revealing insight on the significant influence of repair material ductility (inelastic strain capacity) on the repair cracking potential. Most of the currently available concrete repair materials are either quasi-brittle (e.g. concrete) or tension-softening (e.g. fiber reinforced concrete), therefore having an ε_i equal to 0. This means that reducing the free shrinkage ε_{sh} of these materials is not an effective approach to preventing cracking due to restrained volume change, because it can only lower the cracking potential by a minimal amount below zero. When shrinkage is combined with other causes of volume change such as thermal deformation and deformation due to structural loads, very often the total strain imposed on the repair, ε_{total}, leads to a positive cracking potential p.

$$p = (\varepsilon_{total} - (\varepsilon_e + \varepsilon_{cp})) \tag{4.13}$$

This is not the case for a ductile repair material such as HES-ECC, with inelastic strain capacity one order of magnitude higher than its shrinkage strain. The highly negative cracking potential of HES-ECC provides a large safety margin for resisting localized cracking due to restrained volume change.

$$p = (\varepsilon_{total} - (\varepsilon_e + \varepsilon_i + \varepsilon_{cp})) \tag{4.14}$$

Surface Cracking and Interface Delamination of Repaired Systems

Table 4.8 summarizes the surface crack pattern, i.e. crack number and crack width, of the three repaired systems, respectively at the age of 60 days. Three specimens of each repair material were tested. When HES-Concrete was used as the repair material, 3-4 surface cracks localized at the age of 60 days. The maximum crack width observed for the three specimens was 490 μm (19.3×10^{-3} in). When HES-SFRC was used as the repair material, 1-4 localized surface cracks formed, and the maximum crack width of the three specimens was 280 μm (11.0×10^{-3} in). The smaller crack width in the HES-SFRC repair can be attributed to the steel fiber's bridging effect. Note that the restrained shrinkage induced crack width for HES-Concrete or HES-SFRC repair is a structural property, which is dependent on structural dimensions.

In contrast, when HES-ECC was used as the repair material, 83-113 microcracks were formed on the surface of the repair layer, with a maximum crack width of 60 μm (2.36×10^{-3} in) – much narrower than the cracks found in the HES-Concrete and HES-SFRC repairs. The average crack width of the HES-ECC repair was around 30 μm (1.18×10^{-3} in). No localized fracture was observed. The shrinkage strain of HES-ECC

(less than 0.3 %) was far below its tensile strain capacity of 3-6 %. Therefore, the restrained shrinkage cracking of HES-ECC occurred in its strain-hardening stage, during which the material formed multiple microcracks with steady state crack width. In this deformation stage, the restrained shrinkage crack width of the HES-ECC repair was self-controlled, and is a material property independent of structural dimensions. Even for larger scale repair applications with different restraint conditions, HES-ECC repair is still expected to exhibit tight crack width, below 60 μm (2.36×10^{-3} in). This tight crack width should greatly reduce transport of aggressive agents by permeation[10] and chloride penetration[11]. Figure 4.10 shows the surface-cracking pattern of each type of repair layer. HES-Concrete and HES-SFRC repairs exhibited localized fractures, in contrast to the multiple microcracks of HES-ECC repair with significantly smaller crack width.

The measured interface delamination heights and lengths for the nine layered repair specimens are summarized in Table 4.8. As illustrated in Figure 4.11, the delamination height is the distance between the crack faces of the crack running along the repair-substrate boundary, at the two ends of the repaired system; the delamination length is the length of the delaminated section along the long axis of the specimen. At the age of 60 days, both the HES-ECC and the HES-Concrete repaired systems exhibited relatively low delamination heights at the specimen ends, which were a maximum of 80 μm (3.15×10^{-3} in) for the former and 90 μm (3.54×10^{-3} in) for the latter. The maximum delamination length was 80 mm (3.23 in) for the HES-ECC repair and 170 mm (6.69 in) for the HES-Concrete repair. The HES-SFRC repaired system had much larger delamination height than the HES-ECC or HES-Concrete repaired system at the age of 60 days, which was 310 μm (12.2×10^{-3} in). Its delamination length was also larger,

measured to be 340 mm (13.46 in). Figure 4.12 shows the interface delamination profiles of the three repair systems at different ages, which are the vertical displacement/delamination heights of the repair layers at different locations along the repair/substrate interface. These profiles are approximately symmetric about the mid-point of the specimen, as would be expected.

The interface delamination height development of the three repaired systems as a function of time is shown in Figure 4.12. It can be seen that HES-ECC and HES-Concrete repaired systems completed most of their interface delamination at very early ages – within 7 days, when surface cracking had already completed and helped to release tensile and shear stresses at the specimen interface. However, for the SFRC repaired system, delamination behavior continued to evolve for up to 60 days (Figure 4.12), at which time the SFRC repair material had undergone most of its shrinkage (Figure 4.9). This further confirms that the fiber-bridged cracks of HES-SFRC repair could only release a fraction of the stresses at the interface, so that delamination continued along with shrinkage. As can be seen in the figure, the HES-SFRC repair exhibited interface delamination heights several times greater than those of the HES-ECC and HES-Concrete repairs.

4.6 Effects of Surface Preparation on the Repaired System Performance

The same simulated repair system described in Section 4.5 was adopted in this section to investigate the effects of surface preparation (interfacial bond) on repair cracking and interfacial delamination due to restrained drying shrinkage. Three types of repair material were used: concrete (brittle), FRC (tension-softening) and ECC M45

(ductile). These materials do not have the high early-age strength properties, as did the materials investigated in the last section, but still well represent their material categories with respect to specific tensile behavior. This study clarified the influence of surface preparation on the performance of repairs with different tensile behaviors. It also further validated the effects of repair material tensile ductility on the performance of the repaired system. It also further validated the effects of repair material tensile ductility on the performance of repaired system – To prevent restrained shrinkage induced repair cracking and interfacial delamination, it is the tensile properties of the repair material, not any specifically designed mixes, that governs.

4.6.1 Experimental Procedure

Three different type I Portland cement based repair materials — concrete, steel fiber reinforced concrete (SFRC) with tension softening stress-strain curve, and ECC (M45) were investigated in this study. Concrete and SFRC were employed as controls since they have been used in repair applications and included in the ACI Concrete Repair Guide ACI 546R-04[62]. The mix proportion, mechanical properties and shrinkage cracking potentials are summarized in Table 4.9. Experimental details in determining these properties can be found in Li and Li, 2006[31].

The concrete substrate was cast and cured as described in Section 4.5. In this experiment, the surfaces of the concrete substrates were prepared in four different ways: (a) normally cast (smooth); (b) roughened to 4~5mm; (c) roughened to 7~8mm; and (d) roughened to 7~8mm + cement bonding slurry. For case (b), (c) and (d), the substrate surfaces were roughened while in the fresh state by using a chisel to remove slurry

cement from the external surfaces of coarse aggregates. Before placing the repair layers, the substrate surfaces were re-cleaned with a brush and high-pressure air to ensure a clean bonding surface, and then they were damped to an adequate moisture level. After that, repair layers made of each of the three repair materials were cast on top of the concrete substrates. If cement-bonding slurry was used, a thin coating of "creamy" grout was vigorously and thoroughly brushed into the prepared surface immediately before placing the repair material.

The repair layers were moisture cured for 24 hours and then demolded. After demolding, the layered specimens were moved into a room with ambient conditions of 45 ± 5% RH and 20±1 °C (66-70 °F). Both delamination and surface cracking were measured on a daily basis using dial gauges and a portable microscope (Figure 4.8).

4.6.2 Experimental Results and Discussion

Surface cracking and interface delamination of the three types of repair systems are summarized in Table 4.10. The experimental results show that with a normally cast (smooth) substrate surface, concrete, SFRC and ECC repairs all exhibited relatively large delamination heights and lengths. The delamination values (height and length) of the ECC repair were significantly higher than for the other two repair materials, probably due to the large fly ash content in ECC, which leads to lower bonding strength with the concrete substrate at early ages when shrinkage is most significant.

For the concrete repair, enhancing interfacial bonding by roughening the substrate surface and/or adding bonding agent (cement-based slurry) reduced the delamination values. However, the crack pattern did not change and several localized cracks formed

with crack width larger than 100μm. Furthermore, larger crack width was observed as the interfacial bond became stronger. This is explained by the positive cracking potential of concrete, resulting in shrinkage deformation that cannot be accommodated by concrete itself through "yielding". Therefore, the shrinkage deformation must be accommodated by interfacial delamination, repair cracking, or a combination of both to different extents. As a stronger interfacial bond reduces delamination, bigger cracks naturally form in the concrete repair layer to accommodate shrinkage deformation.

For the SFRC repair, no significant changes in interfacial delamination values were observed among the four types of surface preparation. Even with a deeply roughened substrate surface and application of bonding agent, the delamination height and length were still larger than 310μm. This happened because after shrinkage cracks formed in SFRC repair, the cracks were bridged by steel fibers. Unlike the traction-free cracks in the concrete repair, these cracks were not able to open freely to relax the stress built up in the repair layer, and consequently forced the interface to delaminate. This phenomenon dominated the interaction between the SFRC repair and substrate, even when a strong interfacial bond was present.

For the ECC repair with enhanced interfacial bonding, the delamination height and length were significantly reduced, and the multiple cracking phenomenon became more predominant. For the "roughened to 7-8mm" and "roughened to 7-8mm + cement bonding slurry" cases, the ECC repaired system exhibited the most desirable performance, with both crack width and interfacial delamination below 60μm. No localized fracture was observed in the ECC repair layer.

This study further verified the outstanding cracking and delamination resistance of a ductile material repaired system under restrained volume change conditions. When an adequate bond was provided, the ECC repair developed multiple microcracks rather than several localized cracks, which consequently suppressed interfacial delamination under restrained drying shrinkage. Unlike other brittle or quasi-brittle materials, the tight crack width of ECC is a material property, which is independent of structural dimensions. This implies that with increasing structural scale, the advantage of using ECC as a repair material will become even more important.

The bond strength of repair materials with concrete is a requirement of ACI 546R-04[62]. In ACI 546R-04 Section 2.7, in-place tensile pull-off tests are recommended to evaluate the adequacy of the surface preparation and bonding of repair materials. Failure in substrate is preferred, which means that materials having high bonding strength with the old concrete are more likely able to make repairs with sound performance and durability. Experimental results from this study show that sufficient bonding strength is necessary for ECC repair material to fully utilize its tensile ductility to suppress repair cracking and interfacial delamination. However, for brittle or quasi brittle repair materials with large cracking potential values, enhancing interface bonding strength will have a very limited effect on achieving durability in the repaired structure. This can be explained by the time-dependent interaction between the repair and substrate. Once sufficient stresses have been built up in the repaired system due to restrained repair volume change, a stronger bond can reduce the trend of interface delamination, but also promote the tendency of surface cracking, potentially increasing cracking number and/or width. In this sense, special attention needs to be paid when interpreting results from the

pull-off test, because it over-simplifies the interaction between the repair and concrete substrate, and neglects the subtle time-dependent competition between surface cracking and interfacial delamination. Simply seeking a strong bond while ignoring the critical influence of the repair material's tensile ductility on reducing cracking potential cannot fundamentally improve repair durability.

4.7 Numerical Study on the Simulated Repair System

4.7.1 Problem Formulation and FEM Model

A numerical study was carried out to simulate the layered repair specimen by using the finite element program MLS (Multi-Layer Systems) of FEMMASSE (Finite Element Modules for Materials Science and Structural Engineering)[63]. The module MLS can compute the physical and structural behavior of composite structures, taking varying environmental conditions into account.

This numerical study considered a concrete substrate that was repaired by a freshly cast layer of material. The dimensions of the concrete substrate and the repair layer adopted were the same as those of the experimental specimen. The geometry and mechanical boundary conditions of this model are shown in Figure 4.13. The objectives of this numerical study were to simulate the restrained shrinkage induced repair cracking and interfacial delamination process using three types of repair material models (brittle, tension-softening, and strain hardening). The simulation results were used to explain the experimental findings, by providing insights on the time-dependent stress distribution in the repair layer and at the repair/substrate interface.

Three material models were applied, respectively to simulate the three types of repair material: brittle material model – HES-Concrete, tension softening model – HES-SFRC, and strain hardening model – ECC (Figure 4.14). In these models, a bi-linear stress-strain relation was used to describe the elastic straining and strain-hardening response, while a stress-crack opening relation was used to describe the tension-softening response. Note that the parameters of the material models are age-dependent, and were fitted as curves according to experimentally measured results from material of ages 4 h to 28 d. For example, the initial slope of the three curves (the material Young's modulus E) changes with material age according to experimental results, as shown in Table 4.3 and Table 4.4. The tensile strength of HES-ECC from material age of 4 h to 28 d was adopted from the testing results in Table 4.4. The first cracking strength of HES-ECC was assumed to be 80 percent of the ultimate tensile strength. The tensile strength of HES-Concrete and HES-SFRC was assumed to be the same as HES-ECC at different ages. Statistical standard deviation of material tensile strength of the three materials was assumed to be 0.1 in the FEMMASSE FEM model. The tensile strain capacity of HES-ECC was conservatively assumed to be 3% at all ages. Compressive strength of the three materials was adopted from the experimental data in Table 4.3. Poisson's ratios of the three materials were all assumed to be 0.2.

The concrete substrate was assumed to have the same mechanical and fracture properties as the HES-Concrete repair layer. No cracking or shrinkage was considered in the old concrete substrate.

The repair/old interface used the interface type A model in FEMMASE, with the properties listed in Table 4.11 and illustrated in Figure 4.15. No direct measurements

were made of the interface properties, but they were assumed to be the same in all three cases. f_t was assumed to be 4 MPa[38]. FEMMASE type A model default values were used for the other parameters.

In this numerical model, loading derives from the repair layer material drying shrinkage deformation that changed with material age as well. The measured time-dependent shrinkage strain of HES-Concrete, HES-SFRC and HES-ECC shown in Figure 4.9 was used as the input loading for this FEM model.

4.7.2 Numerical Simulation Results

The FEM predicted cracking behavior of the HES-Concrete, HES-SFRC and HES-ECC repairs at the 60-day age is shown in Figure 4.16. It can be seen that the HES-Concrete repair developed several localized cracks with a maximum crack width of 229 μm. The HES-SFRC repair developed more localized cracks, but a smaller maximum crack width of 111 μm. Despite having shrinkage strain nearly twice as high as that of HES-Concrete and HES-SFRC, HES-ECC exhibited saturated cracking behavior with crack width under 46 μm. These results from FEM simulation are quite similar to the experimental results. Although the cracking numbers predicted by the FEM models are not exactly the same as the experimental results due to the unavoidable material variability (e.g. initial flaw sizes), the cracking trends (localized fractures with larger crack width in the HES-Concrete and HES-SFRC repairs and microcracks in the HES-ECC repair) are accurately predicted by the FEM model.

Figure 4.17 shows the tensile stress (σ_{xx}) distribution in the HES-Concrete, HES-SFRC, and HES-ECC repair layers at the age of 60 days. Figure 4.18 shows the

repair/old interface shear stress (σ_{xy}) distribution of the three repaired systems at the age of 60 days. In the HES-Concrete repair, σ_{xx} is zero at the cracking locations because the cracks are traction free. Opening these cracks relieves part of the interface normal and shear stresses, and reduces interface delamination at the ends of repair. However, it can be seen that σ_{xy} remains at a significant level. The tensile component σ_{yy} (not shown) shows a similar trend. This high stress is due to the tendency of the repair elements between the widely separated cracks to shrink while being restrained by the underlying substrate. Therefore, although the HES-Concrete repair exhibited a similar amount of interface delamination as the HES-ECC repair in the experiments, the FEM simulation indicates that the tendency of interface delamination of the HES-Concrete repair is much higher than the HES-ECC repair due to the higher level of interface stresses. In the HES-SFRC repair, σ_{xx} is non-zero at the cracking locations due to tension softening associated with steel fiber bridging. The resulting high interface stresses (Figure 4.18) induce high interface delamination in the HES-SFRC repair.

A significantly different behavior can be observed in the HES-ECC repair. The saturated microcracks of HES-ECC are tight (below 46 μm) and uniformly distributed through the repair layer. After cracking, these microcracks can still carry significant amounts of stress, as seen in Figure 4.17. By developing a large number of microcracks, the HES-ECC repair deformed uniformly in a ductile manner, and relieved the stresses everywhere along the interface. Thus, the shrinkage deformation was accommodated by the "plastic" straining of the ECC repair layer. Figure 4.18 shows that small interface shear stresses (σ_{xy}) (and similarly the tensile stress σ_{yy}, not shown) are almost uniformly distributed along the HES-ECC repair. A small amount of interface delamination exists

only at the repair ends. The repair cracking and interface delamination behavior experimentally measured and numerically predicted in this study are consistent with those numerically modeled by Kabele[38].

4.8 Simplified Analytical Model for the Repair Systems under Restrained Volume Change

An analytical model was developed by Zhou et al[64] to calculate the stresses in the concrete and ECC repairs as well as at their interfaces with concrete substrate due to restrained volume change. For the concrete repair, the model development procedure contains four steps, assuming the restrained volume change is due to differential shrinkage[65] as illustrated in Figure 4.19. Firstly, the repair material is assumed to be unbonded from the substrate concrete. Instead, the shrinkage of the repair material is restrained at the both ends, resulting in a tensile stress

$$\sigma_{sh}(y) = E_r \times \varepsilon_{sh}(y) \tag{4.15}$$

where $\varepsilon_{sh}(y)$ and E_r are the shrinkage and elastic modulus of the repair material. Secondly, the repair material was bonded to the substrate concrete. For the equilibrium of the repair system, a compressive stress $-\sigma_{sh}(y)$ is then applied at the ends of the repair material. This stress is simplified to be constant through the depth of the repair material, which can be written as

$$\sigma_{eq} = -\frac{1}{h_r}\int_{h_r}^{0} E_r \varepsilon_{sh}(y)dy \tag{4.16}$$

where h_r is the thickness of repair material. Thirdly, the stresses and strains in the repair system subjected to the external stress σ_{eq} are calculated based on the plate theory and the assumption of a linear relation between shear stress and slip at the interface. Finally, the

restrained shrinkage stress $\sigma_{sh}(y)$ is superimposed to the stress in the repair material calculated in the third step. According to this model, the highest tensile stress σ_{xx} in the repair material is located at the middle bottom (in x direction) of the repair layer, and the highest interfacial tensile stress σ_{yy} and interfacial shear stress σ_{xy} are located at the two ends (in x direction). The maximum values of the stresses can be calculated using the following equations:

$$\sigma_{xx} = \frac{E_r \varepsilon_{sh}}{1 + \frac{E_r h_r}{E_s h_s}} \left(1 - \frac{2}{e^{\lambda \frac{L}{2}} + e^{-\lambda \frac{L}{2}}}\right) \tag{4.17}$$

$$\sigma_{yy} = \frac{E_r \varepsilon_{sh}}{\frac{1}{\lambda h_r} - \frac{E_r}{E_s}} \left(1 - \frac{e^{\lambda L} - 1}{e^{\lambda L} + 1} \frac{2}{\lambda L}\right) \tag{4.18}$$

$$\sigma_{xy} = \frac{E_r \varepsilon_{sh} \lambda h_r}{1 + \frac{E_r h_r}{E_s h_s}} \frac{e^{\lambda L} - 1}{e^{\lambda L} + 1} \tag{4.19}$$

where $\lambda = \sqrt{\frac{K}{E_r h_r} + \frac{K}{E_s h_s}}$ (4.20)

E_s is the elastic modulus of substrate concrete, h_s is the thickness of substrate concrete, K is the shear stiffness of interface, and L is the length of repair system.

If restrained volume change is due to combined effects of shrinkage, temperature deformation and structural loads, the ε_{sh} can be replaced by ε_{total} in this model.

For the ECC repair, the tensile stress-strain curve of ECC is assumed to be bilinear, as illustrated in Figure 4.20. When the stress is lower than the first cracking strength σ_{fc}, ECC exhibits elastic straining like concrete, as defined by E_1; When the stress is between the first cracking strength σ_{fc} and the ultimate strength σ_{cu}, ECC shows strain-hardening behavior as defined by E_2.

The calculation of stresses in the ECC repair system was divided into two stages.

In the first stage, i.e. when the tensile stress is smaller than the first cracking strength of ECC, the stresses in the ECC repair system increase as the differential volume change increases. The stresses can be calculated using Equations 4.17, 4.18, 4.19, 4.20, by replacing E_s with the elastic modulus of ECC E_1. The critical value of the differential volume change ε_{fc} corresponding to the stresses leading to first cracking of ECC can be calculated with the following equation:

$$\sigma_{xx}^{1} = \frac{E_1 \varepsilon_{fc}}{1 + \frac{E_1 h_r}{E_s h_s}} \left(1 - \frac{2}{e^{\lambda_1 \frac{L}{2}} + e^{-\lambda_1 \frac{L}{2}}}\right) = \sigma_{fc} \tag{4.21}$$

where $\lambda_1 = \sqrt{\frac{K}{E_1 h_r} + \frac{K}{E_s h_s}}$ (4.22)

With the calculated value of differential volume change ε_{fc}, the maximums of stresses at the interface can be calculated by:

$$\sigma_{yy}^{1} = \frac{E_1 \varepsilon_{fc}}{\frac{1}{\lambda_1 h_r} - \frac{E_1}{E_s}} \left(1 - \frac{e^{\lambda_1 L} - 1}{e^{\lambda_1 L} + 1} \frac{2}{\lambda_1 L}\right) \tag{4.23}$$

$$\sigma_{xy}^{1} = \frac{E_1 \varepsilon_{fc} \lambda_1 h_r}{1 + \frac{E_1 h_r}{E_s h_s}} \frac{e^{\lambda_1 L} - 1}{e^{\lambda_1 L} + 1} \tag{4.24}$$

Once the tensile stress is higher than the first cracking strength of ECC, ECC starts the multiple cracking process and enters the strain hardening stage. During this stage, the stresses induced by the increase in the differential volume change from ε_{fc} to ε_{sh} can be calculated by:

$$\sigma_{xx}^{2} = \frac{E_2 (\varepsilon_{sh} - \varepsilon_{fc})}{1 + \frac{E_2 h_r}{E_s h_s}} \left(1 - \frac{2}{e^{\lambda_2 \frac{L}{2}} + e^{-\lambda_2 \frac{L}{2}}}\right) \tag{4.25}$$

$$\sigma_{yy}^{2} = \frac{E_2 (\varepsilon_{sh} - \varepsilon_{fc})}{\frac{1}{\lambda_2 h_r} - \frac{E_2}{E_s}} \left(1 - \frac{e^{\lambda_2 L} - 1}{e^{\lambda_2 L} + 1} \frac{2}{\lambda_2 L}\right) \tag{4.26}$$

$$\sigma_{xy}^2 = \frac{E_2(\varepsilon_{sh} - \varepsilon_{fc})\lambda_2 h_r}{1 + \frac{E_2 h_r}{E_s h_s}} \frac{e^{\lambda_2 L} - 1}{e^{\lambda_2 L} + 1} \tag{4.27}$$

where $\lambda_2 = \sqrt{\frac{K}{E_2 h_r} + \frac{K}{E_s h_s}}$ (4.28)

By superimposing the stresses calculated in these two stages, the stresses in the ECC repair system induced by the differential volume change can be determined by the following equations:

$$\sigma_{xx} = \sigma_{xx}^1 + \sigma_{xx}^2 \tag{4.29}$$

$$\sigma_{yy} = \sigma_{yy}^1 + \sigma_{yy}^2 \tag{4.30}$$

$$\sigma_{xy} = \sigma_{xy}^1 + \sigma_{xy}^2 \tag{4.31}$$

The experimentally measured ECC material properties[31] were used as inputs to calculate stresses in the ECC repair system, which were experimentally and numerically investigated in previous sections, using Equations 4.29, 4.30 and 4.31. The shear stiffness of interface *K* was assumed to be 10 N/(mm^2×mm)[66]. The ECC shrinkage strain at different ages was assumed to be constant through the depth of the repair layer (independent of y). Figure 4.21 shows the calculated results. As the shrinkage of ECC increases to 392 μstrain (0.0392%), the tensile stress in ECC reaches the first cracking stress of 5.0 MPa. At this point, ECC enters the strain-hardening stage and starts inelastic straining similar to metals. As the shrinkage strain continued increasing up to 1800 μstrain (0.18%), which corresponds to the measured free shrinkage of ECC M45 (28-day, 45 ± 5% RH, 20±1 °C (66-70 °F)), the stresses in the ECC repair only increases a small amount. This is because of the low stress-strain gradient E_2 in the strain-hardening

stage. As the maximum imposed shrinkage strain 0.18% is greatly lower than ECC tensile strain capacity 3-6%, the material is still experiencing the early part of its strain-hardening stage through multiple microcracking, and there is no danger of tensile failure. Additionally, Figure 4.21 shows the interfacial stresses increase as shrinkage increases to 392 μstrain (0.0392%). Beyond this strain level, the increase rates interfacial stresses become extremely slow. This shows that the inelastic straining of ECC material effectively reduces the stresses built up at the repair/old interface, therefore suppressing interfacial delamination.

The modeling results correspond well with the experimental findings and FEM results described in previous sections, in term of the stress development in the ECC repair layer and at the interface as well as their effects on repair cracking and interfacial delamination. Although some assumptions (e.g. interfacial shear stiffness as 10 $N/(mm^2 \times mm)$) need to be further validated, this analytical model provides a useful tool to study the influence of various parameters (e.g. interfacial shear stiffness, repair length and thickness, repair material tensile strain capacity, tensile strength and elastic modulus) on the stresses and strains in the repair and at the repair/old interface, and to predict the performance of different repair systems. The details will be included in future publications.

4.9 Conclusions

Simultaneously suppressing repair cracking and interfacial delamination, which are induced by restrained volume change, can be achieved using ductile ECC repair materials as proposed in this study. The free drying shrinkage properties of HES-ECC

were characterized at different RHs. Results showed that the shrinkage strain of HES-ECC was below 0.3%, which was one order of magnitude lower than its tensile strain capacity of 3-6%, therefore leading to a highly negative cracking potential value. This implied that when the drying shrinkage of HES-ECC was restrained, the material's ductility can accommodate shrinkage deformation by forming multiple microcracks during its strain hardening stage without localized cracking failure. This contention was proven later by the results of the restrained shrinkage ring test and the restrained shrinkage test on a simulated repair system.

An experimental study was conducted on a simulated repair system subject to drying shrinkage, in order to investigate the effects of repair material ductility and surface preparation on the repair's performance. When an adequate bond was present, 3 ~ 4 large surface cracks with width up to 520 μm formed in the HES-Concrete repair layer, accompanied by a small amount of interfacial delamination up to 90 μm. For the HES-SFRC repair system, 1 ~ 4 large surface cracks formed, and the presence of steel fibers reduced the maximum crack width to 280 μm. However, the interfacial delamination of HES-SFRC repair was the largest among the three repair materials. This was explained by the significant amount of restrained shrinkage induced tensile and shear stresses at the interface, which had no avenue of release through material inelastic straining as does HES-ECC, or crack free-opening as does HES-Concrete. For the HES-ECC repair, more than 100 fine microcracks with width less than 50 μm formed in the repair layer, accompanied by interface delamination less than 80 μm at the ends. Similar constrasts in behavior were also found in concrete, SFRC, and ECC repair systems, suggesting that the

ductility of a repair material is the most critical factor contributing to the resistance to repair cracking and delamination.

Experimental results also showed that sufficient bonding strength was necessary for ECC repair materials to fully utilize their tensile ductility to achieve desired performance. However, for brittle or quasi-brittle repair materials with large cracking potential values, increasing bonding strength will provide only limited aid in improving the durability of the repaired system. This is due to the interaction between the repair and concrete substrate, and the time-dependent competition between surface cracking and interfacial delamination. Therefore, simply seeking a strong bond while ignoring the critical influence of the repair material's tensile ductility on reducing cracking potential cannot fundamentally improve repair durability.

The results from an FEM study further confirmed the influence of repair material ductility on the repair system's resistance to cracking and interfacial delamination. The analysis provided additional insights on the stress distribution in the repair systems using brittle, quasi-brittle, and ductile repair materials, respectively. It revealed that the shrinkage deformation of ECC was accommodated by the "plastic" strain of the ECC repair layer by forming saturated microcracks, which still carried significant amounts of stress after formation. The uniform deformation of the ECC repair in a ductile manner relieved the stresses everywhere along the interface, so that a small amount of interface delamination existed only at the repair ends. In the concrete repair, cracking happened when the restrained shrinkage caused the tensile stress in the repair layer to reach the material tensile strength. Opening these tract-free cracks relieves part of the interface normal and shear stresses, and reduces interface delamination at the ends of repair.

However, the model showed that σ_{xy} and σ_{yy} remained at a significant level. In the SFRC repair, σ_{xx} is non-zero at the cracking locations due to its tension-softening behavior associated with steel fiber bridging. This resulted in high interfacial stresses between the SFRC repair and old concrete. The FEM study provided understanding on the mechanical mechanism behind the repair/substrate composite performance that was observed in the experimental study.

Additionally, a simplified analytical model was derived to calculate the tensile stress in the repair layer, and the tensile and shear stresses at the interface. The model-predicted results corresponded well with the experimental findings and the FEM results. More importantly, this analytical model can be used to study the influence of different parameters (e.g. interfacial shear stiffness, repair length and thickness, repair material tensile strain capacity, tensile strength and elastic modulus) on the stresses and strains in the repair and at the repair/old interface.

This research departs from the traditional emphasis on isolated material properties such as high compressive strength and low shrinkage, and intends to shift the repair industry's attention toward the age-dependent interaction between the new repair and old concrete. To ensure dimensional compatibility between the repair and existing concrete, a repair material with large inelastic tensile strain capacity (ductility) is necessary. When the material ductility requirement is satisfied, cracking control reinforcements and repair material free drying shrinkage limits will become less important, and surface preparation methods to enhance the interface bond will be more meaningful toward achieving durability of repaired concrete structures.

Table 4.1 – General requirements of patch repair materials for structural compatibility.

Property	Relationship of repair mortar (R) to concrete substrate (C)
Strength in compression, tension, and flexure	$R \geq C$
Modulus in compression, tension, and flexure	$R \approx C$
Poisson's ratio	Dependent on modulus and type of repair
Coefficient of thermal expansion	$R \approx C$
Adhesion in tension and shear	$R \geq C$
Curing and long-term shrinkage	$R \leq C$
Strain Capacity	$R \geq C$
Creep	Dependent on whether creep causes desirable or undesirable effects
Fatigue performance	$R \geq C$
Chemical reactivity	Should not promote alkali-aggregate reaction, sulfate attack, or corrosion of reinforcement in the substrate
Electrochemical stability	Dependent on permeability of patch material and chloride ion content of substrate

Table 4.2 – Mix proportion of the investigated materials.

Material	C [(a)]	W	S	CA	SP	AC	V_f [(c)]
HES-Concrete	1.0	0.4	1.3	1.3	0.005	0.04	--
HES-SFRC	1.0	0.4	1.3	1.3	0.005	0.04	0.01 [(d)]
HES-ECC	1.0	0.33	1.0	0.064 [(b)]	0.0075	0.04	0.02 [(e)]

[(a)] Portland type III cement
[(b)] Polystyrene beads as "coarse aggregates" for HES-ECC
[(c)] Fiber volume content
[(d)] Steel hooked fibers used for HES-SFRC
[(e)] PVA fiber used for HES-ECC

Table 4.3 – Mechanical properties of the investigated materials.

Material	Age	$f_c'^{(a)}$, MPa(psi)	E [(a)], GPa(ksi)	ε_u %	Tensile Behavior
HES-Concrete	7 d	49.9 ± 1.6 (7234 ± 228)	26.2±1.4 (27.8± 196)	0.01	brittle
	28 d	54.2 ± 2.4 (7860± 345)	27.8±1.5 (4025 ± 221)		
HES-SFRC	7 d	51.5 ± 2.4 (7462 ± 348)	25.7±2.0 (3725 ± 287)	0.01	quasi-brittle
	28d	57.0 ± 2.0 (8254 ±290)	29.2±1.3 (4231 ± 189)		
HES-ECC	7 d	47.5 ± 1.9 (6885 ± 275)	20.6±0.7 (2986 ± 101)	3~6	ductile
	28 d	55.6 ± 2.2 (8063±315)	23.2±1.0 (3365 ± 140)		

Table 4.4 – HES-ECC tensile properties at different ages.

Age	E[(a)], GPa(ksi)	Tensile Strength[(a)]MPa(psi)	Strain Capacity (%)
4 h	13.10 ± 0.77 (1900 ± 111)	3.46 ± 0.08 (501 ± 12)	5.97± 0.22
6 h	14.98 ± 0.79 (2173 ± 114)	4.21 ± 0.13 (610 ± 19)	4.97± 0.38
12 h	16.05 ± 1.02 (2328 ± 147)	4.57 ± 0.17 (662 ± 25)	4.41± 0.33
24 h	18.30 ± 0.59 (2654 ± 85)	4.69 ± 0.08 (680 ± 12)	3.99± 0.27
7 d	20.59 ± 0.70 (2986 ± 101)	5.56 ± 0.11 (807 ± 16)	3.52± 0.29
28 d	23.20 ± 0.96 (3365 ± 140)	5.68 ± 0.14 (823 ± 20)	3.47± 0.62

[(a)] Mean ± standard deviation (measured from 9 specimens for each of the properties)

Table 4.5 – Theoretical parametric values of the investigated materials.

	A [J/g]	B [J/g]	λ [g/J] x10^{-3}	c [g/J] x10^{-5}	d [g/J] x10^{-4}
HES-ECC	8.4	13.1	3.1	4.3	-1.0
HES-Concrete	2.9	8.5	3.8	1.6	1.2
ECC (M45)*	8.2	17.9	2.3	2.0	+7.1
Concrete*	2.3	5.1	4.0	1.9	-3.0

* Values adopted from Weimann and Li, 2003[48]

Table 4.6 – Restrained drying shrinkage crack width development with age.

Age (day)	Average cracking width, μm (in)	
	HES-ECC	HES-Concrete
0	0 (0)	0 (0)
1	30 (0.001182)	0 (0)
2	40 (0.001576)	310 (0.012214)
3	50 (0.00197)	590 (0.023246)
4	50 (0.00197)	610 (0.024034)
14	50 (0.00197)	1070 (0.042158)
28	50 (0.00197)	1210 (0.047674)
40	50 (0.00197)	1250 (0.049250)
60	50 (0.00197)	1250 (0.049250)

Table 4.7 – Estimated material cracking potentials, RH=45%.

Properties	ε_{sh}(%)	ε_e(%)	ε_i (%)	ε_{cp} (%)	$p = \varepsilon_{sh} - (\varepsilon_e + \varepsilon_i + \varepsilon_{cp})$ (%)
HES-Concrete	0.105	0.01	0	0.02 - 0.06	0.035 to 0.075
HES-SFRC	0.077	0.01	0	0.02 - 0.06	0.007 to 0.047
HES-ECC	0.242	0.015	3 - 6	0.07	(-5.343) to (-2.843)

*****Properties were measured at specimen's age of 28 days.

Table 4.8 – Interface delamination and surface cracking of HES-Concrete, HES-SFRC, and HES-ECC layered repair systems at the age of 60 days.

Repair Material	Specimen Number	Delamination		Surface Cracking	
		Height, μm (in $\times 10^{-3}$)	Length, mm (in)	Number	Width, μm (in $\times 10^{-3}$)
HES-Concrete	(1)	90 (3.54)	170 (6.69)	3	160 (6.30), 520 (20.5), 370 (14.6)
	(2)	30 (1.18)	27 (1.06)	4	190 (7.48), 340 (13.4), 360 (14.2), 490 (19.3)
	(3)	65 (2.56)	73 (2.87)	4	700 (2.76), 380 (15.0), 420 (16.5), 450 (17.7)
HES-SFRC	(1)	310 (12.2)	323 (12.72)	2	110 (4.33), 120 (4.72)
	(2)	260 (10.2)	301 (11.85)	4	50 (1.97), 90 (3.54), 120 (4.72), 130 (5.12)
	(3)	300 (11.8)	342 (13.46)	1	280 (11.0)
HES-ECC	(1)	80 (3.15)	82 (3.23)	83	10 – 50 (0.39 - 1.97)
	(2)	50 (1.97)	47 (1.85)	109	10 - 60 (0.39 - 2.36)
	(3)	75 (2.95)	79 (3.11)	113	10 - 50 (0.39 - 1.97)

Table 4.9: Material composition, 28-day mechanical properties and cracking potential.

Material	C[(a)]	W	S	FA	CA	SP	V_f[(b)]	V_f	ε_u %	f_c' (MPa)	E (GPa)	*p*
Concrete	1.0	0.4	1.3	--	1.3	0.01	--	--	0.01	60±1	26±1	0 to 0.04
SFRC	1.0	0.4	1.3	--	1.3	0.01	0.01 [(c)]	0.01	0.01	63±2	26±1	(-0.017) to 0.023
ECC	1.0	0.53	0.8	1.2	--	0.03	0.02 [(d)]	0.02	3~5	62±2	20±1	(-4.908) to (-2.408)

[(a)] Portland type I cement
[(b)] Fiber volume content
[(c)] Steel hooked fibers used for SFRC
[(d)] PVA fiber used for ECC

Table 4.10 – Interface delamination and surface cracking of concrete, SFRC and ECC layered repair systems.

Repair Material	Surface Preparation	Delamination		Cracking	
		Height (μm)	Length (mm)	Number	Width (μm)
Concrete	Smooth	410	320	2	120-130
	4-5mm roughened	190	172	3	130-190
	7-8mm roughened	65	50	4	220-270
	7-8 mm roughened + bonding slurry	32	23	4	210-360
SFRC	Smooth	550	397	2	90-120
	4-5mm roughened	370	375	5	70-110
	7-8mm roughened	275	350	3	120-140
	7-8 mm roughened + bonding slurry	310	354	4	90-150
ECC	Smooth	1225	722	0	--
	4-5mm roughened	425	402	21	10-60
	7-8mm roughened	53	50	76	10-60
	7-8mm roughened + bonding slurry	40	31	103	10-60

Table 4.11 – Interface property values in FEM model.

f_t (MPa)	4.0
Factor for S1	0.25
w1 (mm)	0.05
w2 (mm)	0.2
Friction angle (Degr.)	35.0
Maximum slip (mm)	3.0
Normal stiffness (N/mm^3)	100
Shear stiffness (N/mm^3)	10

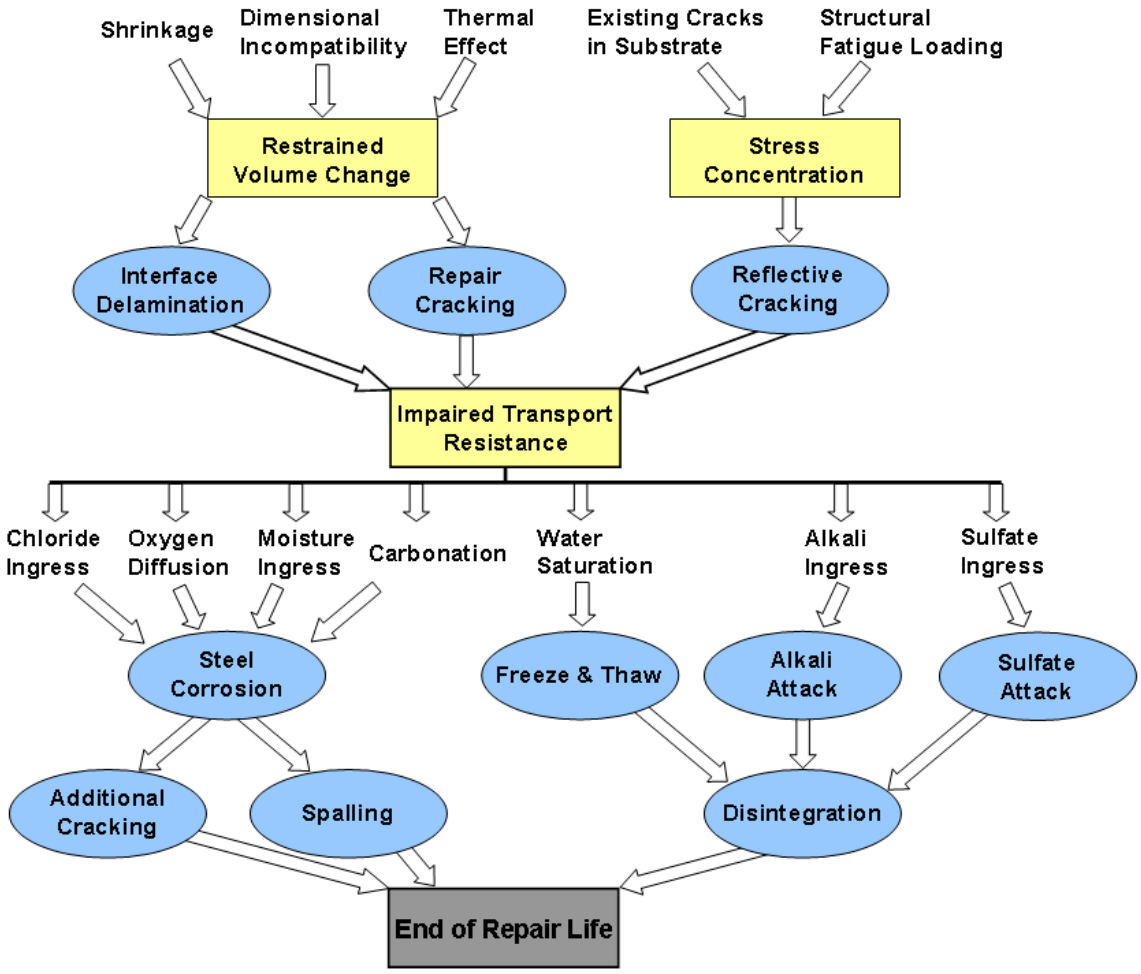

Figure 4.1 – Typical deterioration process of concrete repair.

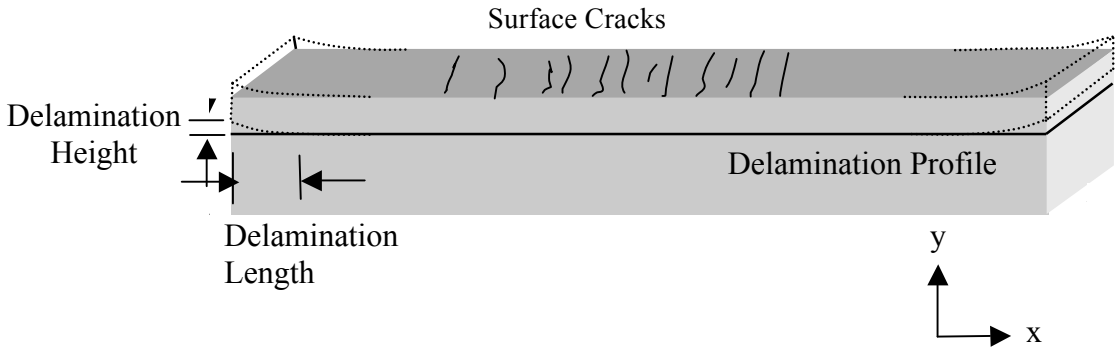

Figure 4.2 – Schematics of typical failure modes in layered repair system.

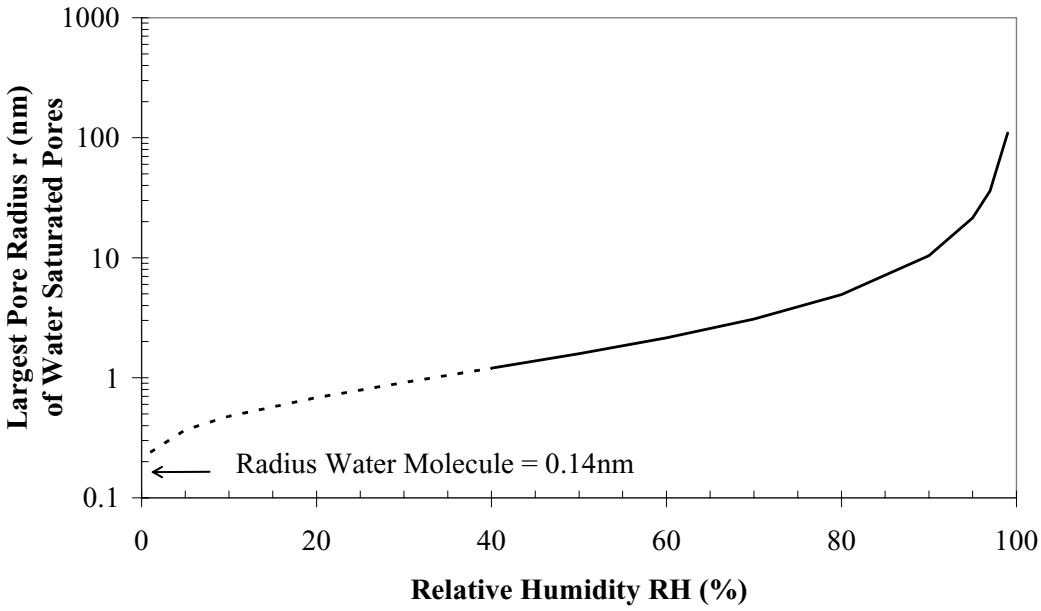

Figure 4.3 – Illustration of the Kelvin Equation.

Figure 4.4 – Free drying shrinkage test.

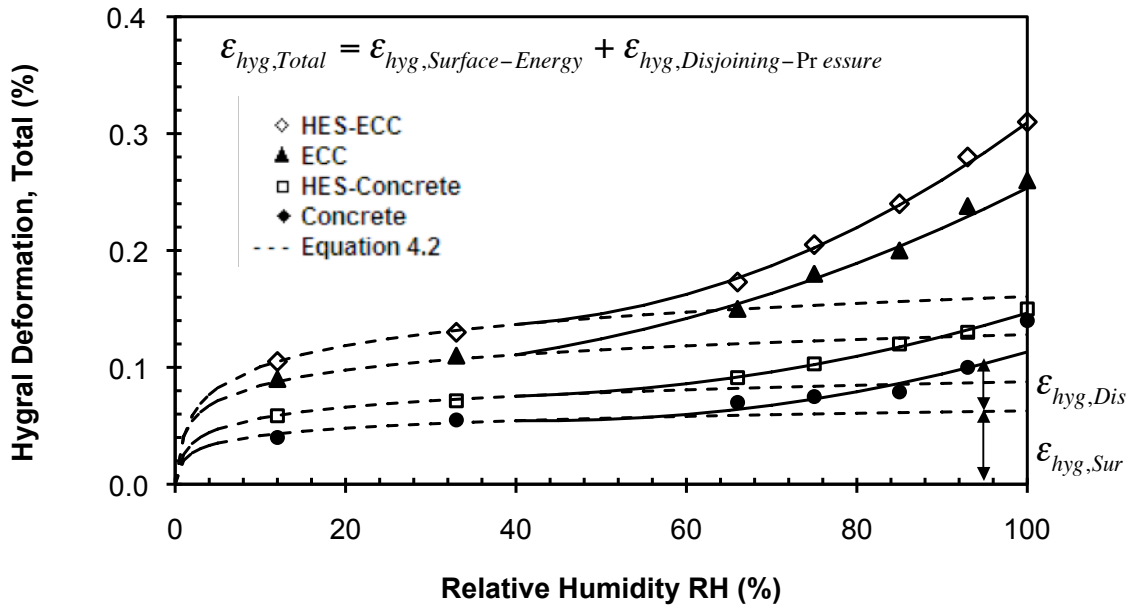

Figure 4.5 – Experimental data and theoretical curves of hygral deformation vs. relative humidity for the investigated materials (data of HES-ECC and HES-Concrete are measured in this study; data of ECC and Concrete are adopted from Weimann and Li, 2003).

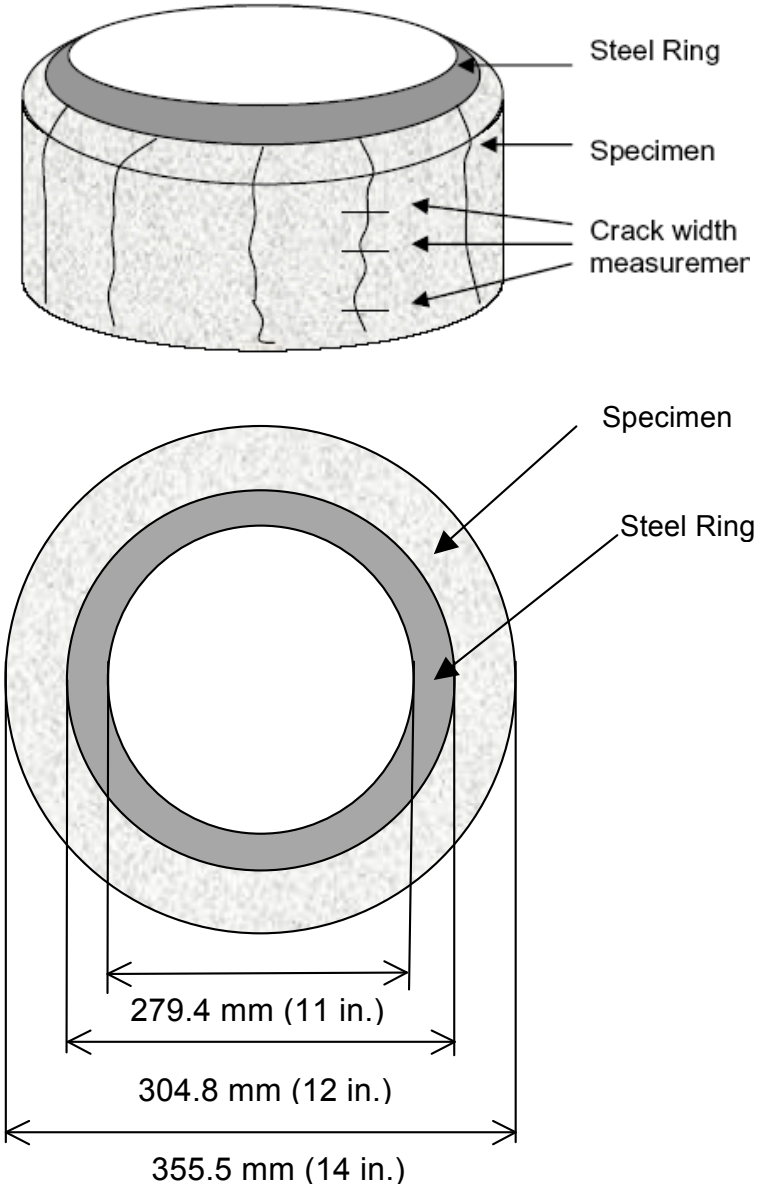

Figure 4.6 – Restrained shrinkage steel ring test.

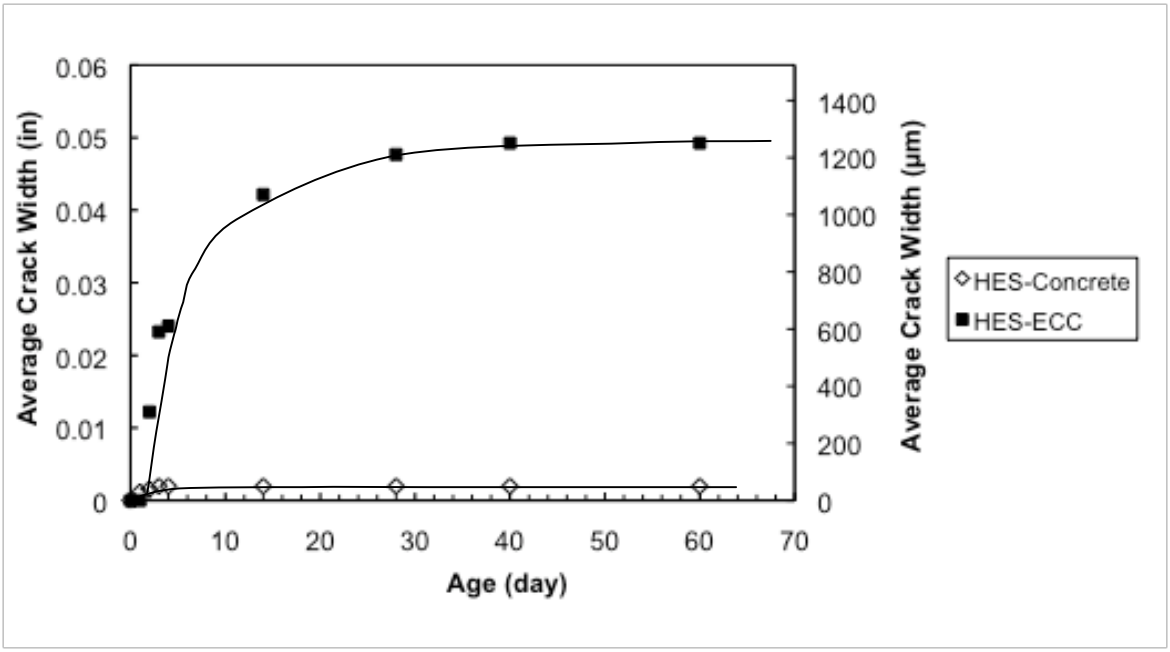

Figure 4.7 – Restrained shrinkage crack width development as a function of drying time (at RH = 45 ± 5%).

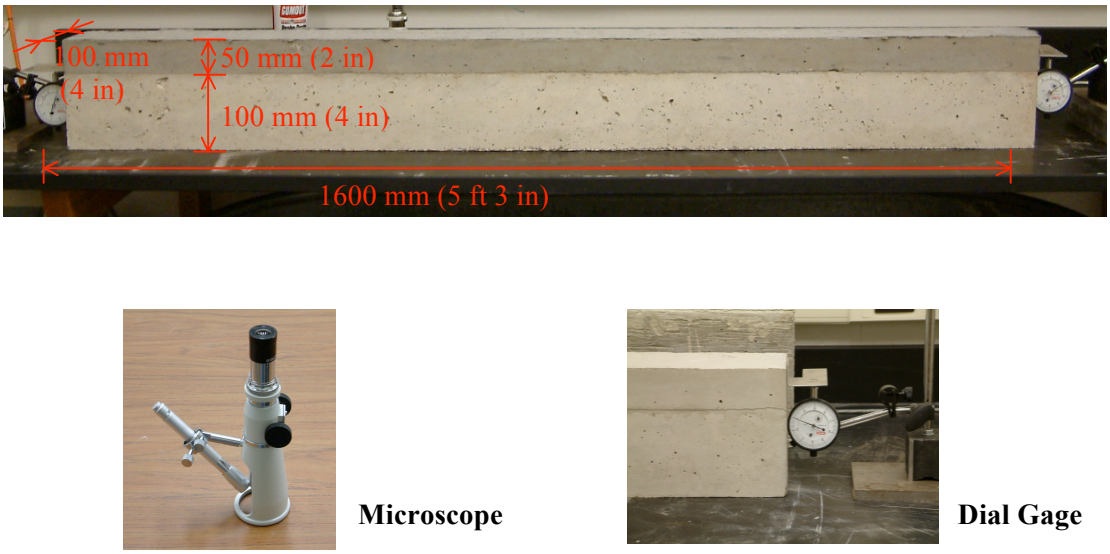

Figure 4.8 – Layered repair system test set-up under restrained shrinkage.

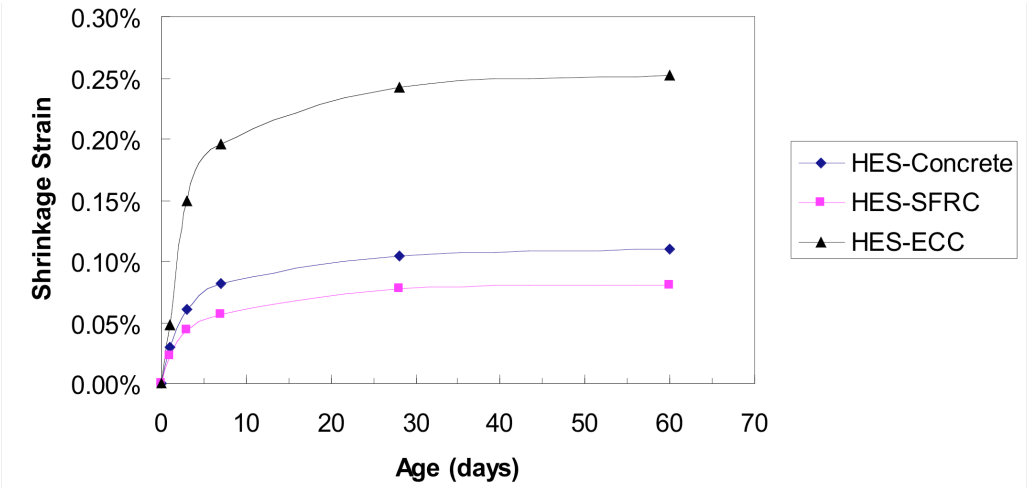

Figure 4.9– Free shrinkage strain of repair materials at different ages.

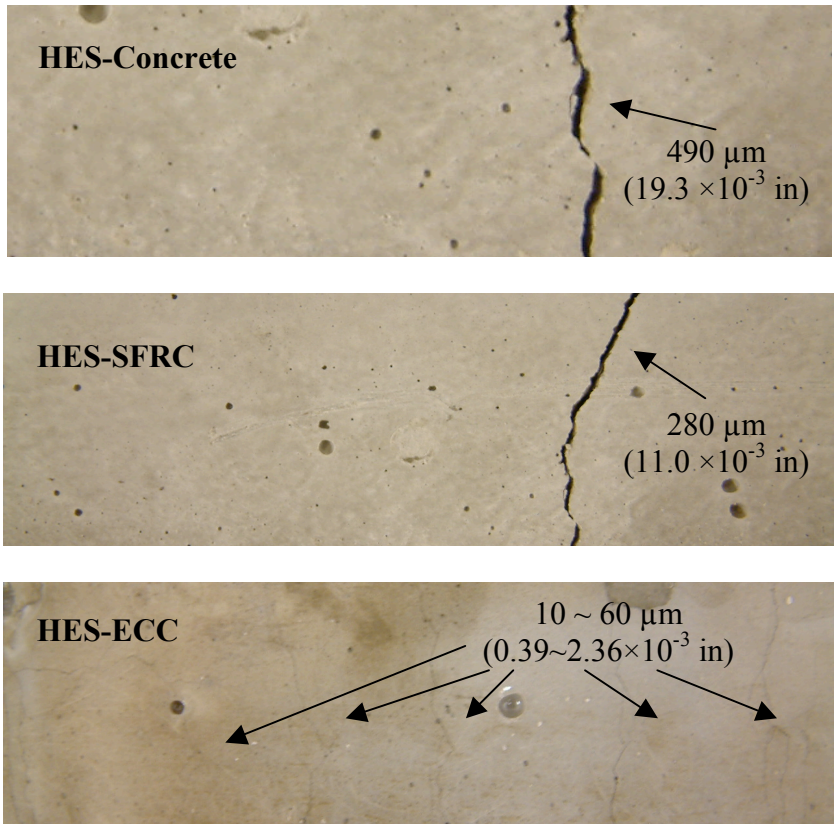

Figure 4.10 – Repair surface cracking at the age of 60 days.

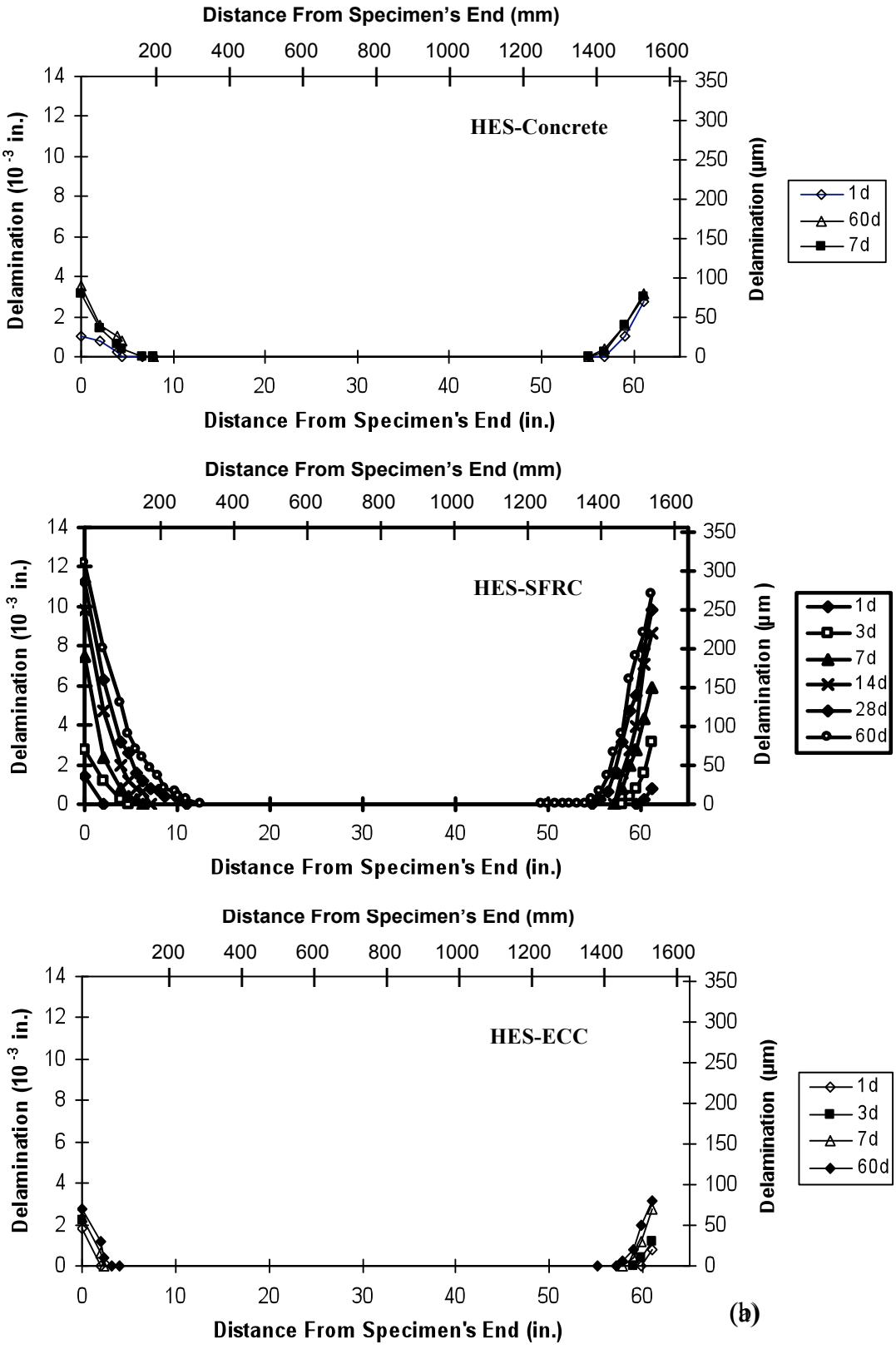

Figure 4.11 – Interface delamination profiles of repaired systems.

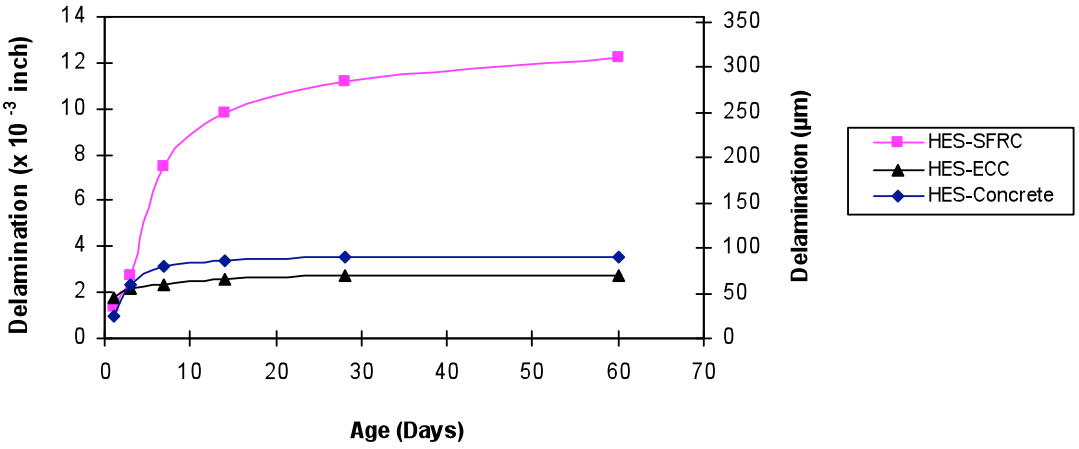

Figure 4.12 – Specimen end delamination height at different ages.

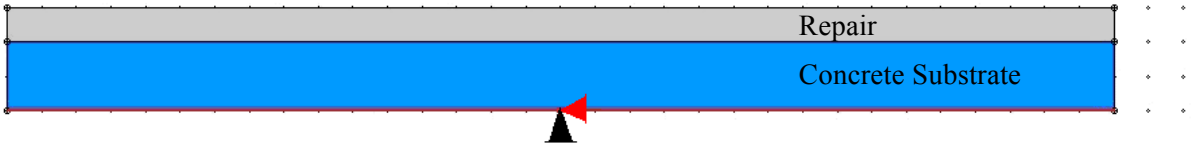

Figure 4.13 – FEM model of layered repair system.

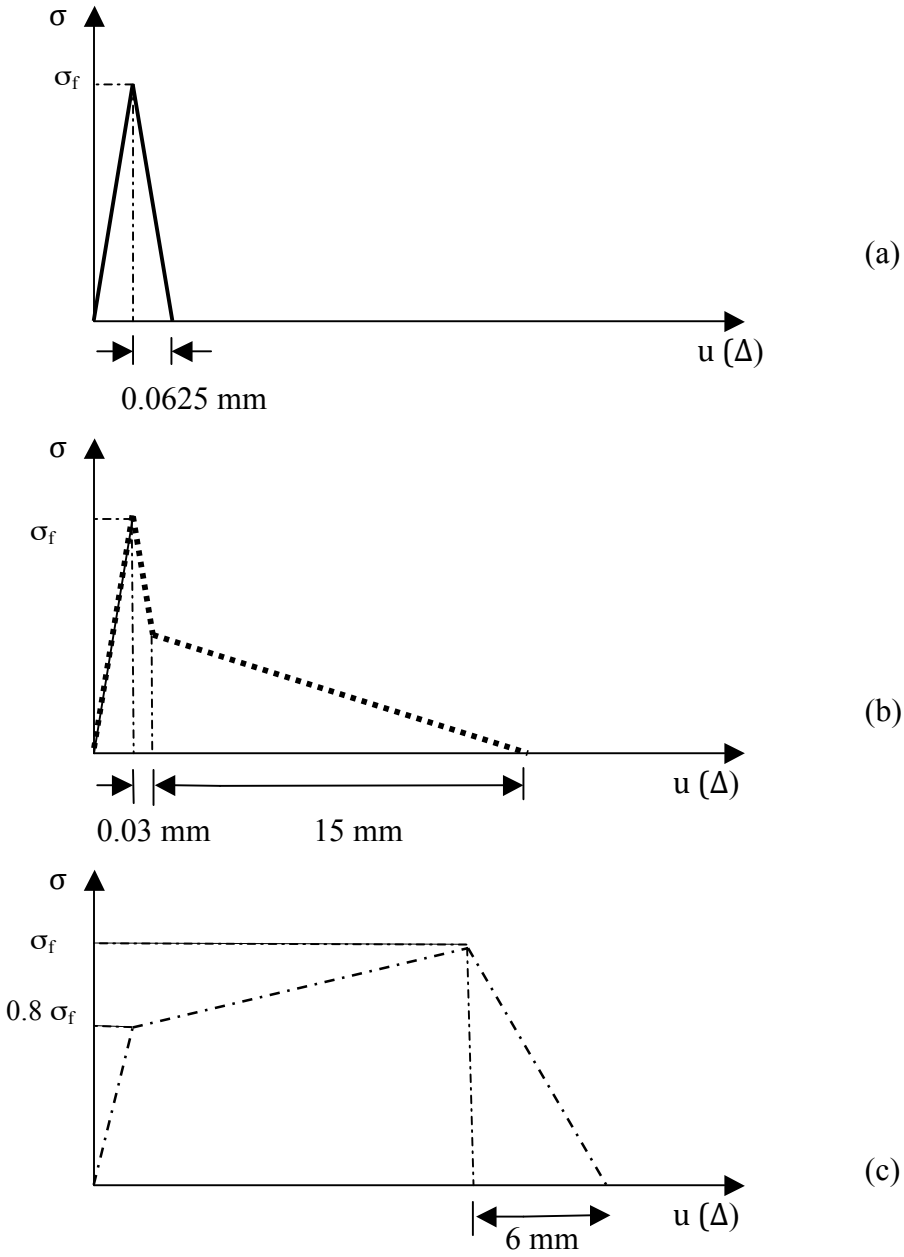

Figure 4.14 – Assumed tensile behavior of (a) HES-Concrete, (b) HES-SFRC, (c) HES-ECC materials, and (d) combined for all three materials.

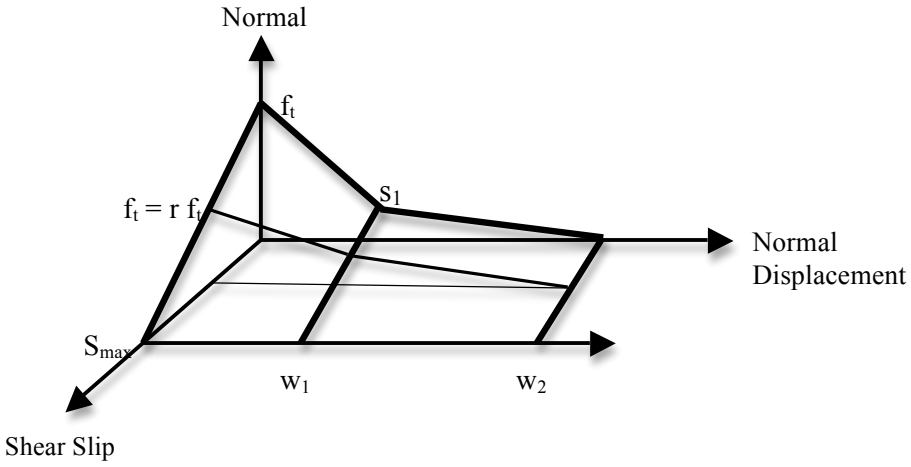

Figure 4.15 – Interface model: combined uniaxial stress-strain relation in the normal direction with influence of shear slip.

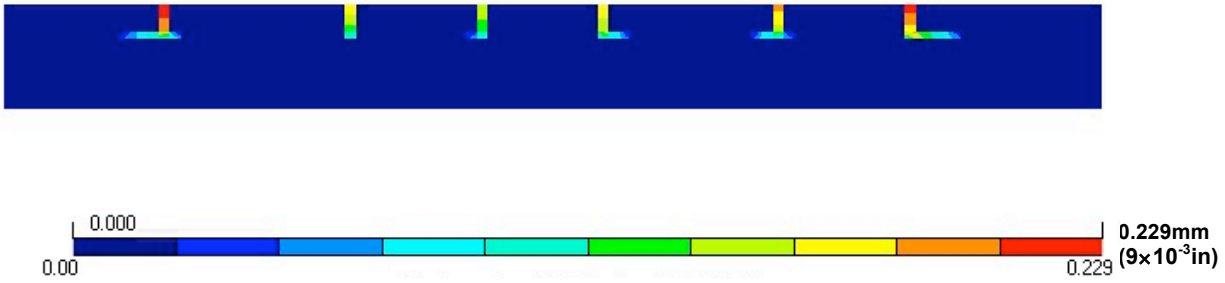

(a) HES-Concrete

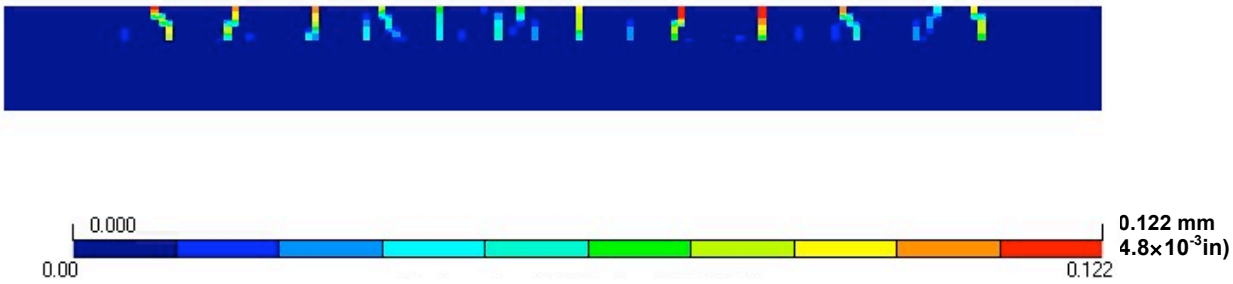

(b) HES-SFRC

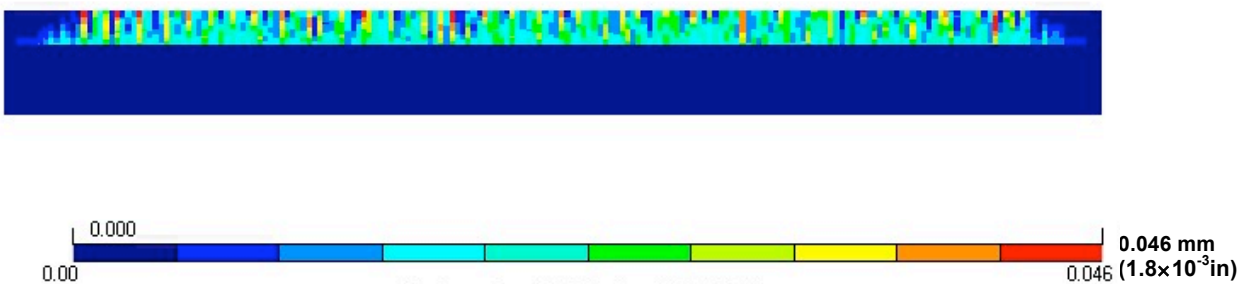

(c) HES-ECC

Figure 4.16 – Predicted crack width of (a) HES-Concrete, (b) HES-SFRC and (c) HES-ECC repair layer at the age of 60 days.

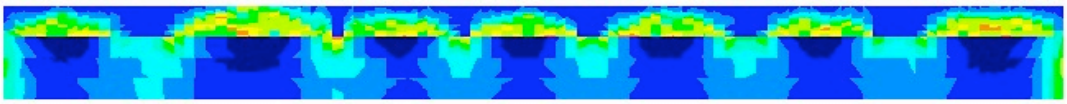

(a) HES-Concrete

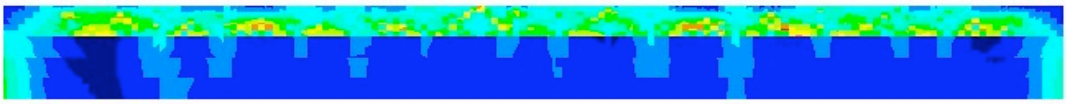

(a) HES-SFRC

(b) HES-ECC

Figure 4.17 – Predicted stress distribution (σ_{xx}) in the (a) HES-Concrete, (b) HES-SFRC and (c) HES-ECC repaired system at the age of 60 days

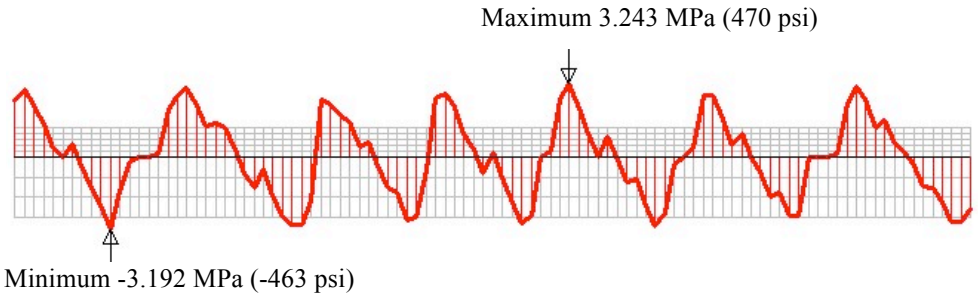

(c) HES-Concrete

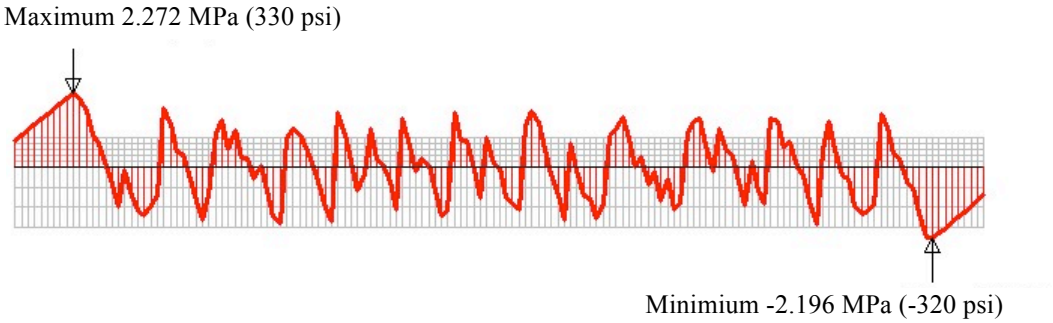

(b) HES-SFRC

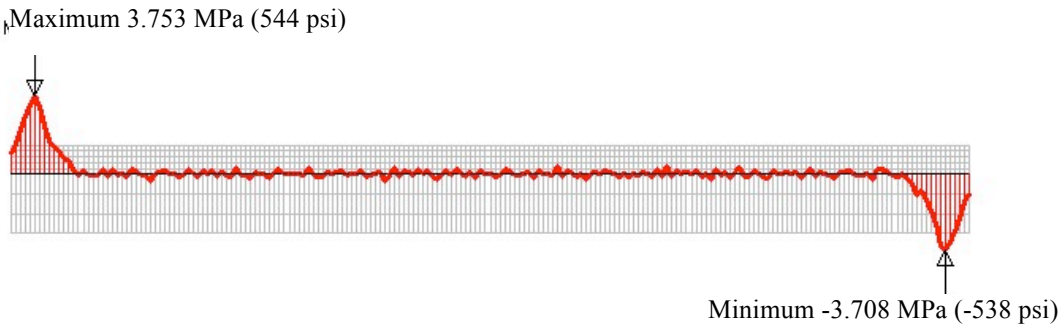

(c) HES-ECC

Figure 4.18 – Predicted interface shear stress (σ_{xy}) of (a) HES-Concrete, (b) HES-SFRC and (c) HES-ECC repaired system.

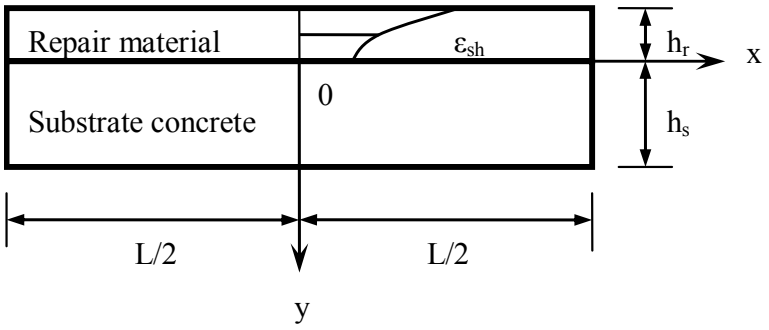

Figure 4.19 – Concrete repair subjected differential shrinkage.

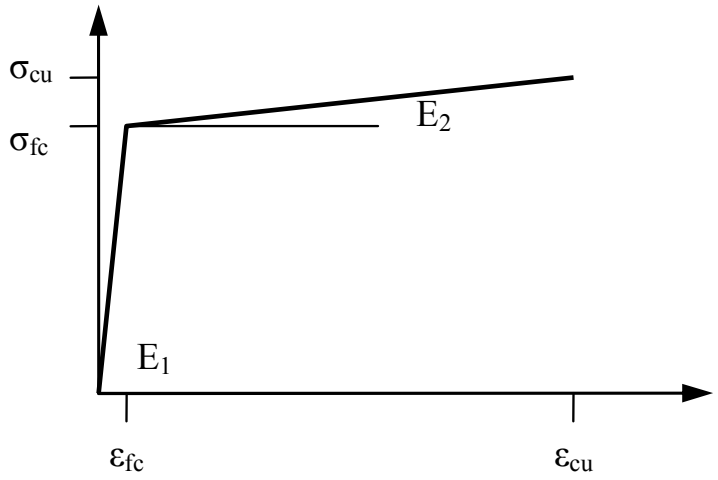

Figure 4.20 – Simplified tensile stress-strain curve of ECC.

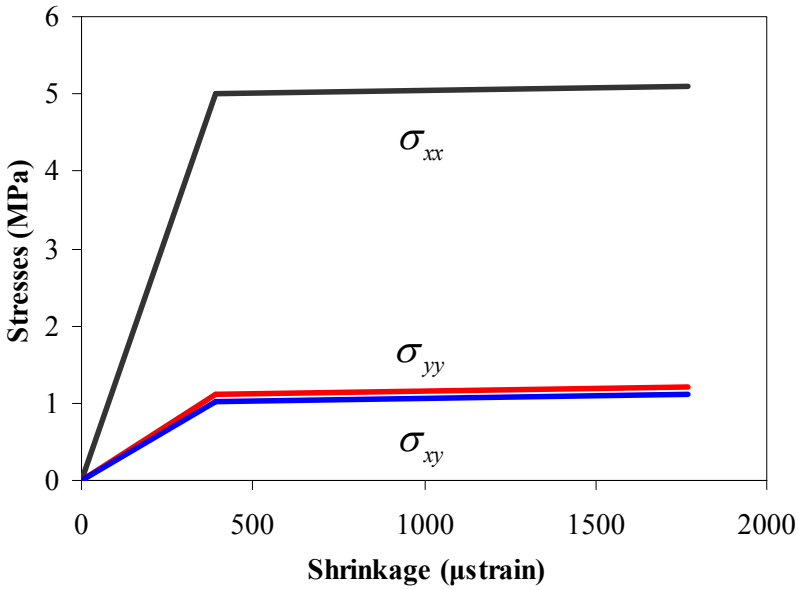

Figure 4.21 – Analytical model predicted tensile stress in ECC repair σ_{xx}, repair/old interfacial tensile stress σ_{yy} and shear stress σ_{xy}.

References:

[1] Vaysburd, A. M., Emmons, P. H., McDonald, J. E., Poston, R. W., and Kesner, K. E., "Selecting Durable Repair Materials: Performance Criteria – Field Studies," *Concrete International*, Vol. 22, No. 12, December 2000, pp. 39-45.

[2] Vaysburd, A. M., Emmons, P. H., Mailvaganam, N. P., Mcdonald, J. E., and Bissonnette, B., "Concrete Repair Technology – A Revised Approach is Needed," *Concrete International*, Vol. 26, No. 1, January 2004, pp. 59-65.

[3] Banthia, N. and Gupta, R., "Repairing with Fiber-Reinforced Concrete – Cellulose Fiber Enhance Overlay Performance," *Concrete International*, Vol. 28, No. 11, November 2006, pp. 36-39.

[4] Cusson, D., Qian, S., and Hoogeveen, T., " Field Performance of Concrete Repair Systems on Highway Bridges," *ACI Materials Journal*, Vol. 103, No. 5, 2006, pp. 366-373.

[5] Vaysburd, A. M., Brown, C. D., Bissonnette, B., and Emmons, P. H., " "Realcrete" versus "Labcrete" – Searching for Tests that Give Reliable Results," *Concrete International*, Vol. 26, No. 2, February 2004, pp. 90-94.

[6] Lawler, J.S., Zampini,D., and Shah, S. P., "Permeability of Cracked Hybrid Fiber-Reinforced Mortar under Load," *ACI Materials Journal,* Vol. 99, No. 4, pp. 379-385.

[7] Hearn, N. "Effect of Shrinkage and Load-Induced Cracking on Water Permeability of Concrete," *ACI Materials Journal,* Vol. 96, No. 2, pp. 234-241.

[8] Gerard, B., Reinhardt, H. W., and Breysse, D., "Measured transport in cracked concrete" *Penetration and Permeability of Concrete: RILEM Report 16.* Ed. H.W. Reinhardt. 1997, pp. 265-331.

[9] Gerard, B., Jacobsen, S., and Marchand, J., "Concrete Cracks II: Observation and Permeability – A Review," *Concrete Under Severe Conditions 2, Environment and Loading, Vol. 1*, Gjorv, E & FN Spon, eds. Sakai, K and Banthia, N., 1998, pp. 183-197.

[10] Lepech, M., and Li, V. C., "Water Permeability of Cracked Cementitious Composites," Paper 4539 of Compendium of Papers CD ROM, ICF 11, Turin, Italy, March 2005.

[11] Sahmaran, M., Li, M., and Li, V. C., "Transport Properties of Engineered Cementitious Composites Under Chloride Exposure," *ACI Materials Journal*, Vol.104, No. 6, 2007, pp. 604-611.

[12] Iowa Department of Transportation (Iowa DOT), "A Study of Transverse Cracks in the Keokuk Bridge Deck," *Final Rep.*, Ames, Iowa, 1986.

[13] Perfetti, G. R., Johnson, D. W., and Bingham, W. L., "Incidence Assessment of Transverse Cracking in Concrete Bridge Decks: Structural Considerations," *Rep. No. FHWA/NC/85-002*, Vol. 2, Federal Highway Administration, Washington, D. C., 1985.

[14] Cheng, T. T., and Johnson, D. W., "Incidence Assessment of Transverse Cracking in Bridge Decks: Construction and Material Consideration," *Rep. No. FHWA/NC/85-002*, Federal Highway Administration, Washington, D. C., Vol. 1, 1985.

[15] Perragaux, G. R., and Brewester, D. R., "In-Service Performance of Epoxy Coated Steel Reinforcement in Bridge Decks," *Final Technical Rep*. No. 92-3, New York State Department of Transportation, Albany, N. Y., 1992.

[16] Kriviak, G. W., Skeet, J. A., and Carter, P. D., "Service Life Prediction of Protective Systems for Concrete Bridge Decks in Alberta," *International Association of Bridges and Structural Engineers Symposium*, San Francisco, Calif.,1995, pp. 469-474,.

[17] Czarnecki, L., Garbacz, A., Lukowski, P., and Clifton, J. R., "Polymer Composites for Repairing Portland Cement Concrete: Compatibility Project," *Technical Report NISTIR 6394*, National Institute of Standards and Technology, 1999.

[18]Emmons, P. H., Vaysburd, A. M., Poston, R. W., and McDonald, J. E., "Performance Criteria for Concrete Repair Materials, Phase II, Field Studies," *Technical Report REMR-CS-60*, U. S. Army Waterways Experiment Station, Vicksburg, MS, September 1998.

[19] Pigeon, M. and Bissonnette, B., "Bonded Concrete Repairs: Tensile Creep and Cracking Potential," *Concrete International*, Vol. 21, No. 11, November 1999, pp. 31-35.

[20] Vayburd, A. M., "Research Needs for Establishing Material Properties to Minimize Cracking in Concrete Repairs, Summary of a Workshop," *ICRI Publication No. Y320001*, 1996.

[21] Vaysburd, A. M., Emmons, P. H., McDonald, J. E., Poston, R. W., and Kesner, K. E., "Performance Criteria for Concrete Repair Materials, Phase II Summary Report," *Technical Report REMR-CS-62*, U. S. Army Engineers Waterways Experiment Station, Vicksburg, MS, March 1999.

[22] Emberson, N. K., and Mays, G. C., "Significance of Property Mismatch in the Patch Repair of Structural Concete. Part I: Properties of Repair Systems," *Magazine of Concrete Research*, No. 152, September 1990, pp. 147-160.

[23] Babaei, K., and Hawkins, N. M.,"Evaluation of Bridge Deck Protective Strategies," *NCHRP Rep. No. 297*, Transportation Research Board, National Research Council, Washington, D. C., 1987.

[24] La Fraugh, R. W., and Perenchio, W. F., "Phase I Report of Bridge Deck Cracking Study West Seattle Bridge," *Rep. No. 890716*, Wiss, Janney, Elstner Associates, Northbrook, Ill, 1989.

[25] Babaei, K. and Purvis, R., "Prevention of Cracks in Concrete Bridge Decks: Report on Laboratory Investigation of Concrete Shrinkage," *Research Project No. 89-01*, Pennsylvania Department of Transportation, Harrisburg, PA, 1994.

[26] Ducrete, J., Lebet, J. , and Monney, C., "Hydration Effect and Deck Cracking During the Construction of Steel Concrete Composite Bridges," *Proc. ICOM-Construction Mettalique*, Article 359, 1997.

[27] French, C., Eppers, L., Le, Q., and Hajjar, J. F., "Transverse Cracking in Concrete Bridge Decks," *Transportation Research Record 1688*, Transportation Research Board, Washington, D. C., 1999, pp. 21-29.

[28] Frosch, R. J., Radabaugh, R. D., and Blackman, D. T., "Investigation of Transverse Deck Cracking," *Proc. Structures Congress*, ASCE, Reston, VA, 2002.

[29] Wittmann, F. H., and Martinola, G., "Decisive Properties of Durable Cement-Based Coatings for Reinforced Concrete Structures," *International Journal for Restoration of Buildings and Monuments*, Vol. 9, No 3, pp 235-264, 2003.

[30] Li, M., and Li, V. C., "Durability of HES-ECC Repair Under Mechanical and Environmental Loading Conditions," *Proc., High Performance Fiber Reinforced Cement Composites (HPFRCC5)*, Eds. H.W. Reinhardt and A.E. Naaman, Mainz, Germany, 2007, pp. 399-408.

[31] Li, M., and Li, V. C., "Behavior of ECC/Concrete Layered Repair System under Drying Shrinkage Conditions", *International Journal of Restoration of Buildings and Monuments*, Vol. 12, No. 2, 2006, pp. 143-160.

[32] Mehta, P. K., *Concrete: Structure, Properties, and Materials*, Prentice-Hall, Englewood Cliffs, New Jersey, 1986, pp. 353-367.

[33] Chang, P. K., Peng, Y. N., and Hwang, C. L., "A Design Consideration for Durability of High-Performance Concrete," *Cement & Concrete Composites*, Vol. 23, No. 4-5, Aug. – Oct. 2001, pp. 375-380.

[34] Hwang, C. L., Liu, J. J., Lee, L. S., and Lin, F. Y., "Densified Mixture Design Algorithm and Early Properties of High Performance Concrete, " *Journal of the Chinese Institute of Civil and Hydraulic Engineering*, Vol. 8, No. 2, 1996, pp. 217-229.

[35] Shah, S. P., Wang, K., and Weiss, W. J., "Is High Strength Concrete Durable?" *Concrete Technology for a Sustainable Development in the 21st Century* Eds. O. E. Gjorv and K. Sakai, 2000, pp. 102-114.

[36] Li, M., and Li, V. C., "Behavior of ECC/Concrete Layered Repair System under Drying Shrinkage Conditions", *Journal of Restoration of Buildings and Monuments*, Vol. 12, No. 2, 2006, pp143-160.

[37] Li, V.C., "High Performance Fiber Reinforced Cementitious Composites as Durable Material for Concrete Structure Repair," *Proc. of ICFRC Int'l Conference on Fiber Composites, High Performance Concretes, and Smart Materials*, Ed. By V.S. Parameswaran, Pub. Allied Publishers Private Limited, New Delhi, India, 2004, pp. 57-74.

[38] Kabele, P., "Assessment of Structural Performance of Engineered Cementitious Composites by Computer Simulation", *CTU Report 4*, Czech Tech. University, Prague, 2001.

[39] Mindess, S., Young, J. F., and Darwin, D., *Concrete*, *2nd Edition*, 2003.

[40] Adamson, A. W., *Physical Chemistry of Surfaces, 6th Edition*, John Wiley and Sons, Inc., 1997.

[41] Wittman, F. H., "Interaction of Hardened Cement Paste and Water," *Journal of the American Ceramic Society*, Vol. 56, No. 8, 1973, pp. 409-415.

[42] Yates, D. J. C., "Molecular Specificity in Physical Adsorption," *Advances in Catalysis and Related Subjects*, Academic Press Inc., Vol. 12, 1960, pp. 265-312.

[43] Flood, E .A., and Heyding, R. D., "Stresses and Strains in Adsorbent-Adsorbate Systems," *Canadian Journal of Chemistry*, Vol. 32, 1954, pp. 660-682.

[44] Wittmann, F. H., "Surface Tension, Shrinkage and Strength of Hardened Cement Paste," *Materials and Structures*, Vol.1, No. 6, 1968, pp. 547-552.

[45] Wittmann, F. H., "The Structure of Hardened Cement Paste - A Basis for a Better Understanding of the Materials Properties," *Hydraulic Cement Paste: Their Structure and Properties*, Cement and Concrete Association, Slough, United Kingdom, 1976, pp. 96-117.

[46] Wittmann, F. H., "Creep and Shrinkage Mechanisms," *Creep and Shrinkage in Concrete Structures*, Eds. Z. Bazant and F. H. Wittmann, J. Wiley and Sons Inc., 1982, pp.129-161.

[47] Weimann, M. B., "Vergleichende Studie der hygrischen Eigenschaften ausgewählter Werkstoffe des Bauwesens," *Building Materials Reports No. 14*, Aedificatio Verlag GmbH, Freiburg, Germany, 2001.

[48] Weimann, M. B., and Li, V. C., "Hygral Behavior of Engineered Cementitious Composites (ECC)," *International Journal for Restoration of Buildings and Monuments*, Vol. 9, No 5, 2003, pp513-534.

[49] Beltzung, F., Wittmann, F. H. and Holzer L., "Influence of Composition of Pore Solution on Drying Shrinkage," *Creep, Shrinkage and Durability Mechanics of Concrete and other Quasi-Brittle Materials*, Eds. Ulm, F. J., Bazant, Z .P. and Wittmann, F. H., Elsevier Science Ltd., 2001, pp. 39-48.

[50] Schubert, H., *Kapillarität in porösen Feststoffsystemen,* Springer-Verlag, Berlin, Germany, 1982.

[51] Hiller, K. H., "Strength Reduction and Length Changes in Porous Glass Caused by Water Vapour Adsorption," *Journal of Applied Physics*, Vol. 35, No. 5, 1964, pp. 1622-1628.

[52] **A**merican **S**ociety for **T**esting and **M**aterials (U.S. Code Organization).

[53] Wittmann, F. H., and Martinola, G., "Decisive Properties of Durable Cement-Based Coatings for Reinforced Concrete Structures," *International Journal for Restoration of Buildings and Monuments*, Vol. 9, No 3, 2003, pp. 235-264.

[54] Greenspan, L., "Humidity Fixed Points of Binary Saturated Aqueous Solutions," *Journal of Research of the National Bureau of Standard – American Physics Chemistry,* 81A, 1, January-February 1977.

[55] Weiss, W. J., and Ferguson, S., "Restrained Shrinkage Testing: the Impact of Specimen Geometry on Quality Control Testing for Material Performance Assessment," *Concreep 6: Creep, Shrinkage, and Curability Mechanic of Concrete and Other Quasi-Brittle Materials*, ed., Ulm, F. J., Bazant, Z. P., and Wittman, F. H., Elsevier, August 22-24 Cambridge MA © 2001, pp. 645-651.

[56] Shah, S.P., Karaguler, M.E., and Sarigaphuti, M., "Effects of shrinkage-reducing admixtures on restrained shrinkage cracking of concrete," *ACI Materials Journal*, Vol. 89, No. 3, 1992, pp 291-295.

[57] Bentur, A., and Mindess, S., *Fibre Reinforced Cementitious Composites*, 1990, 449 p.

[58] **A**merican **A**ssociation of **S**tate **H**ighway and **T**ransportation **O**fficias, 1999.

[59] Wang, K., Jansen, D, Shah, S., Karr, A., "Permeability Study of Cracked Concrete," *Cement and Concrete Research*, Vol. 27, No. 3, pp. 381-393, 1997

[60] Emmons, P. H., "Concrete Repair and Maintenance Illustrated", American Society for Testing and Materials (U.S. Code Organization), 1994, pp. 155-164.

[61] Li, V. C., "High Performance Fiber Reinforced Cementitious Composites as Durable Material for Concrete Structure Repair," *International Journal for Restoration of Buildings and Monuments*, Vol. 10, No 2, pp 163–180, 2004.

[62] American Concrete Institute, *Concrete Repair Guide (ACI 546R-04)*, American Concrete Institute. Farmington Hills, MI. 2004

[63] FEMMASSE MLS: Computer Program for the Analysis of the Thermal and Mechanical Behavior of Hardening Concrete – User Manual 2006.

[64] Zhou, J., Li, M., Ye, G., Schlangen, E., Breugel, K. V., and Li, V. C., "Modeling the Performance of ECC Repair Systems under Differential Volume Changes," *Proc. 2nd Int'l Conf. on Concrete Repair (ICCRRR), Rehabilitation and Retrofitting*, Cape Town, S. Africa, November, 2008, pp1005-1009. Leiden: CRC Press/Balkema.

[65] Zhou, J., Ye, G., Schlangen, E., and van Breugel, K., "Modelling of Stresses and Strains in Bonded Concrete Overlays Subjected to Differential Volume Changes," *Theoretical Applied Fracture Mechanics*, No. 49, Vol. 2, pp. 199-205.

[66] Ackermann, G., "Structural behaviour of joints in composite structures of precast elements and in-situ concrete," *Adherence of Young on Old Concrete, Proc. 2nd Bolomey Workshop. Sion/Sitten, Switzerland, 1-2 April 1993,* F.H. Wittmann (ed.), Unterengstringen: Aedificatio, 1994, pp. 115-127.

CHAPTER 5

Influence of Material Ductility on Reflective Cracking in Overlay Repairs

Chapter 5 addresses the reflective cracking issues that are prevalent in concrete repairs, especially pavement overlay repairs. Reflective cracking is another major cracking mechanism that greatly affects concrete repair service life. It is caused by the brittle response of overlay material under high stress concentration induced by pre-existing joints or cracks in the substrate concrete. The approach in this study emphasizes the inherent ductility and strain hardening behavior of ECC repair materials to diffuse stress concentration, thereby fundamentally eliminating reflective cracking. To demonstrate this concept, experimental studies were conducted on a simulated HES-ECC overlay repair system, to evaluate its early-age and late-age behavior subjected to monotonic and fatigue flexural loading. Compared to the control HES-Concrete overlay system, the HES-ECC overlay system exhibits 100% increased load carrying capacity and significantly prolonged fatigue life, both at ages of 6 hours and 28 days. This

methodology of suppressing reflective cracking can be generalized as translating the ductility of the repair material to the durability of the repair system, when subjected to stress concentration from existing cracks.

5.1 Introduction

In concrete repairs, especially overlay repairs, premature reflective cracking is often the ultimate failure mode that limits the repair service life[1,2,3]. Concrete or hot mix asphalt (HMA) overlays primary methods for rehabilitating distressed asphalt and Portland cement concrete pavements subjected to moderate and heavy traffic, including highways, bridge decks and airfields[4]. Before the more expensive option of removal and re-construction of existing pavements are undertaken, overlays can be used to provide smooth surfaces while utilizing the structure of existing concrete pavements[5,6]. Reflective cracking is often the first distress that occurs in overlays[7]. It is characterized as new cracks reflected through the overlay from pre-existing cracks or joints in the substrate (Figure 1.6) under repeated traffic loads. In most cases cracks propagate through the new overlay during the first few years of service[8]. Under severe conditions, a reflective crack can reach the surface of a 150 mm (6 in.) overlay in less than one year[9]. Reflective cracking not only reduces the overlay load carrying capacity and service life, but also provides a path for aggressive agents to infiltrate the pavement or bridge deck structure and cause early deterioration[10].

Traditionally, efforts undertaken to reduce reflective cracking in overlay repairs have fallen into three broad categories[11]: (a) concrete slab fracturing, which includes rubblization, crack and seat (for plain concrete pavement), and break and seat (for

reinforced concrete pavement); (b) stress-relieving interlayer, which is used between the concrete substrate and overlay, and includes paving fabric, modified HMA interlayer, geogrid, and other proprietary interlayers; and (c) modified overlay, which includes increasing overlay strength, increasing overlay thickness, adding fiber reinforcement, introducing saw and seal joints in HMA overlay, etc. If used appropriately, these methods can delay reflective cracking to a certain extent, although they will not fundamentally eliminate the fracture failure of the overlay. The advantages and drawbacks associated with these techniques will be briefly discussed below.

Through the crack and seat technique (Figure 5.1), numerous cracks are created in the existing concrete pavement slab to allow deformation of the concrete to occur at more locations and diffuse the stress concentration[12]. Similarly, the break and seat technique breaks the pavement into shorter slabs, thereby reducing the movements at the joints and cracks to prevent reflective cracking. However, these initial fracturing processes have not been successful[13]. Even with the reduced movements of the smaller slabs, cracks eventually reflect through the overlay. Rubblization (Figure 5.2**)** involves an extreme reduction of the slab length. It breaks the existing pavement into fragments that range in size from grains of sand to approximately 100 mm (4 in.) to 200 mm (8 in.) in width. As it completely destroys the concrete's slab action by breaking it down into crushed-stone sized fragments, it is an attempt to turn the existing pavement into base course. Rubblization is generally considered to be a more favorable approach to reducing reflective cracking among these three repair options[14,15]. However, there is one notable shortcoming to this analogy: a rubblized pavement has no gradation or density control, which are required by specifications for base course[16]. Also, rubblization destroys the

main structural component of the pavement system and reduces its load carrying capacity, such that a thicker overlay is required to compensate[17,18]. Although perceived as a rehabilitation technique to delay reflective cracking and quick deterioration of the overlay, rubblization is actually a destructive procedure; it destroys the structure of the existing concrete slab and weakens the entire pavement system[13,19,20].

As the concrete slab fracturing technique sacrifices the pavement integrity to reduce stress in the overlay induced by substrate movements, the stress-relieving interlayer method relies on an additional low-modulus layer of material to diffuse stress concentration. Stress-relieving interlayer performance can vary greatly; the type of interlayer chosen depends on overlay thickness, interlayer placement, base layer stability, and surface preparation[21]. Interlayers, such as paving fabrics (Figure 5.3), can form a waterproof layer of protection above the base layer, even after severe reflective cracking[22], and some studies have found they can retard development of overlay cracks[21,23,24]. However, previous studies, including a large-scale assessment by the Illinois DOT[25], have found that fabric interlayers and HMA interlayers (Figure 5.4) only retard reflective cracking by at most 3 years and are not cost effective.

As opposed to the repair methods described above, the modified overlay technique relies on improving the performance of the overlay itself. Increasing overlay thickness or increasing overlay material strength (e.g. using high strength concrete) both emphasizes increasing the margin between the traffic-induced stress in the overlay and the overlay material's tensile strength. A thicker overlay may delay the reflective crack from reaching the overlay surface if the crack is propagating by fatigue mode. These two methods have shown marginal improvement on overlay resistance to reflective cracking[26],

mainly because they do not provide abatement for tensile stress concentration in the overlay. Moreover, increasing overlay thickness may compromise cost-effectiveness because it greatly increases material usage, considering the long miles of pavement. Increasing the compressive strength of concrete materials also increases the material Young's modulus, correspondingly increasing the stress level at the same level of deformation. It also increases brittleness of the concrete material, leading to an increased susceptibility to fracture failure[27]. As for the saw and seal joint method (Figure 5.5), the state DOTs have documented their experiences with marginal to good results[28,29]. Secondary reflective cracking can occur, unless the saw cut is made within 25 mm (1 in.) from the existing joint/crack in substrate. The timing of when the cut is made has been found to be critical for preventing reflective cracking[28,29]. Furthermore, the presence of joints in overlay may necessitate additional maintenance[11].

The effectiveness of current approaches in eliminating reflective cracking in pavement overlays is limited[30]. For example, according to the Illinois DOT[31], on average HMA overlay with rubblized concrete pavement can extend pavement service life for 1-2 years. This amount of extension in service life is beneficial, yet not significant considering the continuously aging and deteriorating US highway infrastructure, and the declining funding for repair and rehabilitation. A new approach, which effectively addresses this repair failure mode and greatly extends the service life of the overlay system, is necessary for significantly improving the durability of concrete infrastructure.

5.2 Ductile ECC Overlay

The proposed approach in this study utilizes the inherent tensile ductility and strain hardening behavior of ECC materials to fundamentally eliminate reflective cracking initiated from underlying cracks in the substrate concrete. Without relying on an increase in overlay thickness, fracturing substrate concrete, and application of stress relieving interlays, a ductile overlay would be able to diffuse stress concentrations and prevent propagation of cracks to the overlay surface. This concept, which is investigated in an overlay case within this study, can be generalized to many surface repair scenarios where underlying cracks or joints exist in substrate concrete, e.g. surface repairs of dams, building floors, retaining walls and viaducts, tunnels, and pools.

The concept of ductile ECC overlays was first investigated by Lim and Li (1997)[32] and Kamada and Li (2000)[33] using a special version of ECC, containing a Type I Portland cement based matrix and short polyethylene fibers (PE-ECC). It was found that under monotonic flexural loading, PE-ECC effectively diffused stress concentrations through its microcracking behavior at the base of the overlay. The multiple microcracking process of the PE-ECC overlay absorbed over ten times the energy that was absorbed in the brittle fracture (reflective cracking) process of the control concrete overlay. Later, Zhang and Li (2002)[34] conducted an experimental study and analytical analysis on the overlay performance of another version of ECC, containing Type I Portland cement based matrix and short polyvinyl alcohol fibers (PVA-ECC), under monotonic and fatigue flexural loading. The experimental results revealed great improvements in both load carrying capacity and fatigue life of the PVA-ECC overlay system, compared to the control concrete overlay system. Recently, Zhang et al. (2007)[35]

and Qian (2007)[11] looked at the overall sustainability of unbonded concrete overlays, HMA overlays, and PVA-ECC overlays using economic, environmental, and social metrics. It was found that ECC overlays were able to improve the sustainability of rigid pavement overlays by reducing surface roughness (improving vehicle fuel economy) and extending overlay service life. A 39.2% or 55.7% reduction in total costs was able to be achieved when using ECC overlay compared with concrete or HMA overlay. ECC overlay was also found to reduce total primary energy consumption by 75% compared with HMA overlay and greenhouse effect was reduced by 32 to 37% compared with concrete and HMA overlay.

These research findings revealed the great potential of ECC as a durable overlay material that extends the service life of pavement infrastructure. The motivation behind this research is to understand the performance of the new HES-ECC material, which was developed in this thesis specifically for concrete repair applications, in term of its resistance to reflective cracking. Differing from previously investigated ECC materials, HES-ECC contains a Type III Portland Cement based matrix, and simultaneously possesses unique tensile properties as well as rapid early-age strength gain rate. Of special interest is the early-age performance of HES-ECC overlays. This study looked at the 6-hour and 28-day cracking behavior, load carrying capacity, deformation carrying capacity, and fatigue life of the HES-ECC overlay system compared to a control HES-Concrete overlay system. Influence of concrete substrate surface preparation on the overlay system's overall performance was also evaluated and reported here.

5.3 Experimental Program

5.3.1 Specimen Configuration and Loading Conditions

Traffic loading induces flexural stresses in the overlay and substrate slab. These stresses in the overlay are at a maximum at and/or close to the existing cracked section, because there is no load transfer through the existing cracks[36,37]. Additionally, due to the dimensional incompatibility between the cracked pavement substrate and overlay, a certain amount of interfacial delamination, starting from the existing cracks, will form[34]. As a result, the maximum flexural stress zone is extended to the region from the existing cracks to the endpoints of the delamination zone on each side.

To simulate the scenario described above, an overlay repair system subjected to four-point bending[32,33,34] was employed in this study. As shown in Figure 5.6, this system consisted of a 51 mm (2 in.) thick layer of repair material cast on a 51 mm (2 in.) thick old concrete substrate. This concrete substrate, which was 356 mm (14 in.) long and 76 mm (3 in.) wide, contained a vertical crack that simulated an existing crack or joint in pavement, and a 51 mm (2 in.) long horizontal interfacial crack that simulates the initial delamination between the overlay and substrate. The specimen was subjected to a four-point bending load, with the load-deflection curve monitored during testing. The deflection of the specimen at the center was measured by two linear variable differential transducers (LVDTs), which were mounted on both sides at the center of the overlay.

Both the monotonic and cyclic loading tests were conducted on a 56 kip load capacity MTS-810 testing machine equipped for closed-loop testing. The monotonic flexural test was carried out with deformation controlled by the displacement of the actuator. The displacement was increased at a constant rate of 0.1 mm/min (0.004

in./min) according to ASTM C1018[38]. The fatigue flexural test was conducted with load controlled using a sinusoidal waveform with a frequency of 2 Hz. Loading followed a ramp function to the maximum load P_{max} at a rate of 0.1 kN/s (22.5 lb/s), followed by sine waveform fatigue loading cycles. The maximum load (P_{max}) was 90%, 80% and 70% of the average load-carrying capacity of the overlay system, which was obtained from the monotonic flexural test results. The ratio R between the minimum and maximum load levels was constant at $R=P_{min}/P_{max}=0.1$. Three specimens were tested for each scenario.

5.3.2 Materials and Specimen Preparation

HES-ECC (developed in chapter 2) and HES-concrete (control mix) were investigated in this study. They were the same as those high early strength materials investigated in the repair layer system subjected to restrained shrinkage in Chapter 4. Their mixing proportions and mechanical properties are summarized in Table 4.2, 4.3 and 4.4. The HES-Concrete mixture consisted of coarse aggregate (CA) with 10 mm (0.4 in) nominal grain size, Portland type III cement (C), sand (S) and water (W). Superplasticizer (SP) was used to achieve sound workability. Accelerating admixtures (AC) were also included to accelerate the material's strength development and setting processes. HES-Concrete specimens were tested to have average compressive strength (f_c') of 49.9 MPa (7234 psi) at the age of 7 days, and 54.2 MPa (7860 psi) at the age of 28 days. Under uniaxial tensile loading, HES-Concrete is a brittle material with sudden fracture failure on a single crack plane.

The HES-ECC mixture is comprised of Type III Portland cement (C), water (W),

silica sand (S) with 110 μm (3.94×10^{-3} in.) nominal grain size, polystyrene beads with a size of 4 mm (0.157 in.) as aggregates, superplasticizer, accelerating admixtures, and 2% (V_f) polyvinyl-alcohol (PVA) fibers. These PVA fibers had a length of 12 mm (0.472 in) and diameter of 40 μm (1.54×10^{-3} in). The HES-ECC was self-consolidating in the fresh state. The polystyrene beads served as deliberately introduced initial flaws to assist in triggering the multiple microcracks during tensioning of the composite. As measured in Chapter 2, the HES-ECC mixture had average compressive strength of 47.5 MPa (6885 psi) at the age of 7 days, and 55.6 MPa (8063 psi) at the age of 28 days. Its average Young's modulus was 20.6 GPa (2986 ksi) at the age of 7 days, and 23.2 GPa (3365 ksi) at the age of 28 days, which was lower than that of HES-Concrete (26.2 GPa (3803 ksi) at 7 days; 27.8 GPa (4025 ksi) at 28 days) due to the absence of coarse aggregates (CA). The HES-ECC mixture also had a tensile strain capacity between 3 – 6% at all ages. Its flexural strength (MOR) was 13.6 MPa (1965 psi) at the age of 7 days, and 15.1 MPa (2188 psi) at the age of 28 days.

The substrate concrete had the same material composition as HES-Concrete, except that it used ordinary concrete containing Portland type I cement while the HES-Concrete repair used Type III Portland cement.

To prepare the specimens, concrete beams with dimensions of 356 mm × 76 mm × 102 mm (14 in × 3 in × 4 in) were first cast, and demolded after 24 hours. After demolding, the beams were cured in water at 20±1 °C (66-70 °F) for 28 days. Then each beam was cut using a diamond saw into four concrete blocks with size of 178 mm × 76 mm × 51 mm (7 in ×3 in × 2 in) (Figure 5.7 (a)). The blocks were then stored in laboratory conditions of 45 ± 5% RH and 20±1 °C (66-70 °F) for an additional week, at

which time smooth plastic tape was used to form the vertical crack and horizontal interfacial crack before the repair layer was cast (Figure 5.7 (b)).

The contact surfaces of the concrete substrates were prepared in two different ways: (a) diamond saw cut smooth, and (b) roughened to 7~8mm (Figure 5.8). For the latter, the substrate surfaces were roughened while in the fresh state by using a chisel to remove slurry cement from the external surfaces of coarse aggregates. Before placing the repair layers, the substrate surfaces were re-cleaned with a brush and high-pressure air to ensure a clean bonding surface, and then they were dampened to an adequate moisture level. HES-ECC or HES-concrete repair layer was cast on top of two concrete blocks that formed the concrete substrate. The repair layers were moisture cured for 6 hours and then demolded. After demolding, the layered specimens were moved into a room with ambient conditions of 45 ± 5% RH and 20±1 °C (66-70 °F). The test was conducted in the same room at specimen ages of 6 hours and 28 days. Three specimens were tested for each case.

5.4 Experimental Results

5.4.1 Overlay System Monotonic Flexural Performance

Figure 5.10 plots the flexural stress vs. midpoint deflection curve of the HES-ECC repair system compared with the HES-Concrete repair system under monotonic loading. The flexural stress $\sigma_{flexural}$ is the tensile stress at the center base of the overlay above the vertical crack, and was determined using linear elastic theory:

$$\sigma_{flexural} = \frac{M}{bh^2/6} \tag{5.1}$$

where M is the bending moment at the center of the overlay, b is overlay width, and h is the overlay thickness. The dimensions of the overlay, instead of the overlay system, were

used for calculation of $\sigma_{flexural}$ because there was no load transfer through the vertical crack. The flexural strength, or modulus of rupture (MOR), which was defined as the peak flexural stress from the flexural stress vs. deflection curve, is summarized in Table 5.1 and compared in Figure 5.11. The corresponding deflection and interfacial delamination length (including the 2 in. initial horizontal crack) upon overlay failure are summarized in Table 5.2 and 5.3, and Figure 5.12 and 5.13.

The *kinking and trapping mechanism*[32] was demonstrated in the HES-ECC overlay system at both early age (6 hours) and late age (28 days). According to Hutchinson and Suo (1992)[39], interfacial cracks can kink into the repair material when the crack tip satisfied the "interfacial crack kink condition", which contains two terms - relative driving force and relative toughness. The relative driving force term can be analytically or numerically calculated, and the relative toughness term can be experimentally measured based on the interface toughness and the toughness of the repair material. Lim (1996)[40] found that low initial fracture toughness with a rapid rise R-curve behavior of repair material, or low first crack strength with a large margin to ultimate tensile strength, are the essential requirements of the trapping mechanism in a repair system. These requirements are met by ECC materials (including HES-ECC), but are not satisfied by traditional concrete (including HES-Concrete) or FRC materials. Figure 5.9 shows the conceptual kinking and trapping mechanism of the ECC/concrete system with the load vs. displacement relationship. Large amounts of energy are dissipated during repeated sequences of kinking, ECC multiple microcracking, trapping, and interfacial crack propagation, so that fracture failure is prevented. In this study, the kinking and trapping mechanism was clearly observed in the HES-ECC overlay system at ages of 6

hours and 28 days. With this mechanism, the HES-ECC overlay system effectively diffused the stress concentration from the initial vertical crack and horizontal interfacial crack by trapping the cracks within the HES-ECC overlay, without reflecting them to the overlay surface (Figure 5.14). Thus, the HES-ECC overlay exhibited a ductile ultimate failure mode in flexure. In contrast, the control HES-Concrete overlay system exhibited a brittle fracture failure mode, with the existing crack quickly reflected to the overlay surface (Figure 5.10). These results indicate that an HES-ECC overlay can be effective in resisting reflective cracking as early as 6 hours after placement.

Although HES-ECC and HES-Concrete have similar 28-day compressive strength, the HES-ECC overlay system achieved significantly higher flexural load carrying capacity than the HES-Concrete overlay system at the same overlay age (Table 5.1 and Figure 5.11). This is due to the tensile strain-hardening behavior of HES-ECC and the resulting different cracking mechanisms discussed above. The flexural strength (MOR) of the HES-ECC overlay was approximately 100% larger than that of the HES-Concrete overlay, at both ages of 6 hours and 28 days, and in both smooth surface and rough surface situations. Furthermore, the deformation capacity of the HES-ECC overlay system, represented by the overlay midpoint deflection corresponding to the peak flexural stress, was approximately 700% (smooth surface) and 500% (rough surface) larger than those of the HES-Concrete overlay system, respectively. The significantly higher load carrying capacity as well as deformation capacity of HES-ECC overlay suggests it has a higher resistance to reflective cracking, even in heavy traffic areas.

It should be noted that the flexural strength (MOR) of HES-ECC overlay at age of 6 hours (9.65 MPa [smooth]; 9.51 MPa [rough]) is slightly higher than that of HES-

Concrete overlay at age of 28 days (9.09 MPa [smooth]; 8.67 MPa [rough]). This early-age load carrying capacity of HES-ECC overlay confirms its capability of early opening to traffic 6 hours after placement. This advantage of HES-ECC overlay, in terms of its early-age load carrying capacity and resistance to reflective cracking, has not been demonstrated in other versions of ECC materials or traditional concrete or FRC materials.

Comparing the flexural curves of the HES-ECC repaired system with two differently prepared substrate surfaces, higher deformation capacity was noted when the substrate surface was smooth (Table 5.2, Figure 5.10 and 5.12). This phenomena was consistent with findings from previous studies[33,34], and was additionally revealed at the early age of the HES-ECC overlay. Due to the weak bond of the smooth interface, under flexural load a larger delamination area was formed between the HES-ECC repair layer and the concrete substrate. Thus, a larger section of the HES-ECC overlay (the delaminated section) was subjected to maximum bending stress and underwent the kinking-trapping and multiple microcracking processes, leading to a higher deformation capacity. The interfacial delamination was measured, including the initial 2-in. delamination length, and is shown in Figure 5.13. For the HES-Concrete overlay system, the influence of interface properties on deformation capacity was negligible. In both smooth and rough interface cases, the initial interface crack kinked out from the interface into the HES-Concrete overlay and propagated unstably to the overlay surface. This phenomenon corresponds to a sudden load drop without any interface delamination (Figure 5.10 and 5.13).

The typical cracking pattern of the HES-ECC overlay system compared with the HES-Concrete overlay system is shown in Figure 5.14. Corresponding to the peak

applied flexural stress, the HES-Concrete/Concrete overlay system had a sudden failure with one single crack propagating through the HES-Concrete overlay. The fractured halves of the overlay specimens separated completely in both the smooth and rough interface cases. In contrast, the HES-ECC/Concrete overlay system exhibited multiple microcracking behavior without reflective cracking failure. Before the HES-ECC overlay eventually failed in ductile flexural mode, it experienced deflection hardening with self-controlled crack width below 50 μm (2×10^{-3} in.), in both smooth and rough interface cases. The results show that the unique kink-trap mechanism in HES-ECC overlays effectively suppressed the common reflective failure mode in concrete repairs. Similar behavior was also found in regular ECC (M45) overlays[34].

5.4.2 Overlay System Fatigue Performance

The fatigue flexural performances of HES-ECC and HES-Concrete overlay systems are shown in Figure 5.15, in terms of flexural stress versus fatigue life (S-N). There was no obvious difference in the crack patterns at failure between the applications of fatigue and monotonic flexural loading conditions. At a certain number of cycles of loading, the HES-Concrete overlay system failed with a single crack unstably propagating to the overlay surface. In contrast, the HES-ECC overlay system underwent multiple microcracking at the base of the ECC overlay, preventing the initial crack from unstably "reflecting" through to the surface. It was also observed that as the fatigue stress level decreased, the number of microcracks also decreased. In this way, it became more difficult for the HES-ECC overlay to reach saturated multiple microcracking because the material was under lower stress and strain levels. Such phenomenon was

also observed by Qian (2008)[11] and Matsumoto et al. (2002) in regular ECC beam specimens[41]. During a fatigue test with constant stress level, fatigue load cycles repeatedly re-opened the microcracks in HES-ECC overlay, until the fiber bridging capacity at one of the microcracks was exhausted under fatigue, leading to the final overlay failure. Because of significant difference in the failure modes of HES-Concrete and HES-ECC overlay systems under fatigue, it was clearly observed from Figure 5.15 that at the same overlay age of 28 days, and at the same level of applied maximum flexural stress, the fatigue life of the HES-ECC overlay system was several orders of magnitude higher than that of the HES-Concrete repair system. Additionally, comparing the HES-ECC overlay system at the age of 6 hours with the HES-Concrete overlay system at the age of 28 days, the former had a fatigue life approximately one order of magnitude higher at the same stress level. These results suggest that when designed with equal thickness, HES-ECC overlays can have a drastically longer service life than HES-Concrete overlays under the same traffic loading conditions. In other words, under equal service life and traffic loading conditions, the required overlay thickness of an HES-ECC overlay can be significantly lower than that of an HES-Concrete overlay, leading to large savings of overlay material, equipment use, and construction time.

The difference in interface roughness did not significantly affect the fatigue life of the HES-ECC and HES-Concrete layered repair systems. The hypothesis was that the flexural fatigue life of a beam was dominated by the single crack propagation behavior under fatigue loading[42]. For the HES-ECC overlay, its fatigue life until failure was likely governed by the fiber bridging properties under cyclic loading at the dominant single crack, and did not significantly depend of the number of microcracks formed. However,

the number of microcracks was positively correlated with the deformation capacity of the HES-ECC overlay upon fatigue failure, as was similarly observed in the monotonic flexural testing results.

5.5 Conclusions

The common durability concern in concrete repairs, reflective cracking, can be fundamentally prevented through the high tensile ductility and strain-hardening behavior of ECC materials. This was demonstrated in this study of an HES-ECC overlay system with an existing vertical crack in the substrate concrete and a small amount of interfacial delamination. Under monotonic and fatigue four-point bending, the HES-ECC overlay exhibited a "kinking and trapping" mechanism, and multiple microcracking behavior with controlled crack width below 50 μm (2×10^{-3} in.). Through this process a large amount of energy was dissipated, thus preventing the brittle reflective cracking failure mode that was observed in the control HES-Concrete overlay system.

Due to the ductile tensile behavior and unique "kinking and trapping" mechanism of the HES-ECC overlay, it exhibited 100% higher load carrying capacity and several orders of magnitude longer fatigue life compared to an HES-Concrete overlay with similar compressive strength and the same age. This suggests that significant improvements are possible in overlay design when HES-ECC is used: assuming the same loading conditions, (a) if designed with same overlay thickness, the HES-ECC overlay is expected to have a significantly longer service life than traditional concrete overlays; (b) if designed with same service life, the HES-ECC overlay thickness can be greatly reduced compared to traditional concrete overlays, leading to a significant amount

of saving of materials, construction equipment, and construction time; or (c) a compromise of either parameter, i.e. reduced overlay thickness as well as prolonged overlay service life, can be achieved simultaneously.

It should be noted that the high resistance to reflective cracking of the HES-ECC overlay through multiple microcracking and the "kinking and trapping" mechanism was also observed at the early age of 6 hours. The load carrying capacity of the HES-ECC overlay at the age of 6 hours and the control HES-Concrete overlay at the age of 28 days was the same. Furthermore, at the same stress level, the fatigue life of the HES-ECC overlay at the age of 6 hours was approximately one order magnitude larger than that of the control HES-Concrete overlay. All of these results highlight the significant advantages of the newly-developed HES-ECC material in fast and durable repair applications, with shortened operations shutdown time as well as greatly prolonged service life. These potentials in HES-ECC have not been demonstrated in other versions of ECC materials, or traditional concrete or FRC materials.

Table 5.1 – Modulus of rupture of HES-ECC and HES-Concrete overlays under monotonic loading.

	Overlay Age	6 hours	28 days
MOR, psi (MPa)	HES-ECC [Smooth]	1513.32 (10.43) 1315.06 (9.07) 1371.62 (9.46)	2725.38 (18.79) 3095.92 (21.35) 2877.19 (19.84)
	Average	*1400.00 (9.65)*	*2899.49 (19.99)*
	HES-ECC [Rough]	1527.83 (10.53) 1337.68 (9.22) 1270.97 (8.76)	2620.75 (18.07) 2861.51 (19.73) 2773.58 (19.12)
	Average	*1378.83 (9.51)*	*2751.95 (18.97)*
	HES-Concrete [Smooth]	657.02 (4.53) 604.81 (4.17) 570.00 (3.93)	1370.99 (9.45) 1201.88 (8.29) 1381.16 (9.52)
	Average	*610.61 (4.21)*	*1318.01 (9.09)*
	HES-Concrete [Rough]	548.24 (3.78) 661.37 (4.56) 510.53 (3.52)	1391.18 (9.59) 1318.67 (9.09) 1064.69 (7.34)
	Average	*573.38 (3.95)*	*1258.18 (8.67)*

Table 5.2 – Center deflection (upon failure) of HES-ECC and HES-Concrete overlays under monotonic loading.

	Overlay Age	6 hours	28 days
Deflection in. (mm)	HES-ECC [Smooth]	0.198 (5.02) 0.180 (4.56) 0.206 (5.22)	0.138 (3.51) 0.132 (3.35) 0.171 (4.34)
	Average	*0.194 (4.93)*	*0.147 (3.73)*
	HES-ECC [Rough]	0.118 (3.00) 0.100 (2.54) 0.131 (3.34)	0.075 (1.91) 0.112 (2.85) 0.095 (2.41)
	Average	*0.117 (2.96)*	*0.094 (2.39)*
	HES-Concrete [Smooth]	0.011 (0.28) 0.015 (0.37) 0.018 (0.45)	0.017 (0.43) 0.016 (0.41) 0.017 (0.43)
	Average	*0.014 (0.37)*	*0.017 (0.42)*
	HES-Concrete [Rough]	0.016 (0.41) 0.015 (0.37) 0.015 (0.39)	0.015 (0.38) 0.017 (0.43) 0.017 (0.43)
	Average	*0.015 (0.39)*	*0.016 (0.42)*

Table 5.3 – Interfacial delamination (upon failure, including initial delamination) of HES-ECC and HES-Concrete overlays under monotonic loading.

	Overlay Age	6 hours	28 days
Delamination in. (mm)	HES-ECC [Smooth]	7.34 (186.44) 7.62 (193.55) 7.93 (201.42)	7.07 (179.58) 6.45 (163.83) 6.12 (155.45)
	Average	*7.63 (193.80)*	*6.55 (166.29)*
	HES-ECC [Rough]	4.03 (102.36) 4.51 (114.55) 3.89 (98.81)	4.20 (106.68) 4.05 (102.87) 3.51 (89.15)
	Average	*4.14 (105.24)*	*3.92 (99.57)*
	HES-Concrete [Smooth]	2.00 (50.80) 2.00 (50.80) 2.12 (53.85)	2.08 (52.83) 2.12 (53.85) 2.05 (52.07)
	Average	*2.04 (51.82)*	*2.08 (52.92)*
	HES-Concrete [Rough]	2.00 (50.80) 2.01 (51.05) 2.07 (52.58)	2.05 (52.07) 2.10 (53.34) 2.06 (52.32)
	Average	*2.03 (51.48)*	*2.07 (52.58)*

Figure 5.1 – Crack-and-seated pavement surface.

Figure 5.2 – Rubblized pavement surface.

Figure 5.3 – Paving fabric installation.

Figure 5.4 – HMA interlayer installation.

Figure 5.5 – Overlay saw and seal

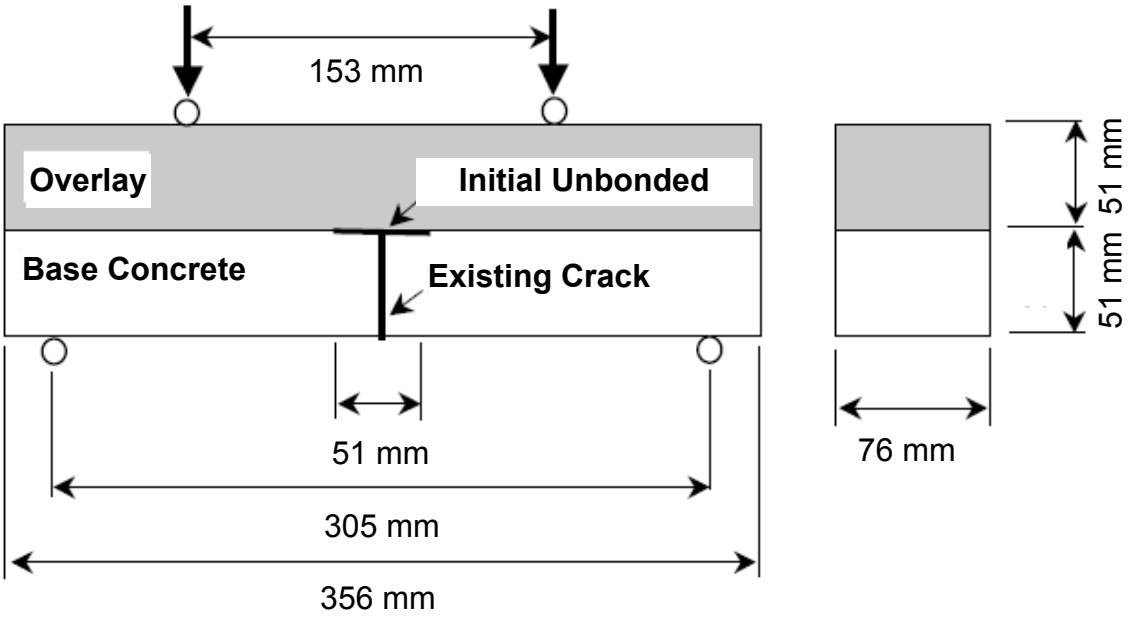

Figure 5.6 – Specimen confuguration and loading conditions.

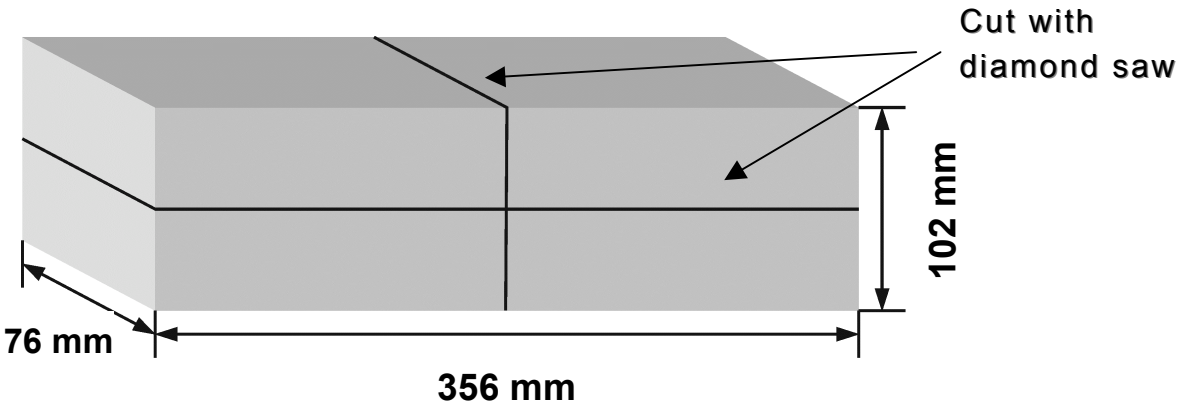

(a)

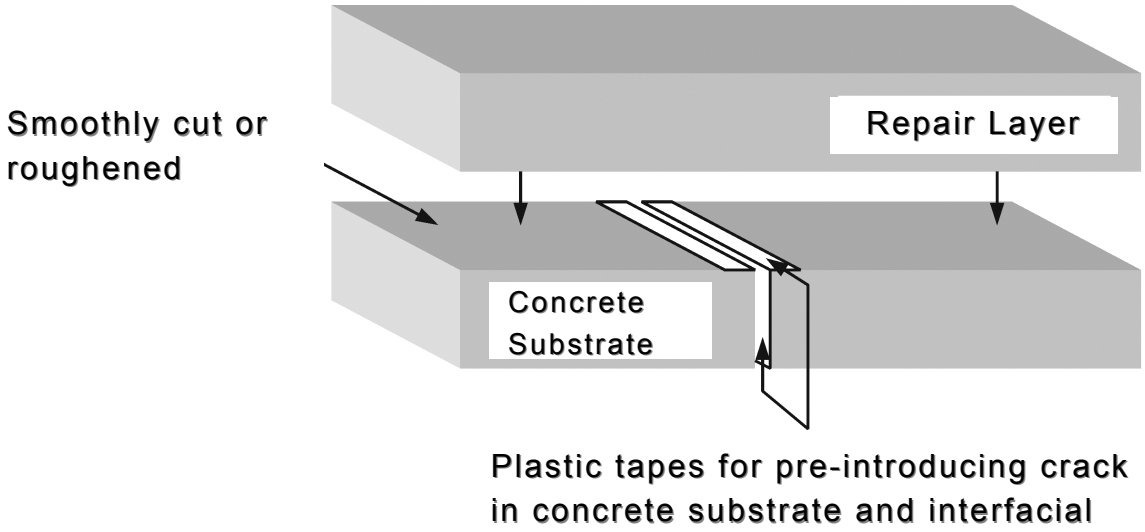

(b)

Figure 5.7 – Specimen preparation. (a) Concrete beams were cut into four blocks, two of which formed the concrete substrate with an initial vertical crack. (b) Overlay repair layer was cast onto the concrete substrate with an initial vertical crack and small amount of horizontal interfacial crack.

Figure 5.8 – Concrete substrate surface preparation.

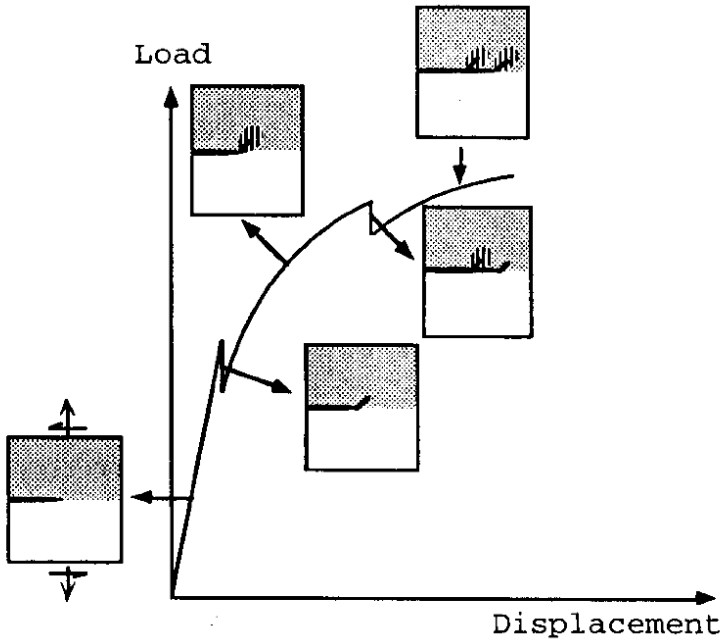

Figure 5.9 – "Kinking and trapping" mechanism[27].

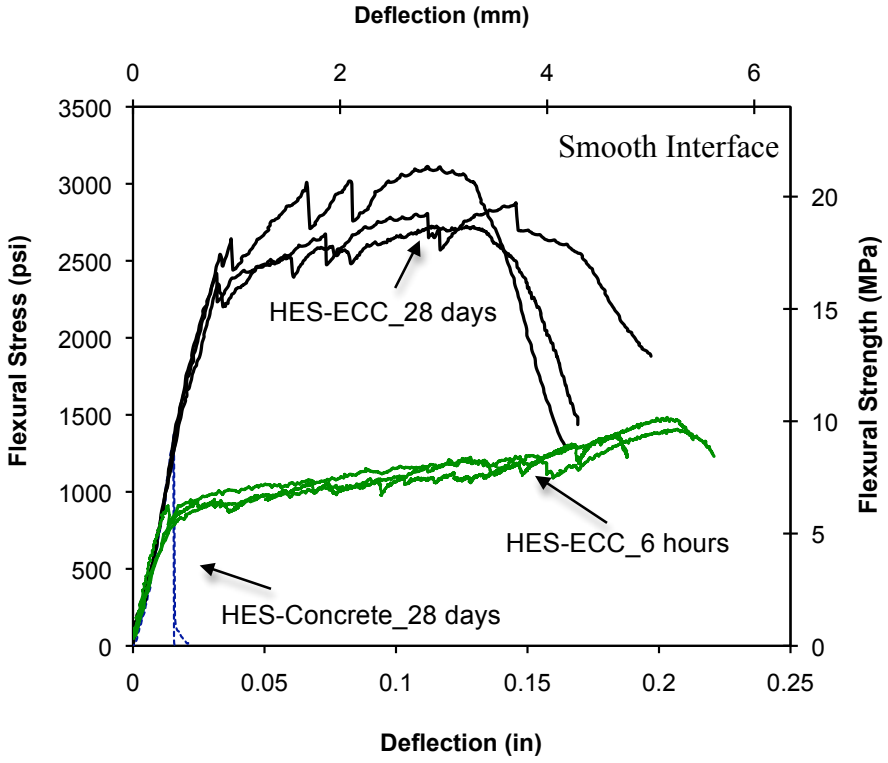

(a)

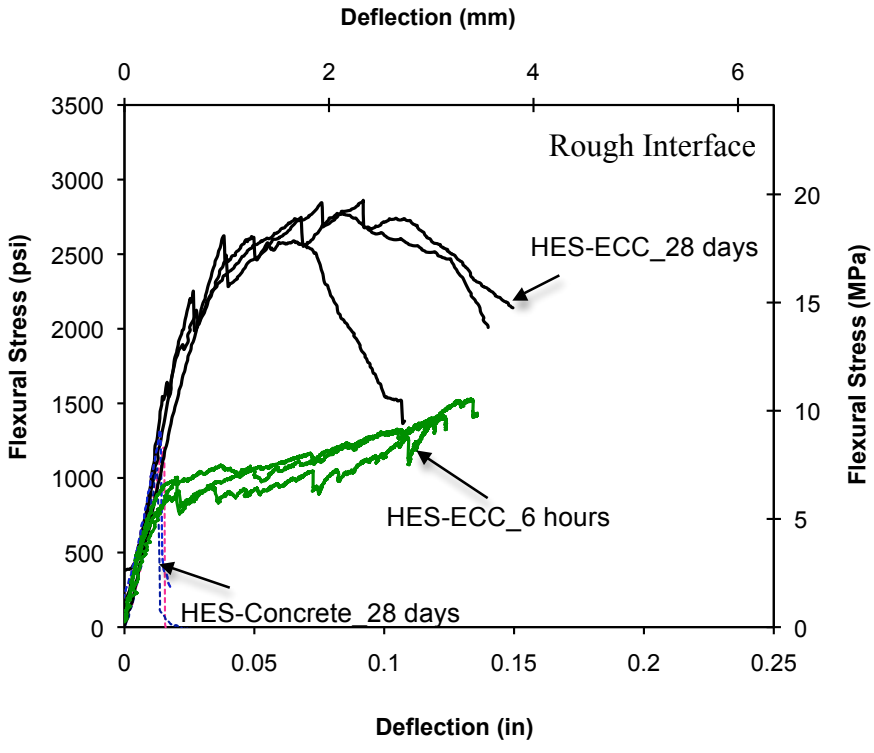

(b)

Figure 5.10 – Flexural behavior of HES-ECC and HES-Concrete layered repair system under monotonic loading: (a) smooth interface; (b) rough interface.

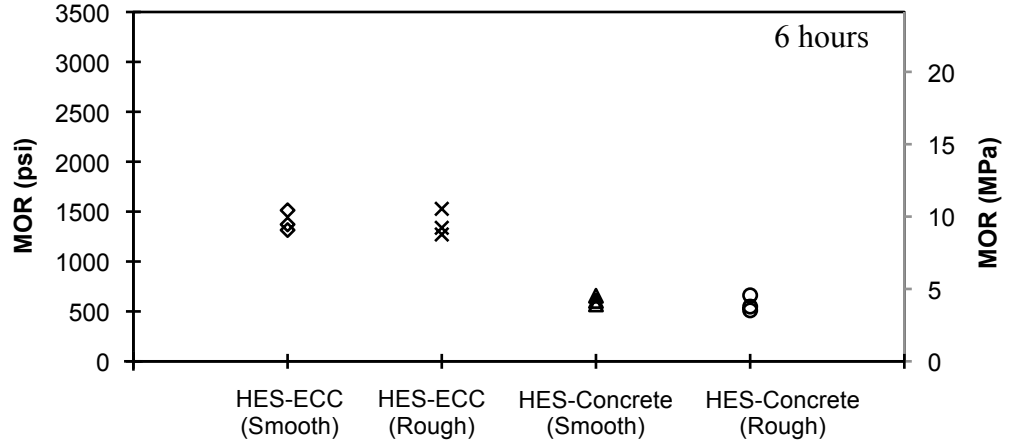

(a)

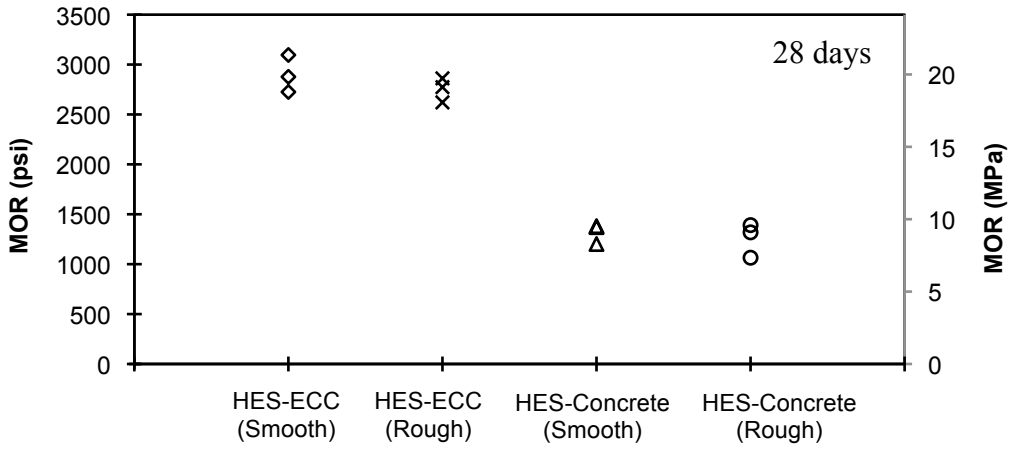

(b)

Figure 5.11 – Modulus of rupture (MOR) of HES-ECC and HES-Concrete overlay systems under monotonic loading. (a) Overlay age of 6 hours. (b) Overlay age of 28 days.

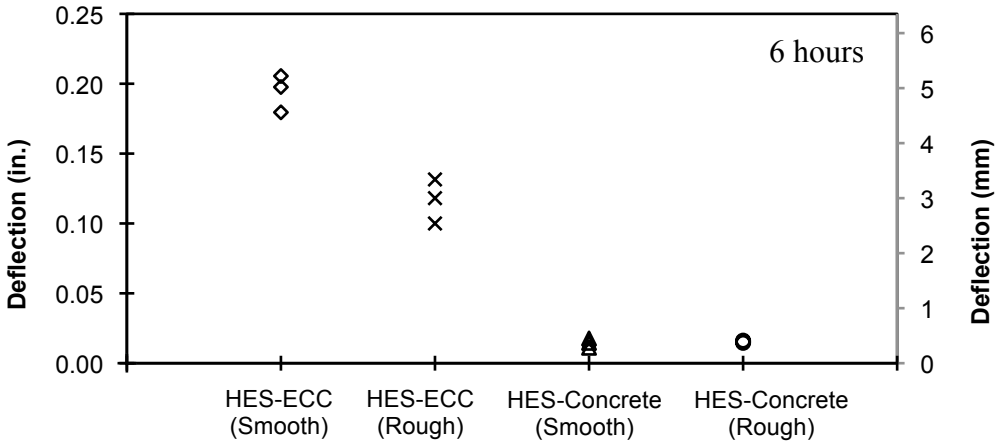

(a)

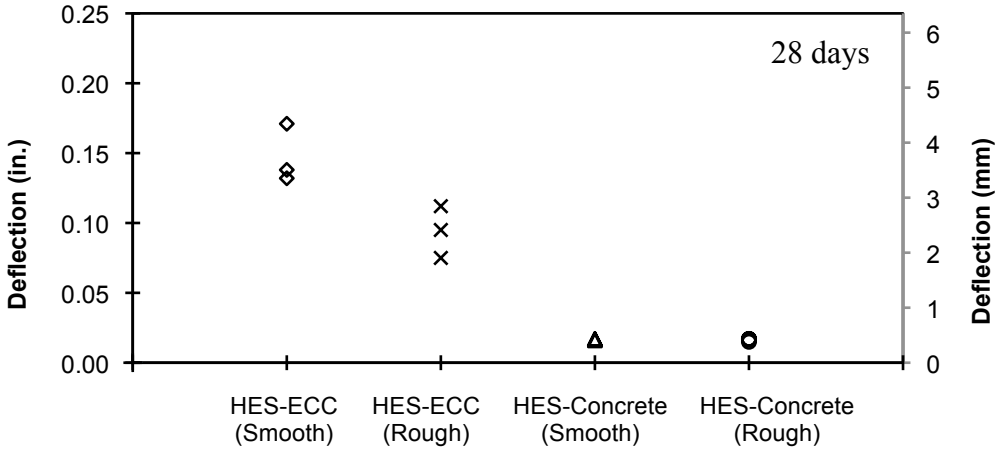

(b)

Figure 5.12 – Deflection at failure of HES-ECC and HES-Concrete overlay systems under monotonic loading. (a) Overlay age of 6 hours. (b) Overlay age of 28 days.

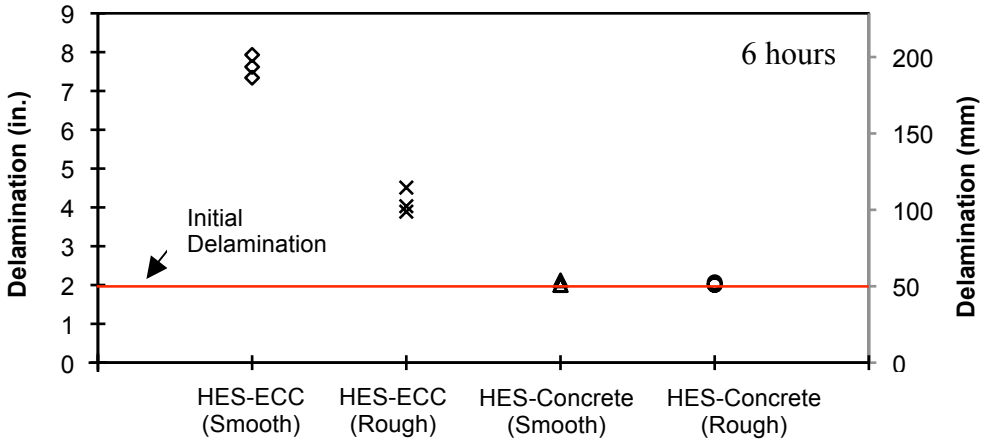

(a)

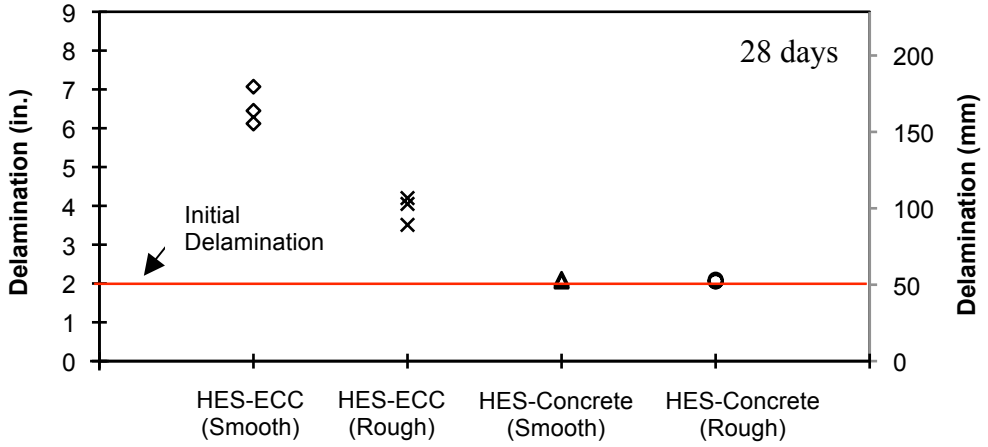

(b)

Figure 5.13 – Interfacial delamination upon failure of HES-ECC and HES-Concrete overlay systems under monotonic loading. (a) Overlay age of 6 hours. (b) Overlay age of 28 days.

(a) HES-ECC overlay system (smooth interface)

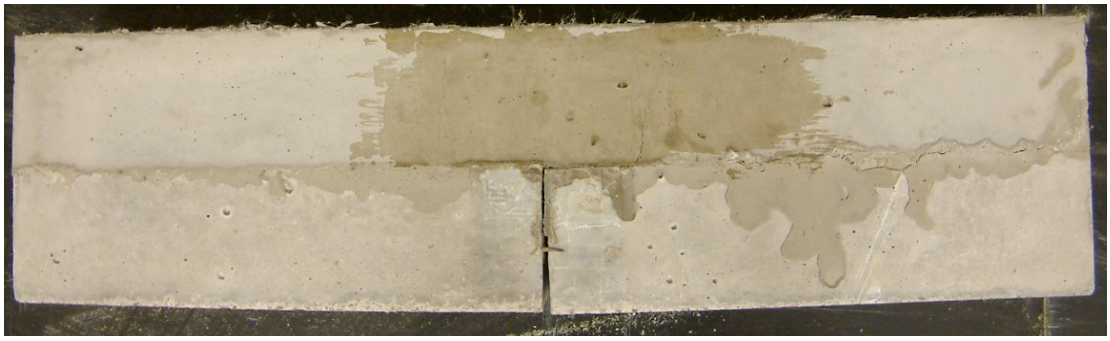

(b) HES-ECC overlay system (rough interface)

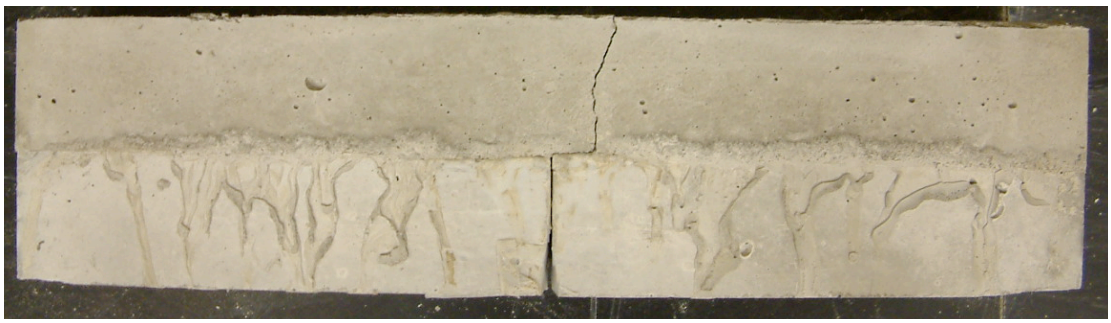

(c) HES-Concrete overlay system (smooth interface)

(d) HES-Concrete overlay system (rough interface)

Figure 5.14 – Crack pattern of HES-ECC and HES-Concrete overlay systems at overlay age of 28 days. Epoxy glue was spread over the cracking sections of HES-ECC overlays (a) and (b), to better visually reveal multiple microcracking.

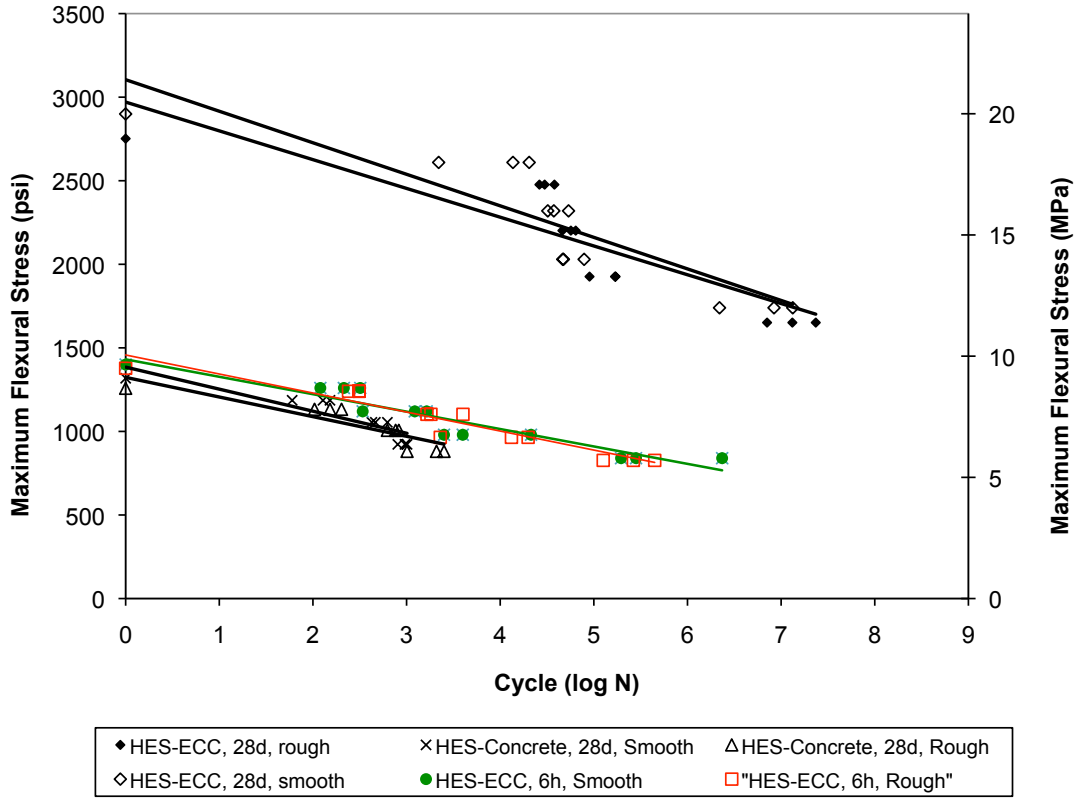

Figure 5.15 – Fatige stress-fatigue life relation (log) for HES-ECC and HES-Concrete overlay systems.

References:

[1] Tayabji, S. D. and Okamoto, P. A., "Thickness Design of Concrete Resurfacing," Proc., *3rd Int'l Conf. on Concrete Pavement Design and Rehabilitation*, 1985, pp. 367-379.

[2] ERES Consultants, Inc., "Evaluation of Unbonded Portland Cement Concrete Overlays," *NCHRP Report 415*, Transportation Research Board, Washington, D. C., 1999.

[3] Huang, Y. H., *Pavement Analysis and Design, 2nd edition*, Pearson Education, Upper Saddle River, NJ 07458.

[4] MDOT, *Pavement Design and Selection Manual*, Michigan Department of Transportation, Lansing, Michigan, 2005, 65p.

[5] Jones, H. W., "Asphalt Overlays; Crack & Seat vs. SAMI vs. Rubblizing vs. Removal How to Choose," *2009 Michigan Concrete Repair Seminar*, Michigan's Local Technical Assistant Program, Michigan Concrete Paving Association, Michigan Transportation Asset Management Council, Howell, Michigan, 2009.

[6] National Concrete Pavement Technology Center, *Guild to Concrete Overlays: Sustainable Solutions for Resurfacing and Rehabilitating Existing Pavements, Second Edition*, September 2008.

[7] Transport Research Board (TRB) of the National Academies, "Crumb Rubber Modified (CRM) Stress-Absorbing Membrane Interlayers for New Pavement Construction, Maintenance and Repair of Existing Pavements and Bridge Decks," *Research Needs Statements*, http://rns.trb.org/dproject.asp?n=13076, accessed on August 31, 2009.

[8] Newman, K., and Shoenberger, J. E., "Polymer Concrete Micro-Overlay for Fuel and Abrasion Resistant Surfacing: Laboratory Results and Field Demonstrations," US Army Engineer Research and Development Center, Vicksburg, Mississippi, USA, Presented for the *2002 Federal Aviation Administration Airport Technology Transfer Conference*, May 2002.

[9] RILEM Technical Committee 157-PRC, "Third RILEM International Conference Reflective Cracking in Pavements," *Materials and Structures*, Vol. 30, June 1997, pp. 317-318.

[10] National Concrete Pavemet Technology Center, *Guild to Concrete Overlay Solutions*, January 2007.

[11] Qian, S., "Influence of Concrete Material Ductility on the Behavior of High Stress Concentration Zones," *Ph.D. Dissertation*, University of Michigan, 2007.

[12] Harris, G. K., "Cracking & Seating to Retard Reflective Cracking – Fremont County," *Final Report*, Iowa Highway Research Board Research Project HR-279, 1993.

[13] American Concrete Pavement Association, "Rubblizing of Concrete Pavements: A Discussion of its Use," *Concrete Pavement Engineering and Research*,1998.

[14] DelDOT, *Design Guidance Memorandum on Concrete Pavement Rubblization*, Delaware Department of Transportation, 2002.

[15] Ceylan, H., Mathews, R., Kota, T., Gopalakrishnan, K., and Coree, B. J., "Rehabilitation of Concrete Pavements Utilizing Rubblization and Crack and Seat Methods," *Final Report* submitted to Iowa Highway Research Board and Iowa Department of Transportation, 2005, 156p.

[16] Guide Specifications for Highway Construction, American Association of State Highway and Transportation Officials, Washington, DC, 1993.

[17] FHWA, "Crack and Seat performance," *Review Report*, Demonstration Projects Division and Pavement Division, Federal Highway Administration, 1987.

[18] Freeman, T., "Final Report Evaluation of Concrete Slab Fracturing Techniques in Mitigating Reflective Cracking Through Asphalt Overlays," submitted to Virginia Transportation Research Council, Charlottesville, Virginia, VTRC 03-R3, 2002, 18p.

[19] Buncher, M., and Jones, H. W., "State-of-the-Practice: Rubblization of Airfield Pavements," *Concrete Pavement Engineering and Research*, American Concrete Pavement Association, 1998.

[20] Transportation Research Board, "Rubblization of Portland Cement Concrete Pavements," *Transportation Research Circular E-C087*, Washington, DC, January 2006.

[21] Zou, W, Wang, Z, and Zhang, H, "Field Trial for Asphalt Pavements Reinforced with Geosynthetics and Behavior of Glass-Fiber Grids," *Journal of Performance of Constructed Facilities*, Vol. 37, Sep/Oct 2007, pp. 361-367.

[22] Buttlar, W, Bozkurt, D, Dempsey, B, "Cost-Effectiveness of Paving Fabrics Used to Control Reflective Cracking," *Transportation Research Record*, No. 1730, 2000, pp. 139-149.

[23] Blankenship, P, Iker, N, Drbohlav, J, "Interlayer and Design Considerations to Retard Reflective Cracking," *Transportation Research Board*, No. 1896, 2004, 177-186.

[24] Penman, J, Hook, K.D., "The use of geogrids to retard reflective cracking on airport runways, taxiways and aprons," *Pavement Cracking: Mechanisms, Modeling, Detection, Testing and Case Histories*, 2008.

[25] Buttlar, W, Bozkurt, D, Dempsey, B, "Cost-Effectiveness of Paving Fabrics Used to Control Reflective Cracking," *Transportation Research Record*, Vol. 1730, pp. 139-149.

[26] Jiang, Y., and McDaniel, R. S., "Application of Cracking and Seating and Use of Fibers to Control Reflective Cracking, " Transportation Research Board, No. 1388, 1993, pp. 150-159.

[27] Li, V. C., and Stang, H., "Elevating FRC Material Ductility to Infrastructure Durability," *Proceedings of 6th RILEM symposium on FRC*, Varenna, Italy, 2004, pp. 171-186.

[28] Kilareski, W. P., and Bionda, R. A., "Structural Overlay Strategies for Joints Concrete Pavements," Vol. 1, *Report No. FHWA-RD-89-142*, FHWA, Washington, D. C., 1990.

[29] Hall, K. T., Correa, C. E., and Simpson, A. L., "Performance of Rigid Pavement Rehabilitation Treatments in the SPS-6 Experiment, " TRB, 1823, 2003, pp. 64-72.

[30] Lepech, M. D., Keolain, G. A., Qian, S., and Li, V. C., "Design of Green Engineered Cementitious Composites for Pavement Overlay Applications," *Int'l Association for Life Cycle Civil Engineering conference (IALCCE 08)*, Italy, June, 2008, pp. 837-842.

[31] Lippert, D. L., Rubblizing in Illinois (Presentation), Illinois DOT, 2003, 65p.

[32] Li, V.C. and Lim, Y.M., "Trapping Mechanism of Interface Crack at Concrete/Engineered Cementitious Composite Bimaterial", in Proc. of First International Conference on Damage and Failure of Interfaces - DFI-1 Vienna, pp. 405-409, Austria, 22-24 September, 1997.

[33] Kamada, T. and V.C. Li, "The Effects of Surface Preparation on the Fracture Behavior of ECC/Concrete Repair System," J. of Cement and Concrete Composites, Vol. 22, No. 6, pp.423-431, 2000.

[34] Zhang J., and Li, V.C., "Monotonic and Fatigue Performance in Bending of Fiber Reinforced Engineered Cementitious Composite in Overlay System ," *Journal of Cement and Concrete Research*, Vol. 32, No. 3, 2002, pp. 415-423.

[35] Zhang, H., G. A. Keoleian, S. Qian, and V. C. Li,"Dynamic Life Cycle Modeling of Pavement Overlay System: capturing the impacts of users, construction, and roadway deterioration", *The 4th Int'l Conference of the International Society for Industrial Ecology*, ISIE, June 17-20, 2007.

[36] Cable, J. K., Fanous, F. S., Ceylan, H., Wood, D., Frentress, D., Tabbert, T., Oh, S. Y., Gopalakrishnan, K., "Design and Construction Procedure for Concrete Overlay and Widening of Existing Pavements," *FHWA Technical Report* DTFH61-01-X-00042 (Project 6), IHRB Project TR-511, September 2005.

[37] Kim, J., and Buttlar, W. G., "Analysis of Reflective Crack Control System Involving Reinforcing Grid Over Base-Isolating Interlayer Mixture," *Journal of Transportation Engineering*, Vol. 128, No. 4, 2002, pp. 375-384.

[38] ASTM C1018-97 Standard Test Method for Flexural Toughness and First-Crack Strength of Fiber-Reinforced Concrete (Using Beam With Third-Point Loading).

[39] Hutchinson, J. W., and Suo, Z., "Mixed Mode Cracking in Layered Materials," *Advances in Applied Mechanics*, Vol. 29, 1992, pp. 63-191.

[40] Lim, Y. M., Interface Fracture Behavior of Rehabilitated Concrete Infrastructures Using Engineered Cementitious Composites, *Ph.D. Thesis*, The University of Michigan, Ann Arbor, 1996.

[41] Matsumoto, T. P., Suthiwarapirak, P., and Kanda, T., "Mechanisms of Multiple Cracking and Fracture of DFRCCs under Fatigue Flexure," *Proceedings of the JCI International Workshop on Ductile Fiber Reinforced Cementitious Composites (DFRCC) – Application and Evaluation (DFRCC -2002)*, Takayama, Japan, Oct. 2002, pp. 259-268.

[42] Zhang, J., Stang, H., and Li, V. C., "Fatigue Life Prediction of Fiber Reinforced Concrete Under Flexural Load," *International Journal of Fatigue*, Vol. 21, No. 10, 1999, pp. 1033-1049.

CHAPTER 6

Transport Properties of ECC under Chloride Exposure

This chapter addresses the chloride penetration stage in a typical repair deterioration process, before and after cracking occurs at different levels of strain. Chloride diffusion driven by a chloride concentration gradient, which is the predominant mechanism of chloride transport for most of the concrete structures exposed to deicing salts, and airborne or waterborne chloride ions, is the focus of this study. Experiments are conducted under combined mechanical (flexural) and environmental (3% chloride solution ponding) conditions to simulate actual conditions experienced by a structural member when it is subjected to both structural loading and chloride exposure. The influences of material tensile strain capacity, crack width, and applied deformation level on the effective chloride diffusion coefficient are investigated. The results show that ECC is effective at slowing down the diffusion process of chloride ions under combined mechanical and environmental loading, by virtue of its ability to achieve a self-controlled tight crack width, even under large applied straining levels. This study verifies the

concept of improving repaired system durability with the inherent crack self-controlling mechanism of ECC repair materials.

6.1 Steel Corrosion in Concrete Structures

The corrosion of steel in concrete is a major durability problem for reinforced and prestressed concrete structures (Figure 6.1), demanding significant amounts of repair and rehabilitation[1,2,3,4]. When concrete is cast around steel reinforcements, a passivation film will form around the steel bars and protect them from corrosion initiation. However, chloride ions, whether airborne or from deicing salt or seawater, are often present, especially in coastal areas and snow regions where deicing salts are used. Corrosion starts when chloride ions pass through the sound or cracked concrete cover, reach the steel, and accumulate beyond a threshold concentration level. At this point the natural protection layer surrounding the steel becomes depassivated, if oxygen and moisture are present in the steel-concrete interface. The oxidation products generate expansive forces within the concrete, eventually causing the concrete cover to spall[5] (Figure 6.2). Moreover, the cross section of the reinforcing bar or prestressing strand is now diminished, leading to a reduction in the load carrying capacity of the concrete member. It is widely recognized that corrosion of reinforcing steel has led to the premature deterioration of many concrete structures in the United States, especially bridges and marine structures, before their design life was exceeded. Although corrosion is not the sole cause of all structural deficiencies, it is a significant contributor and has become a major concern[3,6].

Current approaches to preventing steel reinforcement corrosion in concrete

bridges have had mixed results[4]. These approaches include the use of good construction design and procedures, adequate concrete cover depth, corrosion-inhibiting admixtures, and the adoption of low-permeability concrete. The reason for the limited success is due to the fact that concrete is brittle and tends to crack under a variety of combined mechanical and environmental loading conditions. In fact, it has been observed recently that the new low permeability concrete (high-performance concrete), which is made from partial substitution of Portland cement with silica fume or fly ash, has a more pronounced tendency than conventional concrete to crack[7, 8]. As a result, a faster, gravity-assisted flow of salt-laden water channels through the cracks, rather than a slow diffusion of chloride through uncracked concrete. Corrosion-inhibiting admixtures for concrete are not useful once concrete cracks[9], at which point the reinforcing steel has no further recourse against corrosion. In this situation the use of a barrier system on the reinforcing steel, such as an epoxy coating or other organic coating, becomes more critical in abating corrosion. However, it is likely that there may never be an organic coating that can resist the extreme combination of constant wetting, high temperature, and high humidity that reinforcing steel is exposed to in marine environments, especially in the splash zone in coastal regions[2]. Epoxy-coated steel bars will have to be used in conjunction with sound, crack-free concrete in bridge decks[10], where the concrete is not constantly wet and other exposure conditions are not as severe. The limitations of current approaches to reducing steel corrosion in concrete calls for a new methodology that fundamentally controls the crack width in concrete repairs, therefore preventing penetration of chloride ions through the repair and substrate concrete, and protecting the reinforcement steel from corrosion.

6.2 Proposed Approach – ECC Microcracking Phenomenon

As highlighted previously, ECC is a class of materials that feature high tensile ductility with moderate fiber volume fraction, typically 2% by volume[11]. Of special interest is the capability of ECC to deform to high levels of tensile strain, commonly over 3%, while maintaining self-controlled tight crack widths. These cracks have experimentally been shown to be on the order of 60 μm (0.002 in.). This high tensile ductility and tight crack width is made possible in ECC through the use of steady state crack models that provide quantitative links between micromechanical properties, such as fiber bridging properties and matrix toughness, and composite mechanical behavior, such as steady state cracking stress and maximum crack width. To accommodate large deformations, rather than forming a small number of cracks which widen with increasing load as seen in concrete or tension-softening FRC, ECC forms numerous microcracks which allow the material to undergo pseudo-strain hardening. Once the initial microcracks widen to the typical 60 μm (0.002 in.) at roughly 1% composite straining, additional microcracks form to accommodate further deformation while maintaining this tight crack width in each crack. This phenomenon was shown previously in Figure 1.12.

The microcracking phenomenon observed in ECC materials (e.g. HES-ECC, ECC M45) when subjected to restrained volume change and stress concentration from existing cracks in substrate concrete, has been described in previous chapters. It should be emphasized that crack width in ECC material is a result of matrix-fiber interaction at specific fiber volume fractions and is independent of the steel reinforcement ratio. This inherent maximum crack width can be seen as a material property, similar to compressive strength or elastic modulus, rather than a structural parameter, such as structural

dimensions or the reinforcing ratio in reinforced concrete. The independence of crack width in ECC from structural dimensions and the ratio of cracking-control reinforcement is a unique property different than other cementitious repair materials, which is crucial for achieving robust resistance to chloride penetration in various application situations without relying on cracking-control reinforcements.

Reinforced concrete design codes currently do not specify precise limits on transport properties, such as maximum concrete permeability, or maximum crack width under loading. Permissible crack widths at the tensile face of reinforced concrete structures for service loads under different environmental conditions, according to ACI Committee 224 specifications[12], are given in Table 6.1. The most stringent crack width limit is placed on water-retaining structures, which are allowed maximum crack widths no larger than 100 μm (0.004 in.). For exposure conditions of seawater, seawater spray, wetting, and drying, crack widths smaller than 150 μm (0.006 in.) are permitted. For deicing chemical exposure, a maximum crack width of 180 μm (0.007 in.) is specified. Within the current ACI code[13], a maximum crack width is no longer explicitly specified, although previous versions[14] of the design code suggested 300 μm (0.012 in.) as an upper limit. The AASHTO[15] design code relies on the computation of a "Z" factor, for which maximum crack width limits are set depending on the type of environmental exposure. The limit imposed within the AASHTO code corresponds to a minimum reinforcement spacing that results in a crack width limit of approximately 350 μm (0.014 in.). As discussed previously, at these relatively large crack widths the permeability of concrete material is nearly five orders of magnitude greater than that of uncracked concrete. While these crack width limits are important in reducing the transport of water and

corrosives (e.g. chlorides) into reinforced concrete, they are far larger than that necessary for blocking corrosives from rapidly deteriorating the reinforcing steel, and thus the entire reinforced concrete structure. Furthermore, these crack width limits are difficult to accurately design for or control in real applications with traditional concrete materials. Through the use of ECC material, which exhibits inherently tight crack widths less than 100 μm (0.004 in.) even under large tensile deformations, there exists the possibility of designing durable repairs with consistent resistance to chloride penetration.

6.3 Transport Properties of Cementitious Materials

The transport of chloride through cementitious materials is a complex phenomenon potentially involving three main mechanisms - permeation, diffusion, and absorption[16]. Depending on the conditions, transport of chloride through concrete can be driven by one or a combination of these three mechanisms. The main driving force behind permeation is the presence of a hydraulic pressure gradient. Permeation is an important transport mechanism for underwater concrete structures, such as offshore structures. Absorption, driven by capillary pore suction, is the dominant transport process when dry concrete is exposed to chloride solution. Diffusion is the most commonly studied transport process of chloride ions. When a reasonably moist concrete (sufficient level of pore water exists) is exposed to a chloride solution, a chloride concentration gradient is created between the concrete element surface and the pore solution. Under such conditions, the diffusion process prevails. It is rare for a significant hydraulic head to be maintained on highway structures, parking structures and buildings, and the effect of absorption is typically limited to a dry and shallow concrete cover

region[17,18,19]. Exposure to deicing salts in snowy regions, or the concomitant presence of humid climate conditions and high level of airborne and waterborne chlorides in coastal regions, create an aggressive salt-laden environment for concrete structures. Therefore, researchers tend to agree that in most cases, diffusion is the dominant chloride transport mechanism for most concrete structures[19,20,21,22], and will be the focus of this study.

The development of reliable methods for predicting chloride transport into concrete is important to determining the service life of reinforced concrete structures. A number of studies have been carried out to understand the transport mechanism of chloride ions [23, 24, 25] and numerous service life prediction models have been introduced[25,26,27,28]. In these studies, it was common to investigate the transport properties of concrete in the uncracked state. However, in reality most reinforced concrete structures experience cracking in field conditions. This is especially true for concrete repairs, which are susceptible to cracking due to restrained volume change or reflective cracking[29,30,31,32,33,34,35].

The formation of cracks increases the transport properties of concrete, so that water, oxygen and chloride ions easily penetrate and reach the reinforcing steel, and accelerate the initiation of steel reinforcement corrosion. Crack widths can range from very small internal microcracks that occur upon application of modest amounts of stress, to quite large cracks caused by undesirable interactions with the environment[36]. Wider crack widths have been found to induce corrosion much faster than relatively smaller cracks.

Aldea et al.[37] conducted rapid chloride permeability tests on normal and high strength concrete samples pre-cracked under a feedback-controlled splitting tensile test,

with crack width up to 400 μm (0.016 in.). It was concluded that cracks less than 200 μm (0.008 in.) had no effect on chloride conductivity, while cracks between 200 and 400 μm (0.008 and 0.016 in.) resulted in higher chloride conductivity. Tsukamoto 1990[38], Wang et al. 1997[39], and Feng and Peng 2006[40] found that the permeability of cracked concrete scales with the third power of crack width, and crack widths below 100 μm (0.004 in.) (50 μm (0.002 in.) for gas permeability) tend to behave like sound concrete.

Lepech and Li[41] found that cracked ECC exhibits nearly the same permeability as sound concrete, even when strained in tension to several percent (Figure 6.3). Within this study, both ECC and reinforced mortar specimens were stretched in tension to 1.5% deformation, resulting in a variety of crack widths and number of cracks among the various specimens. The permeability of these cracked materials was then determined under hydraulic head. As seen in Figure 6.3, there is a dramatic rise in permeability with increasing crack width. Further, when normalized by the number of cracks within the specimen, the comparable permeability of cracked ECC with sound concrete becomes more apparent. These results suggest that due to the self-controlled crack widths, replacing concrete with ECC can make significant strides in durability.

Absorption was examined for both cracked and uncracked ECC specimens by Martinola et al.[42]. These studies found that absorption in cracked ECC specimens (1.41 $kg/m^2/h^{0.5}$) was much higher than in uncracked ECC or concrete mortar specimens (0.54 $kg/m^2/h^{0.5}$). This was due to the presence of microcracks within ECC specimens, which promote liquid transport via capillary suction. The addition of an aqueous Silan-Siloxan hydrophobic agent into the mixing water was proposed to repel capillary suction into the thin ECC cracks. This agent was found to reduce the absorption coefficients of cracked

ECC by over 90%. Sahmaran and Li 2009[43] also found that microcracks induced by mechanical loading increases the sorptivity value of ECC when no water repellent admixture is present. However, capillary suction of ECC is not necessarily a concern when compared with normal concrete, even when the ECC is loaded into the microcracked strain-hardening stage. The use of a water-soluble silicone-based water repellent admixture in the production of ECC further reduced the water sorptivity and absorption properties of cracked ECC, to a level significantly lower than that of normal uncracked concrete.

A comparison of diffusion coefficients for cracked and uncracked concrete shows an increase in the diffusion coefficient for cracked concrete by one to two orders of magnitude, with wider cracks resulting in higher values[44]. Chloride diffusion in concrete pre-cracked under three point bending loading was also studied by Gowripalan et. al[45]. In this study, prisms were preloaded, resulting in cracks up to 300 μm (0.012 in.) in width. The experiment showed that the apparent chloride diffusion coefficient is larger in the tensile zone than compression zone. Mangat and Gurusamy[46] studied the influence of cracks on chloride diffusion in steel fiber reinforced concrete. Cracks of widths ranging from 70 to 1080 μm (0.003 to 0.043 in.) were produced on prism specimens and exposed to cycles of splash and tidal zone marine exposure. The authors concluded that crack widths larger than 500 μm (0.020 in.) have a more pronounced influence on chloride intrusion while crack widths less than 200 μm (0.008 in.) appeared to have nearly no effect on chloride intrusion. The influence of crack widths, up to 66 μm (0.003 in.), on chloride diffusivity was also studied by Tognazzi et. al[47]. The experimental results showed that the chloride diffusion coefficient through cracked concrete is proportional to

the crack width.

Diffusion, the transport by an ion concentration gradient, has previously been examined within HPFRCC materials by Miyazato et al.[48]. Diffusion of both chloride ions (Cl^-) and carbon dioxide (CO_2) within cracked and uncracked HPFRCC and mortar specimens was studied. These two chemical species are of particular concern due to their association with depassivation of reinforcing steel, which is a precursor to active steel rebar corrosion. These studies found that in uncracked specimens, chloride ions and carbon dioxide molecules were transported between 1.5 to 3 times faster through an uncracked HPFRCC matrix than through an uncracked concrete matrix. In cracked sections, however, these results were reversed and HPFRCC specimens showed a much lower rate of diffusion, only 20% to 25% of that exhibited by cracked concrete deformed to the same strain level.

The objective of the present research was to investigate the potential improvement of ECC microcracking behavior on the resistance of chloride diffusion, when subjected to combined mechanical and environmental conditions. This was achieved through preloading ECC beam specimens to different deformation levels, and then exposing them to chloride ponding. The chloride ion diffusion resistance of cracked and uncracked reinforced (with steel wire mesh) mortar specimens was measured in a control test series. For ECC or reinforced mortar specimens, the crack number and crack width varied with the applied deformation. The effects of crack number and crack width on the effective diffusion coefficient were determined. The performance of cracked and uncracked ECC and mortar specimens, in terms of chloride penetration profile and depth, and the effective diffusion coefficient as a function of beam deformation level, was compared.

6.4 Experimental Program

6.4.1 Materials and Mixture Proportions

An ordinary version of ECC, ECC M45, is investigated in this study. The mix proportions for ECC M45 mixtures are summarized in Table 6.2. Similar to typical fiber reinforced cement composites (FRC), ECC M45 consists of Type I Portland cement, sand, Class-F fly ash, water, fibers, and a superplasticizer (SP). However, unlike typical FRCs, the component characteristics and proportions within ECC are carefully determined through the use of micromechanical design tools[49] to achieve the desired strain-hardening response. To minimize the mortar matrix fracture toughness and crack tip energy J_{tip}, no large aggregates were used, and the silica sand had average and maximum grain sizes of 110 μm (0.004 in.) and 200 μm (0.008 in.), respectively. The poly-vinyl-alcohol (PVA) fibers were the same type as used in HES-ECC. They were purposely manufactured with a tensile strength, elastic modulus, and maximum elongation to match the micromechanical design criteria for strain-hardening performance. Additionally, the surface of the PVA fiber was coated with a small amount (1.2% by weight) of a proprietary hydrophobic oiling agent to tailor the interfacial properties between fiber and matrix for strain-hardening performance[50]. The mechanical and geometrical properties of the PVA fibers used in this study are shown in Table 6.3.

In addition to ECC, the resistance of cracked and uncracked reinforced (with steel wire mesh) mortar specimens to chloride ion penetration was also measured in a control test series. The mix proportions of the mortar specimens are also shown in Table 6.2. The components of this material are Type I Portland cement, water, and natural river sand. The ultimate tensile strain capacity of ECC and the compressive strength test results of

ECC and mortar mixtures are also listed in Table 6.2. The compressive strength was computed as an average of three standard Ø75×150 mm (Ø3×6 in.) cylinder specimens. To characterize the direct tensile behavior of the ECC mixtures, 152.4×76.2×12.7 mm (6.0 in. × 3.0 in. × 0.5 in.) coupon specimens were used. Direct tensile tests were conducted under displacement control at a loading rate of 0.005 mm/s (0.0002 in./s). The typical tensile stress-strain curves of ECC mixtures are shown in Figure 6.4.

6.4.2 Specimen Preparation and Testing

From each mixture, Ø75×150 mm (Ø3×6 in.) cylinders were prepared for the determination of chloride penetration depth (immersion test), and 355.6 mm x 50.8 mm x 76.2 mm (14 in. x 2 in. x 3 in.) prisms were prepared for the determination of chloride ion profiles and the diffusion coefficient (salt ponding test). All specimens were demolded at the age of 24 hours, and moisture cured in plastic bags at 95±5% RH, 23±2 ^{0}C for 7 days. The specimens were then air cured at 50±5% RH, 23±2 ^{0}C until the age of 28 days for testing.

Immersion Test

At the end of 28 days, all surfaces of the cylindrical specimens except for their bottom sides were sealed with a silicon coating so that chloride penetration could only occur in one direction. Afterwards, they were left in the laboratory for an additional day. At the age of 29 days, the cylinders were stored under continuous exposure to 3% NaCl solution at room temperature, as shown in Figure 6.5 (a). The NaCl solution was replenished every month to maintain uniform concentration. After 30, 60 and 90 day immersion periods, one cylinder was taken out and split open before being sprayed with

0.1-N silver nitrate (AgNO3) solution (Figure 6.5 (b)). In locations where chloride ions penetrated to at least approximately 0.15% by weight of cement[51], silver chloride will precipitate and cause that portion of the sample to turn white, while the silver nitrate in the non-chloride penetrated zone turns brown.

Salt Ponding Test

Chloride ion profiles and the diffusion coefficient of ECC were evaluated in accordance with AASHTO T259-80[52]. In addition to ECC, the same transport properties of mortar specimens were also determined as a control test series. Each mortar prism was reinforced with three levels of steel mesh to achieve cracks of varying widths. At the age of 28 days, the prism surfaces were abraded using a steel brush. After abrasion, the prisms were preloaded using a four point bending test (Figure 6.6) to obtain different crack widths. The ponding test was carried out with the preloaded specimens in the unloaded state (Figure 6.7). A small amount of crack closure occurred upon unloading. For consistency throughout the test program, all crack width measurements were conducted in the unloaded stage. The widths of the cracks were measured on the surface of the specimens by a portable microscope. The average width of the resulting cracks was obtained through measurement of crack widths at five points.

Table 6.4 shows the preloaded beam deformation (BD) value, along with the corresponding average crack widths (CW), depths, and number of cracks for the prism specimens. Two virgin prisms from each mixture were tested without preloading for control purposes. Note that preloading beam deformation of the mortar prisms was limited to 0.83 mm (0.033 in.) due to the large crack width (~ 400 μm [0.016 in.]) and crack depth 70 mm (2.756 in.) generated in these specimens. In the ECC specimens, the

crack width remained at about 50 μm (0.002 in.), even after beam deformation of 2 mm (0.079 in.). Accurate measurement of crack length in the ECC specimens was not feasible because of the tight crack width. As seen from Table 6.4, when the deformation applied to the prism specimens increased, the number of cracks in ECC clearly increased but crack width did not grow beyond 50 μm (0.002 in.). Micromechanically designed ECC changes the cracking behavior from one crack with large width to multiple smaller cracks (Figure 6.8).

After load application, a Plexiglas embankment was built around the immediate perimeter of the prism specimens, such that a chloride solution could be held against the exposed side surfaces of the prism. At 29 days of age, a solution of 3% NaCl by weight was ponded on the cracked surface of the prisms. In order to retard the evaporation of solution, aluminum plates were used to cover the upper surface of the specimens. After 30 days of ponding, the salt solution was removed from the prism surface and samples were taken from each specimen to measure chloride concentration as a function of depth. In the case of uncracked ECC and mortar specimens, a ponding test was also conducted after 90 days of NaCl solution exposure in accordance with AASHTO T259-80.

In the mortar beams, chloride was found to concentrate near the pre-crack and penetrate deeply – to depths of approximately 40-70 mm (1.575-2.756 in.) depending on the crack width and crack depth of the specimen. Mortar samples were taken from the cracked zone for chloride analysis at various depths by using a 15 mm (0.591 in.) diameter rotary drill. In the ECC beams, chloride penetration occurred at multiple locations corresponding to where the multiple cracks were formed during preloading. However, the penetration depth was much shallower – between 0 to 40 mm (0 to 1.575

in.) depending on the level of imposed deformation. Powder samples for chloride analysis of cracked ECC specimens were taken where the multiple cracks were formed during preloading. Total chloride (acid-soluble) content by weight of material at each sampling point was examined according to AASHTO T 260-97[53].

Statistical and curve-fitting software was then used to examine the chloride profiles. Equation 6.1, Crank's solution to Fick's second law[54], was fitted to the data. Regression analysis yielded the values of the effective diffusion coefficient (D_e) and surface chloride concentration (C_s) for each specimen.

$$C_{(x,t)} = C_s\left[1 - erf\left(\frac{x}{2\sqrt{D_e t}}\right)\right] \tag{6.1}$$

where

C(x,t) = chloride concentration at time t at depth x

C_s = surface chloride concentration

D_e = effective chloride diffusion coefficient

t = exposure time

erf( ) = error function

This equation would perfectly describe the diffusion process of chloride if no other transport mechanisms (i.e., absorption and permeation) were present. However, this is not the case in real field conditions. In this experimental study, the coefficient of diffusion, found by regression analysis of chloride profiles using Equation 6.1, is referred to as the effective diffusion coefficient (D_e), and includes the combined transport mechanisms. D_e forms a reasonable basis for comparing the diffusion properties of cracked and uncracked ECC and mortar specimens.

6.5 Experimental Results and Discussion

The results of immersion testing on the cylinders in the 3% NaCl solution for up to 90 days are shown in Figure 6.9. In this test, cylinder specimens were sealed with a silicon coating on all but one side so that chloride ions were allowed to ingress only in one direction. The main transport mechanism in this test was absorption, initially. However, after the specimens became saturated, diffusion became the dominant transport mechanism at later ages. For ECC mixtures with a low water/cementitious material ratio and high volume of fly ash, chloride ion penetration depths were always lower than that of the mortar mixture. The use of fly ash generally resulted in a denser matrix, by reducing the pore sizes and microcracking in the transition zone[55].

Figure 6.10 presents the chloride concentration profiles of uncracked mortar and uncracked ECC from the ponding test. Prism specimens were examined after 30 and 90 days of exposure, and the effective diffusion coefficients (D_e) and coefficients of determination (R^2) were found using regression analysis. The R^2 value represents how well the estimated regression equation fits the data sample, with a value of one signifying perfect agreement. In this figure, it can be seen that there is no significant difference between the chloride concentration profile of the virgin mortar and ECC specimens. The effective diffusion coefficients of the virgin mortar and ECC specimens exposed for 30 days are higher than for those exposed 90 days, likely due to the continuing hydration of cement and fly ash, which is beneficial in reducing pore size and increasing matrix density[46]. In addition, the effective chloride diffusion coefficient of virgin ECC is slightly lower than that of virgin mortar for 30 and 90 days, probably due to the higher amount of cementitious materials, lower water/cementitious materials ratio, and high volume fly ash content, which leads to a denser microstructure in ECC. A lower

effective chloride diffusion coefficient value implies increased service life, according to Figure 6.2, although no service life determination was made in this study to quantify this effect.

The chloride concentration profiles of cracked mortar and cracked ECC at different depths, exposed to NaCl solution for 30 days, are shown in Figure 6.11. The chloride concentration profiles of virgin (BD = 0 mm) ECC and mortar specimens cured in the same environment and of the same age are also included in this figure. As depth from the surface increased, the chloride content in the cracked zone decreased. Figure 6.11 shows that the presence of cracks significantly modifies the chloride transport properties of reinforced mortar. In all cases the chloride concentration increases as the crack width increases, but this trend is especially pronounced in mortar specimens with crack widths greater than 150 μm (0.006 in.). These conclusions are consistent with previous research findings[46]. The multiple-cracking in ECC due to pre-loading alters the chloride transport properties as a function of beam deformation. It was found that chloride ingress increased as the number of cracks in the ECC specimens increased, although the increase was fairly insignificant when compared to mortar specimens at the same deformation levels. Thus, it can be concluded that an ECC specimen with multiple microcracks exhibited greatly increased chloride penetration resistance.

The effective chloride diffusion coefficients of prisms, calculated by using the chloride ion profiles reported above, together with Fick's second law, are summarized in Table 6.5. As expected, this table clearly demonstrates the increase in the effective diffusion coefficient with beam deformation and crack width increase in the mortar specimens. It was also found that the effective diffusion coefficient increased as the number of cracks in ECC specimens increased. Cracks within the ECC specimens

opened to a maximum width of approximately 50 μm (0.002 in.). As designed, the ECC specimens revealed a significantly smaller effective diffusion coefficient compared to mortar specimens preloaded to the same deformation level, again reflecting the reduction in chloride ion transport rate as a result of tight crack width control in ECC.

Figure 6.12 shows the relationship between the effective diffusion coefficient of chloride ions and crack width in mortar specimens exposed to NaCl solution for 30 days. Salt solution may fill the cracks, which can lead to diffusion from the crack plane[45]. This is evident from the high chloride concentrations measured along the depth of crack. The effective diffusion coefficient generally increased as crack width increased, and became almost constant when the crack width fell below 150 μm (0.006 in.). It appears that the effective diffusion coefficient of mortar has the form of a power function with respect to crack width. The relationship between crack width and chloride diffusivity has also been examined by other researchers. Despite the numerous tests and experimental methods used, a consensus on the relationship between crack width and coefficient of diffusion has not been reached. Some authors have found an increase in diffusivity within cracked concrete up to ten times higher than in uncracked concrete[44,47]. Others have found no effect or even a decrease in the diffusion coefficient[56]. The previous studies measured chloride ingress into cracked concrete with roughly constant crack width, but cracks generated in beams under a bending load will vary in width along the length of the beam. The variety of experimental methods used to create these cracks, measure chloride transport properties, and measure the chloride content, as well as the reactivity of the chemical elements within the solid body, are the main reasons for the diversity of results obtained from these different studies[57].

In the case of mortar beams reinforced with three layers of steel mesh, pitting

corrosion was also observed in the first steel mesh layer of specimens, having crack widths of 400 μm (0.016 in.) after 30 days of NaCl solution exposure. Cracks can reduce the service life of reinforced concrete structures by accelerating the initiation of corrosion, especially when the crack width is larger than 150 μm (0.006 in.), which significantly increases the effective diffusion coefficient.

The crack width in the ECC mix did not grow beyond 50 μm (0.002 in.), even under high levels of beam deformation and 1% tensile straining. However, the number of cracks on the tensile surface did increase. For this reason, the effective diffusion coefficient of ECC specimens at different deflection levels, exposed to NaCl solution for 30 days, are plotted against the number of cracks in Figure 6.13. Corresponding values for virgin ECC specimens, also cured in the same environment for 30 days, are included in the figure. The effective diffusion coefficient of ECC increases linearly with the increase in crack number. This finding agrees with Konin et al., who studied chloride penetration of reinforced ordinary and high strength concrete in the microcracked state[58].

Figure 6.14 shows the relationship between the effective diffusion coefficient of chloride ions and beam deformation level for mortar and ECC specimens. Despite imposition of more than twice the preload deformation, and a higher crack density, the ECC specimens have an effective diffusion coefficient considerably lower than that of the reinforced mortar because of tight crack width control. At higher deformation levels, the effective diffusion coefficient of mortar increased exponentially with beam deformation. The effective diffusion coefficient of ECC, however, increased linearly with the imposed deformation value, because the number of microcracks on the tensile surface of ECC is proportional to the imposed beam deformation. The total chloride concentration profiles, perpendicular to the crack path, indicate no significant chloride penetration in the ECC

specimens, even at large imposed deformation (2 mm [0.079 in.]).

The relatively low diffusion coefficient of cracked ECC specimens can be explained by the combined effects of the self-controlled tight crack width as well as self-healing of the microcracks. The self-healing of cracks becomes prominent when the crack width is small. Based on experimental results, Evardsen[59] and Reinhardt and Jooss[60] proposed that crack widths below 0.1 mm (0.004 in.) can be closed by a self-healing process. In the case of precracked ECC specimens exposed to salt solution, a distinct white deposit was visible over the crack surface after one month of exposure (Figure 6.15). These deposits were most probably caused by efflorescence due to leaching of calcium hydroxide (CH) into cracks[36] and also to the presence of NaCl ions in the solution. The white deposits at the crack surfaces effectively blocked the flow path due to the smaller crack widths present in ECC. An environmental scanning electron microscope (ESEM) observation of the fractured surface of ECC across a healed crack is shown in Figure 6.16. This ESEM observation shows that most of the products seen in the cracks were newly formed C-S-H gels. Calcium hydroxide (CH) and deposited salts were also observed in the crack path. These results indicate that microcracks of ECC exposed to NaCl solution for 30 days healed completely by the end of the exposure period. This can be attributed primarily to the large fly ash content and relatively low water-to-binder ratio in the ECC mixture. The continued pozzolanic activity of fly ash caused self-healing of the crack, which in turn reduced the ingress of the chloride ions. The cracking and healing phenomenon of ECC under combined chloride environment and mechanical loading will be investigated in the next chapter (Chapter 7).

6.6 Conclusions

Significant improvements in resistance to chloride penetration can be achieved through the built-in microcracking mechanism of ECC materials. When subjected to increasing deformation levels, which were achieved through the four-point bending test in this study, ECC exhibited multiple microcracking behavior with increased crack numbers but self-controlled crack width under 50 μm (0.002 in.). This phenomenon is fundamentally different from traditional concrete repair materials, in which localized cracks form and the crack width enlarges with increasing strain level. Reinforcements can limit the width of such localized cracks to some degree, but will not alter the dependency of crack width on strain level and structural dimensions. This was partially illustrated in this study through testing on reinforced mortar specimens, which represents a large category of repair materials. After ECC beams and reinforced mortar beams were preloaded to various deformation levels, and then exposed to 3% NaCl ponding for 90 days, the effective diffusion coefficient of ECC was measured to be significantly lower than that of reinforced mortar. Even at a twice-higher preloaded deformation level, the effective diffusion coefficient of the investigated ECC beam was around ¼ that of the investigated reinforced mortar beam.

The significantly lower effective diffusion coefficient of ECC compared with reinforced mortar is attributed to the difference in cracking pattern. The effective diffusion coefficient of ECC was found to be linearly proportional to the number of cracks, whereas the effective diffusion coefficient of reinforced mortar was proportional to the square of the crack width. Therefore, crack width in mortar had a more pronounced effect on chloride transport than did the number of cracks in ECC, leading to

a much higher effective diffusion coefficient at the same deformation level.

Additionally, through the formation of small microcracks less than 100 μm (0.004 in.), a significant amount of self-healing was observed within the microcracked ECC when subjected to NaCl solution. This self-healing phenomenon aides in further reducing the effective diffusion coefficient of microcracked ECC.

In the uncracked beam specimens, the effective chloride diffusion coefficient of ECC was lower than that of reinforced mortar for 30 and 90 days. This is explained by the denser microstructure of ECC due to a higher amount of cementitious materials, lower water/cementitious materials ratio, and high volume fly ash content. The immersion test results further proved this by showing that the chloride penetration depth in uncracked ECC was 2.0 mm (0.79 in.), 3.3 mm (0.13 in.) and 4.1 mm (0.16 in.) shallower than that of reinforced mortar after 30-day, 60-day and 90-day immersion periods, respectively.

This study validated the concept that the microcracking mechanism and self-controlled crack width in ECC materials are crucial for slowing the transport of chloride ions under combined mechanical loading and chloride exposure, and providing protection for steel reinforcements against corrosion. The advantage of ECC is expected to be greater for large field-scale applications, where repair dimensions and the reinforcing ratio can both affect crack width in traditional repair materials. Findings from this study can be used for service life prediction and life cycle cost analysis of ECC repairs or structures, as well as providing a rational basis for the durable design of ECC infrastructure systems. The research is particularly relevant given the anticipation that ECC, especially when applied as a repair material, will be used in the microcracked state

during its structural service life.

Table 6.1 – Permissible crack widths for reinforced concrete under service loads according to ACI Committee 224.

Exposure condition	Permissible Crack Width	
	in.	mm
Dry air or protective membrane	0.016	0.41
Humidity, moist air, soil	0.012	0.30
Deicing chemicals	0.007	0.18
Seawater and seawater spray, wetting and drying	0.006	0.15
Water-retaining structures	0.004	0.10

Table 6.2 – Mixture proportions and properties of ECC and mortar.

Properties	Mortar	ECC (M45)
FA/C	-	1.2
W/CM[#]	0.35	0.27
Water (W), kg/m^3 (lb/yd^3)	215 (362)	331 (558)
Cement (C), kg/m^3 (lb/yd^3)	614 (1035)	570 (961)
Fly ash (FA), kg/m^3 (lb/yd^3)	-	684 (1153)
Sand (S), kg/m^3 (lb/yd^3)	1535 (2585)	455 (767)
Fiber (PVA), kg/m^3 (lb/yd^3)	-	26 (44)
Superplasticizer (SP), kg/m^3 (lb/yd^3)	-	5.1 (8.6)
7-day compressive strength, MPa (ksi)	36.6 (5.3)	37.8 (5.5)
28-day compressive strength, MPa (ksi)	42.9 (6.2)	53.3 (7.7)
7-day tensile strain capacity (%)	-	3.90
28-day tensile strain capacity (%)	-	3.10

[#]CM: Cementitious Materials (Cement + Fly ash)

Table 6.3 – Mechanical properties of PVA fiber.

Nominal Strength	Apparent Strength	Diameter	Length	Young's Modulus	Elongation
MPa (ksi)	MPa (ksi)	μm (in.)	mm (in.)	GPa (ksi)	(%)
1620 (235)	1092 (158)	39 (0.002)	8 (0.3)	42.8 (6200)	6.0

Table 6.4 – Crack widths, numbers and depths of preloaded ECC and mortar prisms.

Mix ID	Beam Deformation mm (in.)	Average Crack Widths μm (in.)	Crack Depth mm (in.)	Crack Number
Mortar	0.50 (0.020)	~50 (0.002)	20 (0.787)	1
	0.70 (0.028)	~150 (0.006)	36 (1.417)	1
	0.80 (0.031)	~300 (0.012)	55 (2.165)	1
	0.83 (0.033)	~400 (0.016)	70 (2.756)	1
ECC (M45)	0.5 (0.020)	~0	-	0
	1.0 (0.039)	~50 (0.002)	-	15
	1.5 (0.059)	~50 (0.002)	-	21
	2.0 (0.079)	~50 (0.002)	-	35

Table 6.5 – Chloride ponding test: effective diffusion coefficient.

Mix ID	Beam Deformation mm (in.)	Average Crack Widths μm (in.)	Diffusion Coefficient $m^2/s \times 10^{-12}$ ($in.^2/s \times 10^{-8}$)
Mortar	0.00	-	10.58 (1.64)
	0.50 (0.020)	~50 (0.002)	33.28 (5.16)
	0.70 (0.028)	~150 (0.006)	35.54 (5.51)
	0.80 (0.031)	~300 (0.012)	126.53 (19.61)
	0.83 (0.033)	~400 (0.016)	205.76 (31.89)
ECC (M45)	0.00	-	6.75 (1.05)
	0.5 (0.020)	~0	8.10 (1.26)
	1.0 (0.039)	~50 (0.002)	27.99 (4.34)
	1.5 (0.059)	~50 (0.002)	37.50 (5.81)

Figure 6.1 – Corrosion in Concrete Structures.

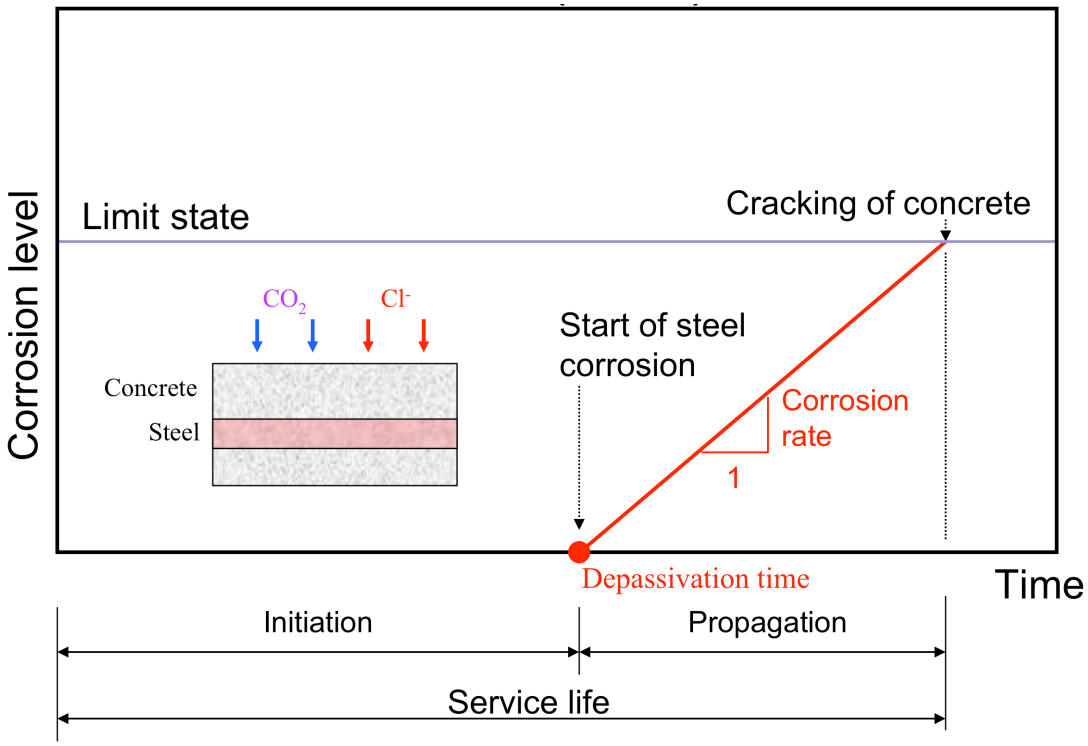

Figure 6.2 – Corrosion process of reinforcing steel according to Tuutti (1982)[20].

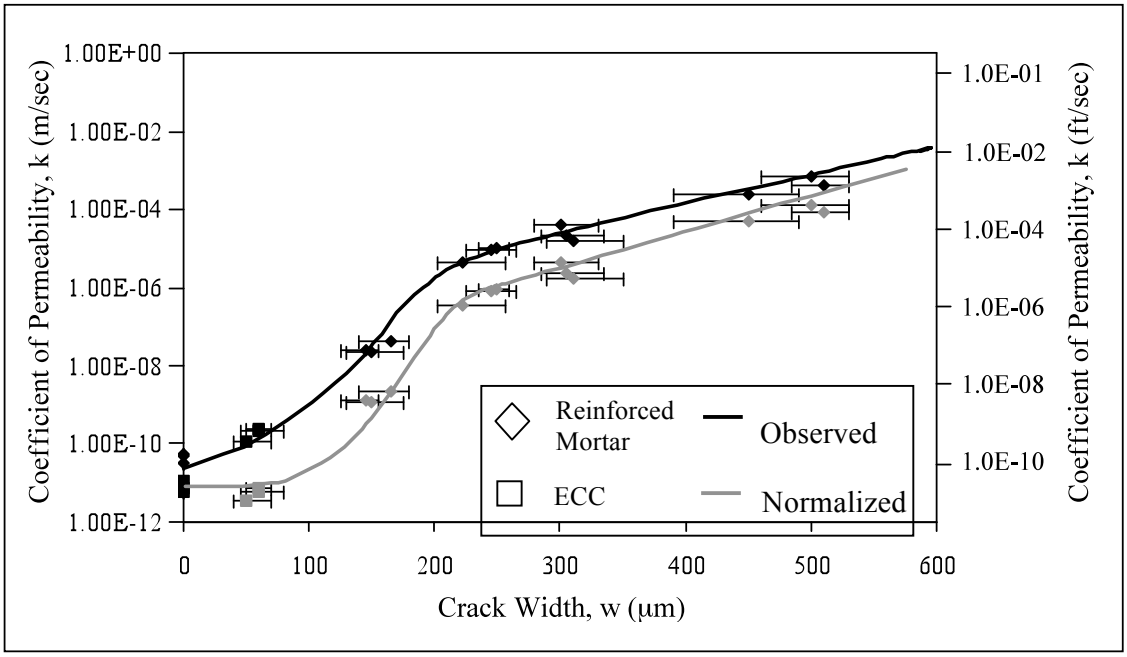

Figure 6.3 – Coefficient of permeability versus crack width for ECC and reinforced mortar series deformed to 1.5% in uniaxial tension[41].

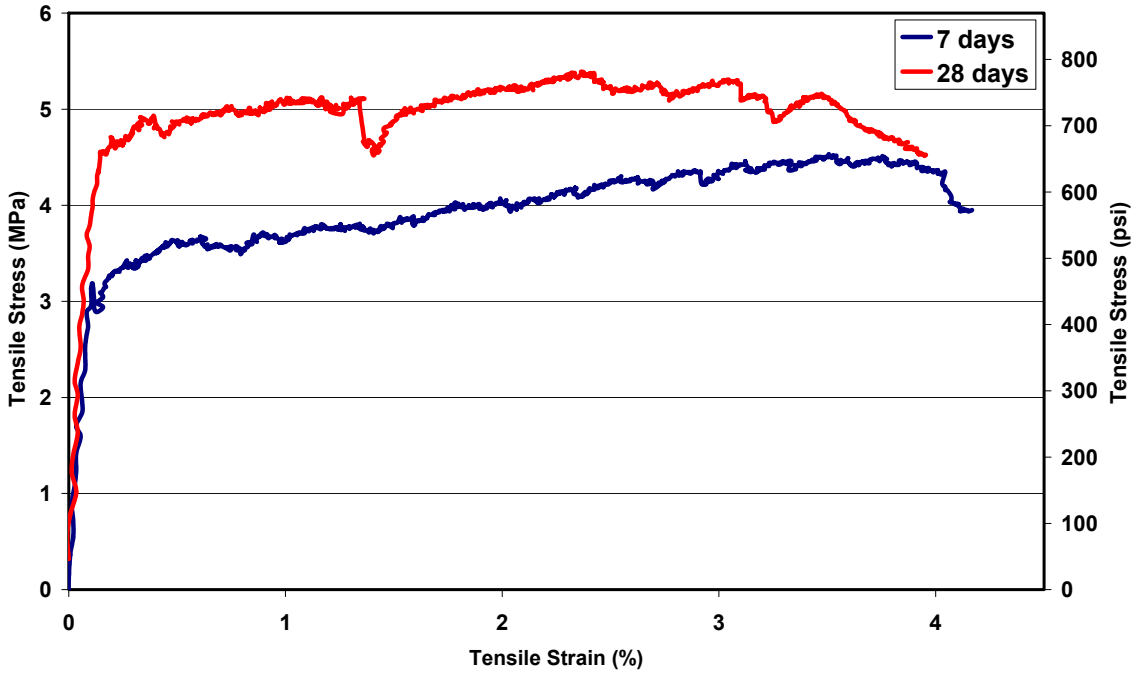

Figure 6.4 – Typical tensile stress-strain response of ECC mixture.

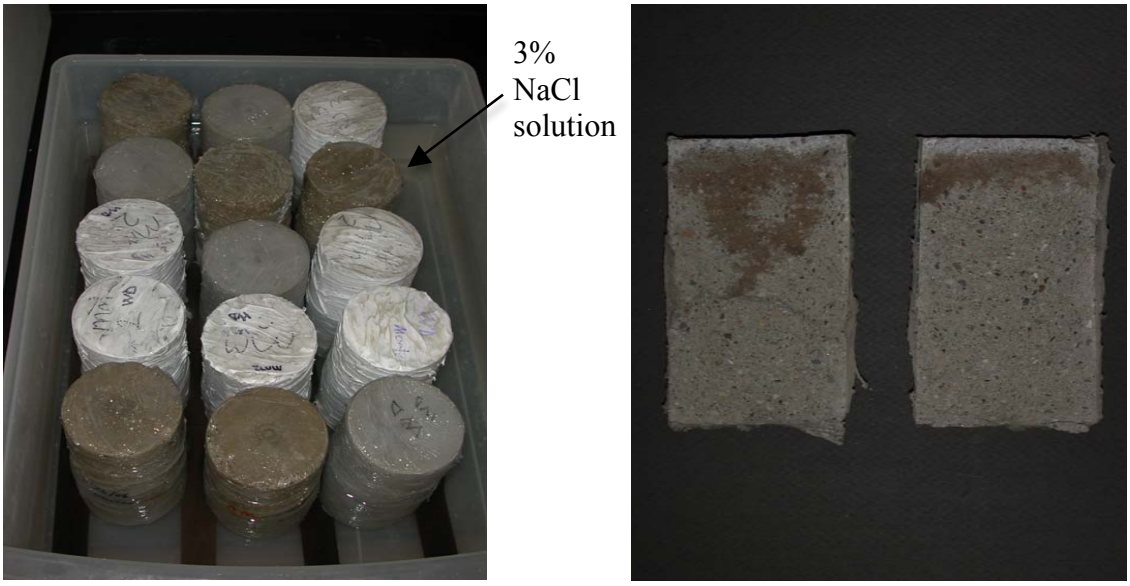

Figure 6.5 – Immersion test. (a) Cylinders were stored under continuous exposure to 3% NaCl solution. (b) One cylinder was taken out, split open, and sprayed with 0.1-N silver nitrate (AgNO3) solution, to measure the chloride penetration depth.

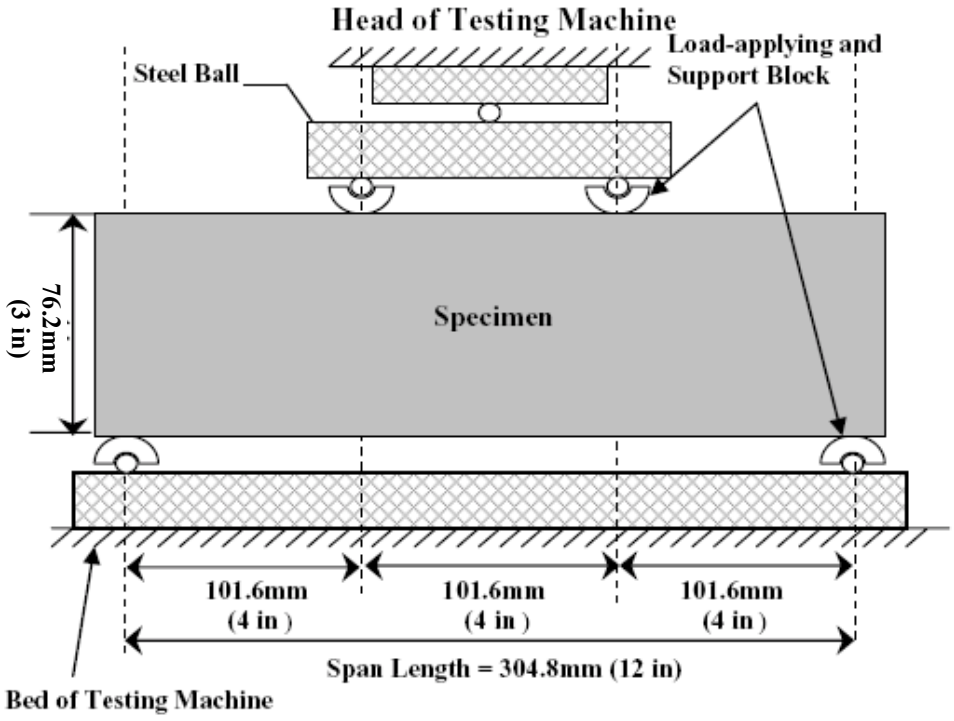

Figure 6.6 – Four point bending test.

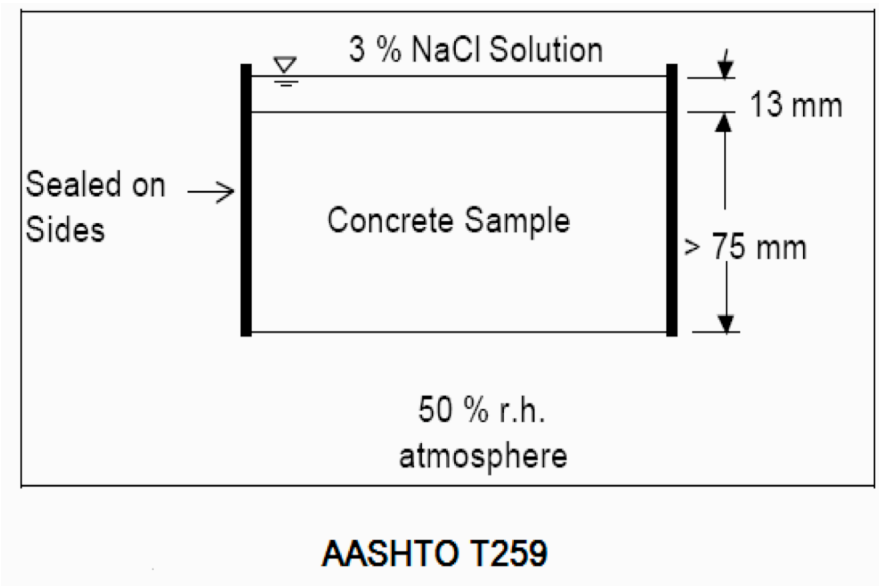

Figure 6.7 – Salt ponding test on uncracked and cracked beam specimens with dimensions of 355.6 mm x 50.8 mm x 76.2 mm (14 in. x 2 in. x 3 in.).

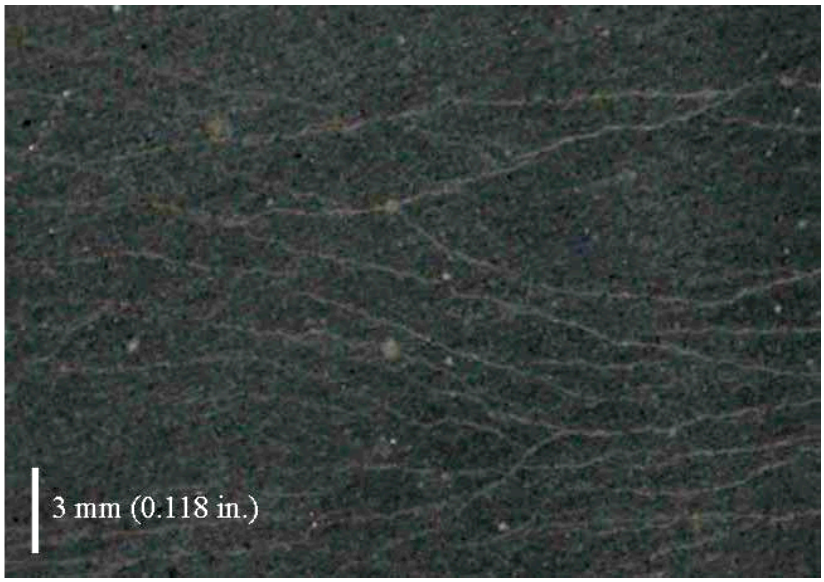

Figure 6.8 – Typical crack pattern on positive moment surface of ECC beams at 2 mm (0.079 in.) deformation.

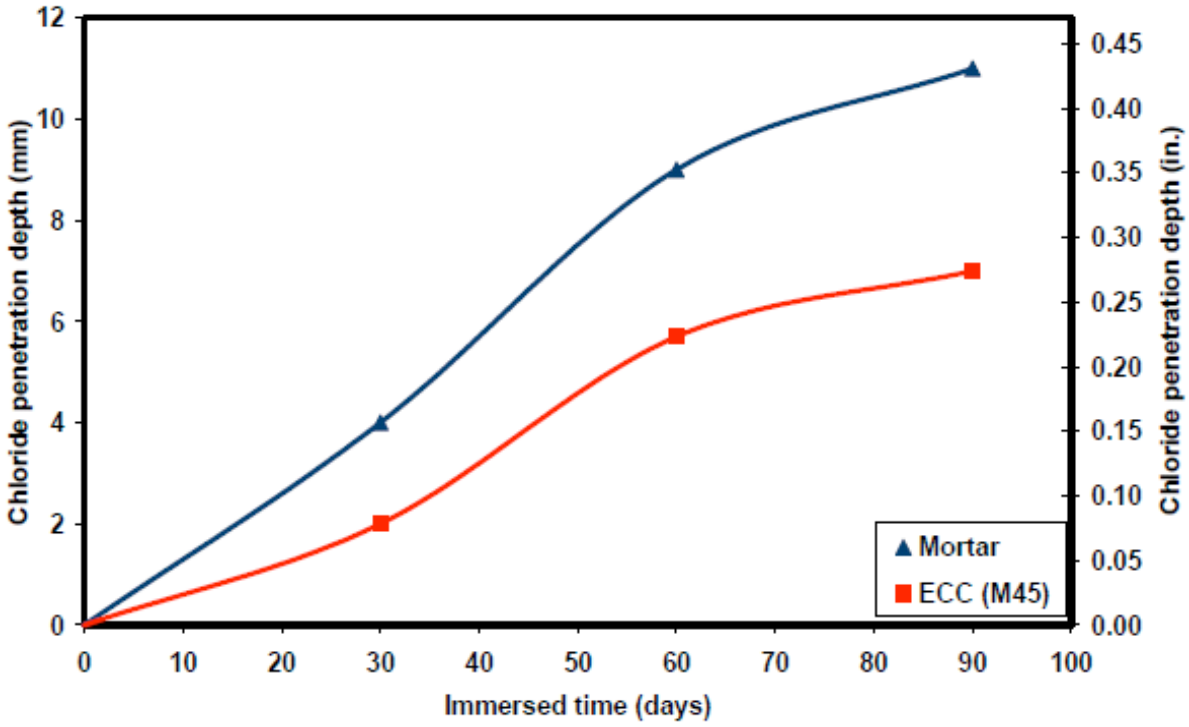

Figure 6.9 – Chloride penetration depth variation measured by immersion test.

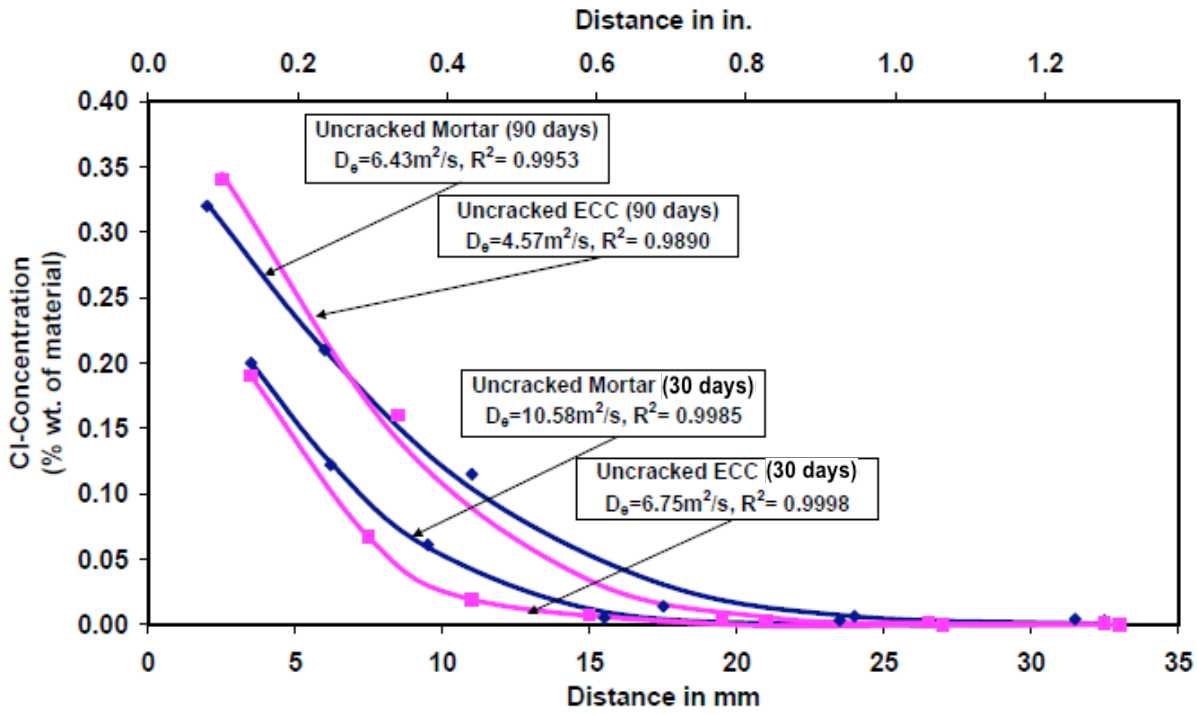

Figure 6.10 – Chloride profiles of uncracked mortar and uncracked ECC prisms after 30 and 90 days in 3% NaCl solution.

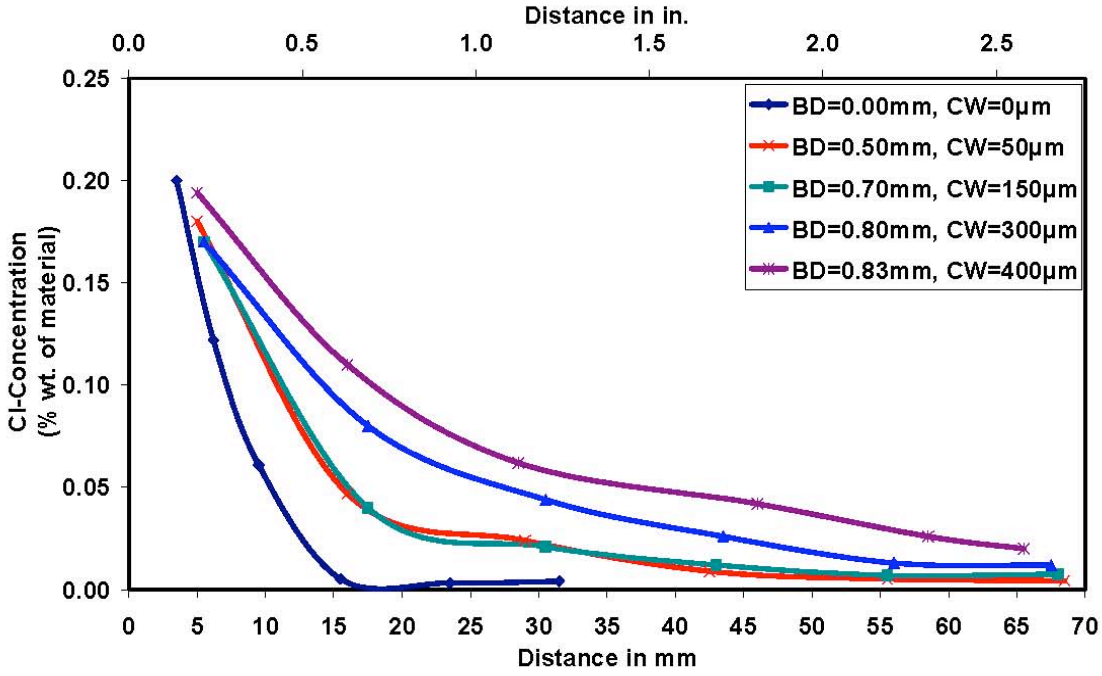

(Mortar)

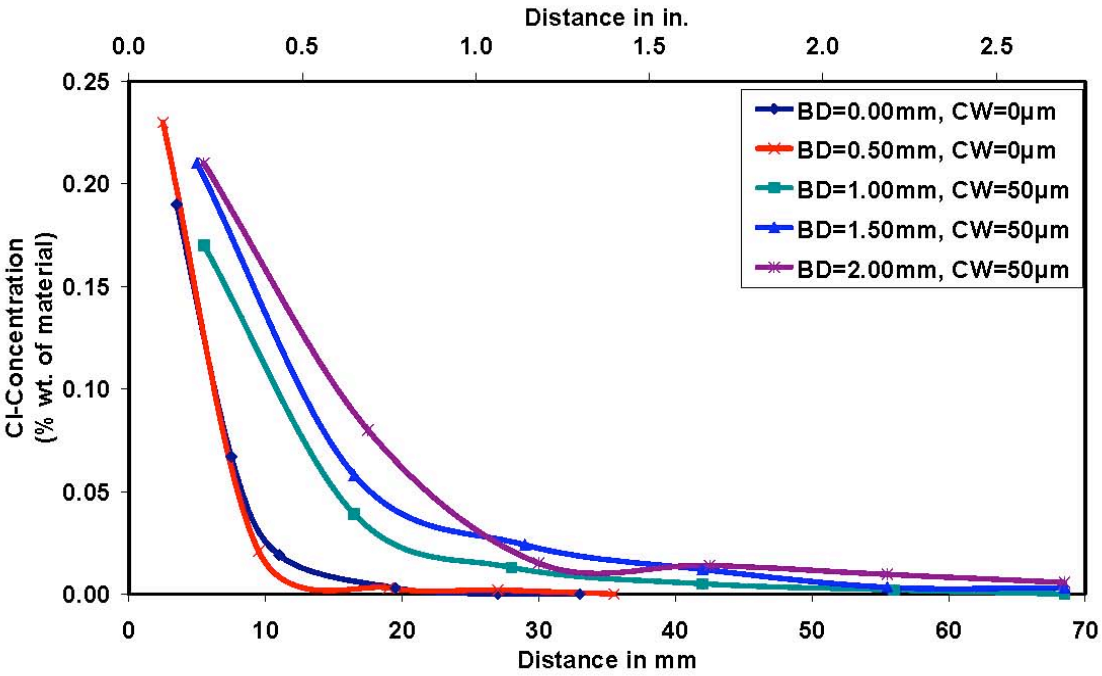

(ECC)

Figure 6.11 – Chloride profiles of mortar and ECC prisms in cracked zone at 30 days exposure.

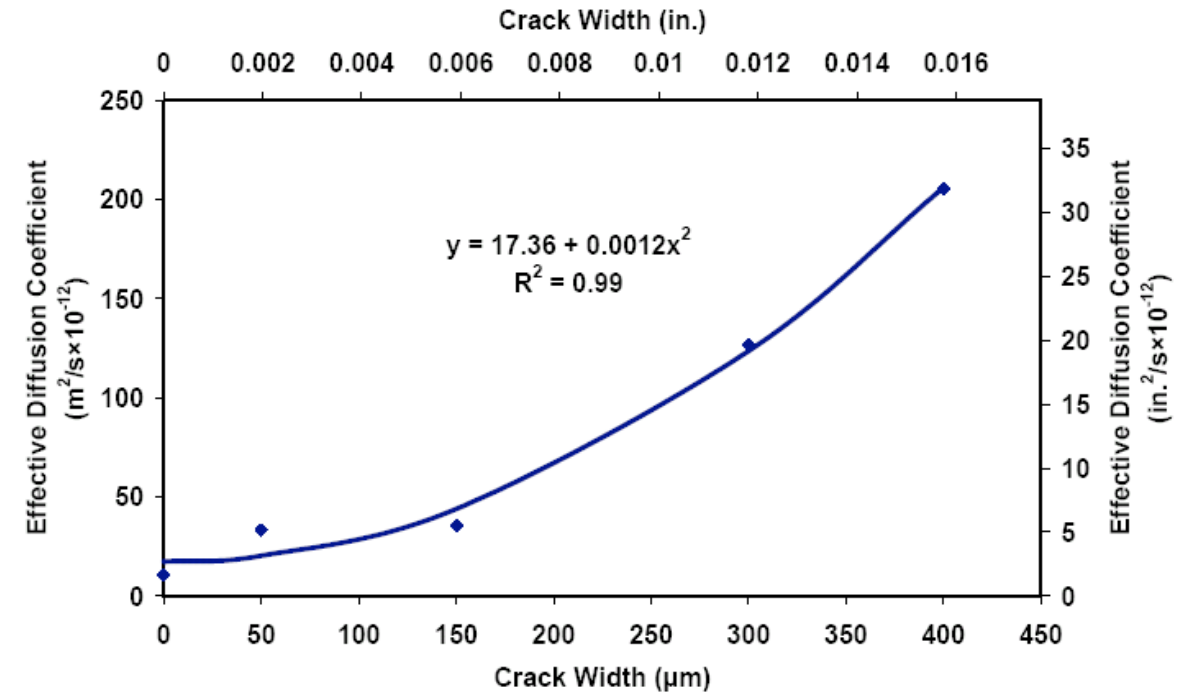

Figure 6.12 – Diffusion coefficient versus crack width for mortar deformed under bending load.

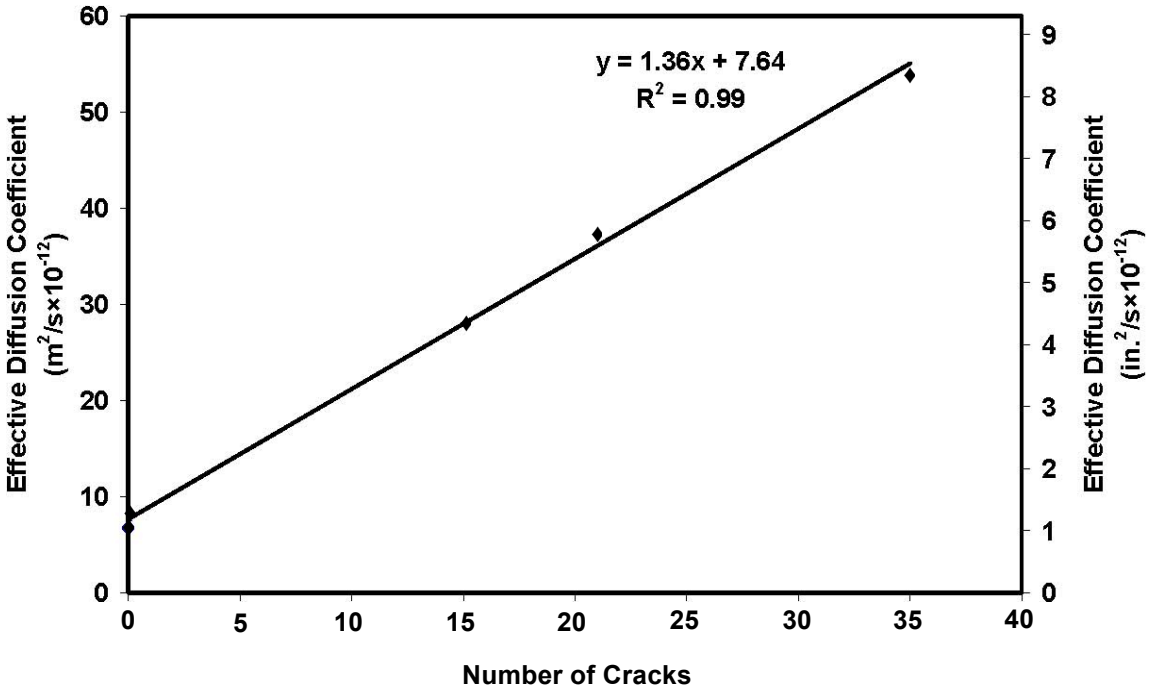

Figure 6.13 – Diffusion coefficient versus number of cracks for ECC.

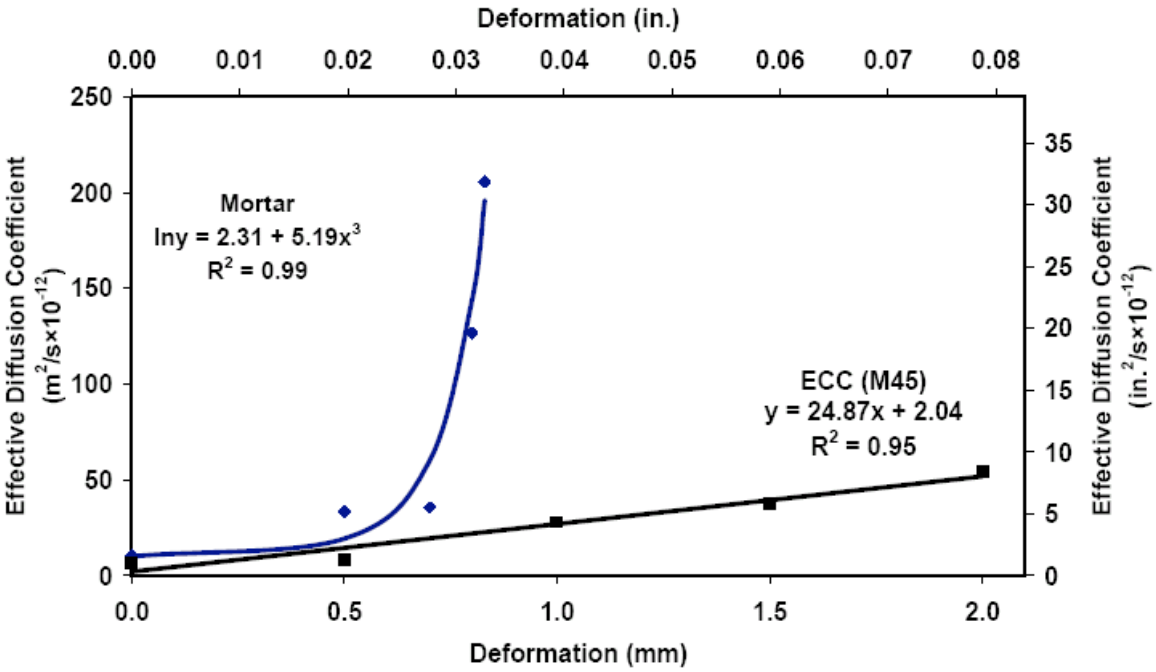

Figure 6.14 – Diffusion coefficient versus preloading deformation level for ECC and mortar.

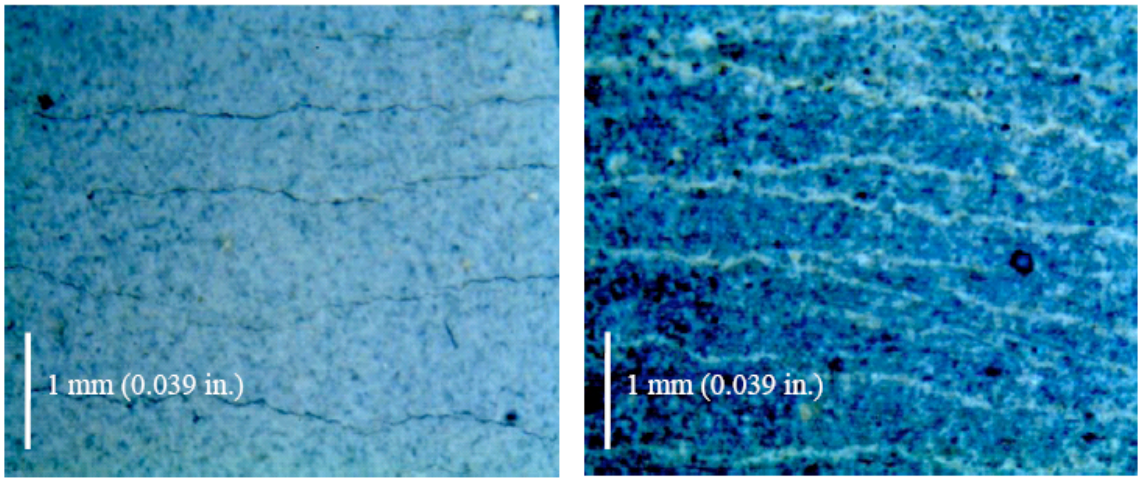

(a) ECC cracks before salt ponding test (b) ECC cracks after salt ponding test

Figure 6.15 – Self-healing products in ECC microcracks before and after salt ponding test at 30 days exposure.

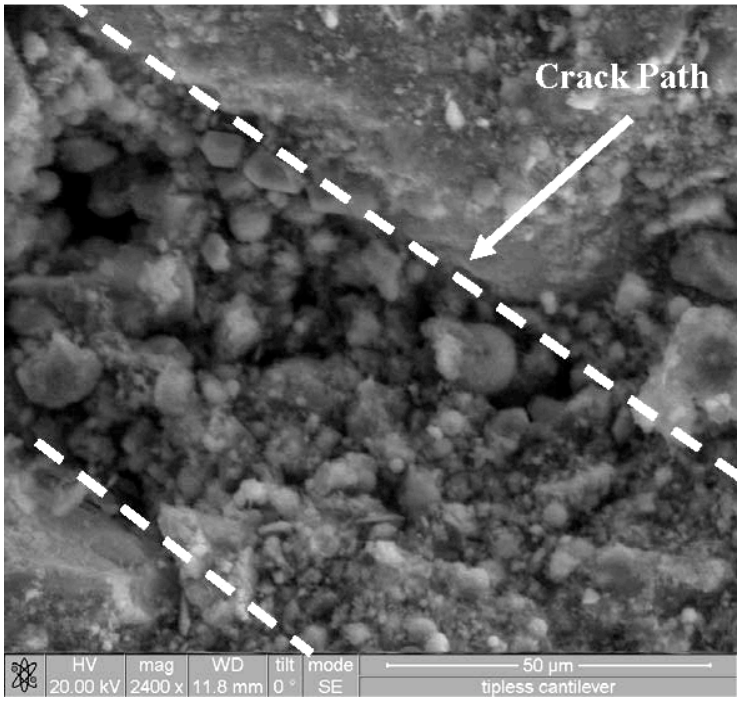

Figure 6.16 – ESEM micrograph of rehydration products in a self-healed crack.

References:

[1] Batis, G., Pantazopoulou, P., and Routoulas, A., "Corrosion Protection Investigation of Reinforcement by Inorganic Coating in the Presence of Alkanolamine-Based Inhibitor," *Cement and Concrete Composites*, Vol. 25, 2003, pp. 371-377.

[2] Elsener, B., "Macrocell Corrosion of Steel in Concrete – Implications for Corrosion Monitoring," *Cement & Concrete Composites*, Vol. 24, 2002, pp. 65-72.

[3] The State of the Nation's Highway Bridges: Highway Bridge Replacement and Rehabilitation Program and National Bridge Inventory, *Thirteenth Report to the United States Congress*, Federal Highway Administration, Washington, D. C., May 1997.

[4] Lewis, D. A., "Some Aspects of the Corrosion of Steel in Concrete," *Proceeding of the First International Congress on Metallic Corrosion*, London, 1962, pp. 547-555.

[5] Scheissl, P. "Corrosion of Steel in Concrete" *RILEM Report*. Chapman and Hall. London. 1988.

[6] Hime, W. G., "The Corrosion of Steel – Random Thoughts and Wishful Thinking," *Concrete International*, Vol. 15, No. 10, 1993, pp. 54-57.

[7] Mehta, P.K., "Durability–Critical Issues for the Future", *Concrete International*, Vol. 19, No. 6, 1997, pp. 27-33.

[8] Xi, Y., Shing, B., Abu-Hejleh, N., Asiz, A., Suwito, A., Xie, Z., and Ababneh, A., "Assessment of the Cracking Problem in Newly Constructed Bridge Decks in Colorado," Colorado Department of Transportation Research Branch. Denver, Colorado. CDOT-DTD-R-2003-3. March 2003.

[9] Kondratova, I., and Bremner, T. W., "Field and Laboratory Performance of Epoxy-Coated Reinforcement in Cracked and Uncracked Concrete," Presented at the 77th Annual Meeting of the Transportation Research Board, Washington, D. C., 1998.

[10] Whiting, D., Nagi, M., and Broomfield, J. P., "Evaluation of Sacrificial Anode for Cathodic Protection of Reinforced Concrete Bridge Decks," *Report No. FHWA-RD-95-041*, Federal Highway Administration, Washington, D. C., May, 1995.

[11] Li, V.C., "On Engineered Cementitious Composites (ECC) – A Review of the Material and its Applications," *Journal of Advanced Concrete Technology*, Vol. 1, No. 3, 2003, pp. 215-230.

[12] ACI Committee 224R-01, "Control of Cracking in Concrete Structures," *ACI Manual of Concrete Practice, Part 3*, American Concrete Institute, Farmington Hills, Michigan, 2001.

[13] American Concrete Institute "Building Code Requirements for Structural Concrete (ACI 318-08) and Commentary (ACI 318R-08)," ACI Committee 318, Detroit, Michigan, 2008.

[14] American Concrete Institute "Building Code Requirements for Structural Concrete (ACI 318-95) and Commentary (ACI 318R-95)," ACI Committee 318, Detroit, Michigan, 1995.

[15] American Association of State Highway and Transportation Officials "AASHTO LFRD Bridge Design Specifications: Second Edition," AASHTO, Washington, D.C., USA, 1998, pp. 5-41.

[16] Uji, K., Matsuoka, Y., and Maruya, T., "Formulation of an Equation for Surface Chloride Content of Concrete due to Permeation of Chloride," *Corrosion of Reinforcement in Concrete*, Society of Chemical Industry, London, 1990, pp. 258-267.

[17] Heirman, G., Vandewalle, L., Boel, V., Audenaert, K., de Schutter, G., D'Hemricourt, J., Desmet, B., and Vantomme, J., "Chloride Penetration and Carbonation in Self-Compacting Concrete," *ConcreteLife'06 - International RILEM-JCI Seminar on Concrete Durability and Service Life Planning: Curing, Crack Control, Performance in Harsh Environments*, RILEM Publications SARL, 2006, pp. 13-23.

[18] Ghanem, H. A., "Chloride Ion Transport in Bridge Deck Concrete under Different Curing Durations," *M.S.E. Thesis in Civil Engineering*, Texas Tech University, 2008, p. 159.

[19] Stanish, K. D., Hooton, R. D., and Thomas, M. D. A., "Testing the Chloride Penetration Resistance of Concrete: A literature Review," *FHWA Contract DTFH61-97-R-00022 "Prediction of Chloride Penetration in Concrete"*, 2000.

[20] Tuutti, K., "Service Life of Structures with regard to Corrosion of Embedded Steel," *Performance of Concrete in Marine Environment, ACI SP-65*, American Concrete Institute, Detroit, pp. 223-236.

[21] Browne, R. D., and Geoghegan, M. P., "Mechanism of Corrosion of Steel in Concrete in Relation to Design, Inspection and Repair of Offshore and Coastal Structures," *Performance of Concrete in Marine Environment*, ACI SP-65, American Concrete Institute, pp. 169-204.

[22] Bruenfield, N., "Chloride in Concrete," *Concrete Repairs*, Paladian, Vol. 2, 1986, pp. 115-130.

[23] Hong, K., and Hooton, R. D., "Effects of Cyclic Chloride Exposure on Penetration of Concrete Cover." *Journal of Cement and Concrete Research*, Vol. 29, No. 9, Sept. 1999, pp. 1379-1386.

[24] Ababneh, A., Benboudjema, F., and Xi, Y., "Chloride Penetration in Nonsaturated Concrete," *Journal of Materials in Civil Engineering*, Vol. 15, No. 2, Mar.-Apr. 2003, pp. 183-191.

[25] Hooton, R.D., and McGrath, P.F., "Issues Related to Recent Developments in Service Life Specifications for Concrete Structures," *Chloride Penetration into Concrete*, International RILEM Workshop, St. Remy - Les Chevreuse, 1995, p. 10.

[26] Clifton, J., "Predicting the Service Life of Concrete," *ACI Materials Journal*, Vol. 90, No. 6, Nov.-Dec. 1993, pp. 611-617.

[27] Liang, M. T., Wang, K. L., and Liang, C. H., ''Service Life Prediction of Reinforced Concrete Structures,'' *Journal of Cement and Concrete Research*, Vol. 29, No. 9, Sept. 1999, pp. 1411-1418.

[28] ACI Committee 365.1R-00, "Service-Life Prediction-State-of-the-Art Report," American Concrete Institute, Farmington Hills, Michigan, 2000.

[29] Li, M. and Li, V. C., "Influence of Material Ductility on the Performance of Concrete Repair", Accepted, *ACI Materials Journal*, Feb. 2009.

[30] Czarnecki, L., Garbacz, A., Lukowski, P., and Clifton, J. R., "Polymer Composites for Repairing Portland Cement Concrete: Compatibility Project," *Technical Report NISTIR 6394*, National Institute of Standards and Technology, 1999.

[31]Emmons, P. H., Vaysburd, A. M., Poston, R. W., and McDonald, J. E., "Performance Criteria for Concrete Repair Materials, Phase II, Field Studies," *Technical Report REMR-CS-60*, U. S. Army Waterways Experiment Station, Vicksburg, MS, September 1998.

[32] Pigeon, M. and Bissonnette, B., "Bonded Concrete Repairs: Tensile Creep and Cracking Potential," *Concrete International*, Vol. 21, No. 11, November 1999, pp. 31-35.

[33] Vayburd, A. M., "Research Needs for Establishing Material Properties to Minimize Cracking in Concrete Repairs, Summary of a Workshop," *ICRI Publication No. Y320001*, 1996.

[34] Vaysburd, A. M., Emmons, P. H., McDonald, J. E., Poston, R. W., and Kesner, K. E., "Performance Criteria for Concrete Repair Materials, Phase II Summary Report," *Technical Report REMR-CS-62*, U. S. Army Engineers Waterways Experiment Station, Vicksburg, MS, March 1999.

[35] Li, V. C., Li, M., and Lepech, M., "High Performance Material for Rapid Durable Repair of Bridges and Structures" *MDOT Report RC-1484*, Dec. 2006.

[36] Mindess, S., and Young, F., *Concrete*, Prentice Hall Inc., Englewood Cliffs, New Jersey, 1981.

[37] Aldea, C. M., Shah, S. P., and Karr, A., "Effect of Cracking on Water and Chloride Permeability of Concrete," *Journal of Materials in Civil Engineering*, Vol. 11, No. 3, Aug. 1999, pp. 181-187.

[38] Tsukamoto, M., "Tightness of Fiber Concrete," *Darmstadt Concrete*, 5, 1990, pp. 215-225.

[39] 21. Wang, K., Jansen, D, Shah, S., Karr, A., "Permeability Study of Cracked Concrete," *Cement and Concrete Research*, Vol. 27, No. 3, 1997, pp. 381-393.

[40] Feng, N.Q., and Peng, G. F., "Effect of Mineral Admixtures on Durability of Concrete Structure Subjected to Alkaline Saline Corrosions," *Key Engineering Materials*, Vol. 302-303, 2006, pp. 68-72.

[41] Lepech, M. D., and Li, V. C., "Water Permeability of Engineered Cementitious Composites," *Cement and Concrete Composites*, Accepted July 23 2009.

[42] Martinola, G., Baeuml, M. F., and Wittmann, F. H., "Modified ECC by Means of Internal Impregnation," *Journal of Advanced Concrete Technology*, Vol. 2, No. 2, 2004, pp. 207-212.

[43] Sahmaran, M., and Li, V. C., "Influence of Microcracking on water absorption and sorptivity of ECC," *RILEM J. of Materials and Structures*, Vol. 42, 2009, pp. 593-603.

[44] Raharinaivo, A., Brevet, P., Grimaldi, G., and Pannier, G., "Relationship between Concrete Deterioration and Reinforcing-Steel Corrosion," *Durability of Building Materials*, Vol. 4, 1986, pp. 97-112.

[45] Gowripalan, N., Sirivivatnanon, V., and Lim, C. C., "Chloride Diffusivity of Concrete Cracked in Flexure," *Journal of Cement and Concrete Research*, Vol. 30, No. 5, May 2000, pp. 725–730.

[46] Mangat, P. S., and Gurusamy, K., "Chloride Diffusion in Steel Fibre Reinforced Marine Concrete," *Journal of Cement and Concrete Research*, Vol. 17, No. 3, May 1987, pp. 385–396.

[47] Tognazzi, C., Ollivier, J.-P., Carcasses, M., and Torrenti, J.-M., "Couplage Fissuration-De´gradation Chimique des Mate´riaux Cimentaires: Premiers Re´sultats sur les Proprie´te´s de Transfert," *Ouvrages, ge´omate ´riaux et interactions*, Ch. Petit, G. Pijaudier-Cabot, and J. M. Reynouard, eds., Herme`s, Paris, 1998, pp. 69–84.

[48] Miyazato, S. and Hiraishi, Y. "Transport Properties and Steel Corrosion in Ductile Fiber Reinforced Cement Composites," *Proceedings of the Eleventh International Conference on Fracture,* Turin, Italy, March 20-25, 2005.

[49] Li, V. C., Wang, S, and Wu, C., "Tensile Strain-Hardening Behavior of Polyvinyl Alcohol Engineered Cementitious Composite (PVA-ECC)," *ACI Materials Journal*, Vol. 98, No. 6, 2001, pp. 483-492.

[50] Li, V. C., Wu, C., Wang, S., Ogawa, A., and Saito, T., "Interface Tailoring for Strain-hardening PVA-ECC," *ACI Materials Journal*, Vol. 99, No. 5, Sept.-Oct. 2002, pp. 463-472.

[51] Otsuki, N., Nagataki, S., Nakashita, K., "Evaluation of AgNO3 Solution Spray Method for Measurement of Chloride Penetration into Hardened Cementitious Matrix Materials," *Construction and Building Material*, Vol. 7, No. 4, 1993, pp. 195–201.

[52] Standard Method of Test for Resistance of Concrete to Chloride Ion Penetration, AASHTO T 259-80, AASHTO, USA, 2001.

[53] Standard Method of Test for Sampling and Testing for Chloride Ion in Concrete and Concrete Raw Materials, AASHTO T 260-97, AASHTO, USA, 2001.

[54] Crank, J., *The Mathematics of Diffusion (2nd Edition),* Oxford University Press, London, 1975.

[55] Mehta, P. K., and Monteiro, P. J. M., *Concrete – Microstructure, Properties, and Materials (Indian Edition)*, Indian Concrete Institute, Chennai, 1997.

[56] Rodriguez, O.G., and Hooton, R.D., "Influence of Cracks on Chloride Ingress into Concrete," *ACI Materials Journal*, Vol. 100, No. 2, Mar.-Apr. 2003, pp. 120-126.

[57] Gerard, B., Reinhardt, H.W., and Breysse, D., "Measured Transport in Cracked Concrete*," Penetration and Permeability of Concrete*, H. W. Reinhardt, ed., RILEM Report 16, 1997, pp. 123-153.

[58] Konin, A., Francois, R., and Arliguie, G., "Penetration of Chlorides in Relation to the Microcracking State into Reinforced Ordinary and High Strength Concrete," *Materials and Structures*, Vol. 31, No. 209, June 1998, pp. 310-316.

[59] Evardsen, C. "Water Permeability and Autogenous Healing of Cracks in Concrete," *ACI Materials Journal*, Vol. 96, No. 4, Jul.-Aug. 1999, pp. 448-454.

[60] Reinhardt, H. W., and Jooss, M., "Permeability and Self-Healing of Cracked Concrete as a Function of Temperature and Crack Width," *Journal of Cement and Concrete Research*, Vol. 33, No. 7, Mar. 2003, pp. 981–985.

CHAPTER 7

Effect of Cracking and Healing on the Durability of ECC under Combined Aggressive Chloride Environment and Mechanical Loading

ECC's large tensile ductility and self-controlled crack width below 100 μm are essential for achieving durable repair performance. This chapter investigated the durability of ECC in terms of maintaining these tensile properties under combined mechanical loading conditions and aggressive chloride environment. Specifically, ECC specimens were preloaded to 0.5, 1.0, and 1.5% tensile strain levels, and then immersed in 3% chloride solution for 30 days, 60 days, and 90 days, respectively. These specimens, together with control virgin (without preloading) specimens, were reloaded to evaluate the potential change in tensile properties including tensile strength, material stiffness, and tensile strain capacity. This study revealed that the reloaded specimens retained multiple microcracking behavior and tensile strain capacity of more than 3%, while the average crack width increased from 40μm to 100μm and tensile strength was reduced by 10%. Furthermore, self-healing of the existing microcracks in ECC under chloride exposure is

evident in terms of recovery of initial material stiffness and tensile strain capacity. These results indicated that even under severe marine environment conditions, ECC remains durable and can provide reliable tensile ductility and self-controlled crack width to prevent common cracking failure as well as chloride penetration.

7.1 Introduction

Concrete cracking is a result of the combined effects of mechanical loading conditions and environmental exposure[1]. Cracking can occur at different stages throughout the life of a concrete structure. The presence of cracks not only causes loss of load carrying capacity and stiffness of structural members, but also dramatically lowers the resistance to penetration by aggressive agents that results in further deterioration.

Among all possible forms of environmental exposure for concrete structures, an aggressive chloride environment (e.g. marine environment) is one of the most severe and aggressive on earth[2]. Serious concrete deterioration has been reported[3,4,5,6], and the general cause was noted to be concrete cracking, which resulted in corrosion of embedded reinforcing steel[2]. Maximum allowable crack widths are thereby required in various codes and specifications by technical committees for design of reinforced concrete structures exposed to marine environments. These requirements are summarized in **Figure 7.1**[7,8,9,10,11,12]. The allowable maximum crack width ranges from 150 μm to 300 μm, with the most stringent requirements specified by JSCE and ACI 224. Such crack limits, however, are a challenge for structures or repairs using traditional concrete materials when they are subjected to mechanical loading conditions while also being attacked in aggressive environments. Despite extensive research, reliable crack

width control using steel reinforcements in concrete structures remains difficult to realize in practice[13,14,15,16].

In previous chapters of this dissertation, it has been proposed and demonstrated that the inherent large tensile ductility (>3%) of ECC achieved through multiple microcracking behavior, as well as its self-controlled crack width under 100 μm during strain-hardening stage, are critical properties for achieving durability of concrete repairs. Durability improvements include preventing cracking and interfacial delamination caused by restrained volume change (Chapter 4), eliminating reflective cracking under stress concentration and fatigue (Chapter 5), and enhancing resistance to chloride penetration, even at large deformation levels (Chapter 6). Through suppression of these three most common mechanisms during the typical deterioration process in concrete structures, the ECC repair can effectively protect the underlying concrete from the hostile environment, and restore/enhance its load carrying capacity. By these means, the structural service life can be greatly extended with minimized future maintenance and repair frequencies.

While ECC's large tensile ductility and self-controlled tight crack width are essential for ensuring repair durability, a question that could naturally be raised is whether ECC can still maintain these properties under combined aggressive environmental (e.g. chloride) exposure and mechanical loading. This concern is critical, especially because for most repair applications ECC is expected to be in service during its strain-hardening stage, as discussed in Chapters 4, 5, and 6. At this stage, the imposed deformation due to restrained shrinkage, movement of underlying cracks, and structural load would have activated multiple microcracking behavior with a certain amount of microcracks. When exposed to an aggressive chloride environment, the presence or

potential penetration of chloride ions through these cracks might reach the fibers and the fiber/matrix interface, leading to potential loss of mechanical properties of ECC. The objective of the present study is to understand the long-term durability of ECC in both the cracked and uncracked state, i.e. the influence of different strain levels, combined with different time-lengths of chloride exposure, on the tensile ductility and cracking behavior of ECC. Specifically, the tensile ductility and self-controlled steady-stage crack width of ECC are investigated after a specified preloaded deformation level, and after exposure to chloride for a specified time period.

7.2 Evidence of Self-Healing of ECC Microcracks and Recovery of Chloride Transport Properties

Self-healing of cracked concrete, commonly known as autogenous healing, is an often-studied phenomenon[17,18]. Self-healing is generally attributed to the hydration of previously unhydrated cementitious material, calcite formation, expansion of concrete in the crack flanks, crystallization, closing of cracks by solid matter in water, and closing of cracks by fragments of concrete from the cracks themselves[19]. It is believed that, under certain environmental conditions as well as the presence of adequate concentrations of certain chemical species, the possibility and consistency of self-healing mechanisms greatly depend on crack width[20]. Previous researchers have reported various ranges of maximum crack widths for self-healing to occur in concrete under various environmental exposure conditions. These maximum crack width criteria include: 5 to 10 μm[21], 53 μm[22], 100 μm[23], 150 μm[24], 200 μm[25], 205 μm[26], 300 μm[27]. These current results, despite their wide range, all imply that a tighter crack width is favorable for self-healing to occur

within the crack. However, as discussed earlier, requirements for such tight crack width are difficult to achieve consistently in concrete. This explains why reliable self-healing in most concrete structures has not been observed.

The self-healing phenomenon in ECC at the composite scale under various exposure regimes, including water/air cycle, water/hot air cycle, 90%RH/air cycle, water submersion, and air, have been reported by Lepech and Li (2005)[28], Yang et al. (2005)[18], and Yang (2008)[17]. The chloride exposure regime, however, has not been previously studied. Autogenous self-healing in preloaded ECC specimens, in terms of *recovery of chloride transport properties*, was observed under chloride exposure in Chapter 6. In that study, preloaded ECC beams under different bending deformation levels were subjected to chloride (3% NaCl solution) ponding. As applied deformation increased, the number of cracks in ECC beams increased with unchanged crack width (approximately 50 μm), in contrast with the increased crack width in the control reinforced mortar beams. Having the same or higher magnitude of imposed overall deformation, the ECC beams revealed an effective diffusion coefficient considerably lower than that of the reinforced mortar beams, especially at higher deformation levels. The total chloride concentration profiles perpendicular to the crack path indicated no significant chloride penetration up to 90 days of exposure, even at large imposed deformation (2 mm), for the ECC beams.

The significantly lower diffusion coefficient of cracked ECC beams was attributed to the combined effects of the self-controlled tight crack width as well as the self-healing of microcracks. Distinct white deposits were visible at the crack surfaces after one month of exposure to chloride ponding (Figure 6.15), which effectively blocked the flow path of penetration of chloride ions. It should be noted that a previous water

permeability test found no self-healing in cracked ECC specimens that were submersed in water[29]. The self-healing phenomenon in cracked ECC under chloride exposure can be attributed to the presence of NaCl ions, which promoted leaching of calcium hydroxide[30] into cracks and sealed the cracks. An environmental scanning electron microscope (ESEM) observation of the fractured surface of ECC across a healed crack (Figure 6.16) showed that most of the products seen in the cracks were newly formed C-S-H gels. Calcium hydroxide (CH) and deposited salts were also observed in the crack path. This can be attributed primarily to the high fly ash content, unhydrated cement, and relatively low water-to-binder ratio in the ECC mixture. The continued cement hydration and pozzolanic activity of fly ash caused self-healing of the microcracks, which in turn reduced the ingress of the chloride ions. These observations indicate that microcracks of ECC healed completely after exposure for 30 days to NaCl solution.

The possibility of autogenous self-healing in preloaded ECC specimens exposed to a chloride environment, in terms of *recovery of tensile properties* (tensile strain capacity, Young's modulus and crack width), was not previously understood. To investigate this phenomenon in the present study, ECC coupon specimens were preloaded under uniaxial tension to strain levels of 0.5%, 1.0%, and 1.5% to simulate in-service loading conditions (e.g., vehicle load, prestressing load, restrained shrinkage, thermal load, etc). After applying and removing the load, specimens were exposed to a 3% chloride concentration solution for 1, 2, or 3 months and subsequently reloaded until failure to measure residual tensile properties. The effect of cracking and autogenous healing under combined mechanical loading and chloride exposure was assessed by

measuring the retained stiffness, ultimate tensile strength, and tensile strain capacity, and crack width of ECC.

7.3 Experimental Program

7.3.1 Testing of Composite Properties

An ordinary version of ECC, ECC M45, as investigated in Chapter 6, is also employed in this study. The mix proportions for ECC M45 mixtures are summarized in Table 6.2. The mechanical and geometrical properties of the PVA fibers used in this study are shown in Table 6.3.

The ECC mixture was prepared in a standard concrete mixer according to the following sequence: the cement, fly ash and sand were first mixed for one minute; water and HRWR were then slowly added and mixed for an additional two minutes until the cementitious material obtained a homogeneous state; finally, the fibers were added and mixed for two-three minutes until maximum uniformity of fiber dispersion was achieved. This mixture was cast into 152.4×76.2×12.7 mm coupon specimens for the direct uniaxial tensile test. The specimens were covered with plastic sheets and demolded after 24 hours. Then they were first cured in plastic bags at 95±5% RH, 20±1 °C (66-70 °F) for 6 days, and then left to cure in laboratory air under uncontrolled humidity 45 ± 5% RH and temperature 20±1 °C (66-70 °F) conditions until the age of 28 days for testing.

The magnitude of initial and recovered mechanical properties was measured under uniaxial tensile loading. First, deliberate damage was introduced by tensioning the coupon specimens to predetermined strain levels of 0.5, 1.0 and 1.5% followed by unloading, before exposure to 3% NaCl solution. A servohydraulic testing system was

used in displacement control mode to conduct the tensile test. The loading rate used was 0.0025 mm/s to simulate a quasi-static loading condition. Aluminum plates were glued both sides at the ends of coupon specimens to facilitate gripping. Two external linear variable displacement transducers were attached to the specimen to measure the specimen deformation. Typical stress-strain curves of the preloaded specimens are shown in Figure 7.2.

The precracked ECC specimens were then continuously immersed in a 3% NaCl solution at room temperature, together with some uncracked specimens (as control) that were not subjected to preloading, for 30, 60 or 90 days, respectively. The sodium chloride solution was replaced with a fresh solution every month. Subsequently, the specimens were reloaded in direct tension and stress-strain curves were recorded. In the case of uncracked specimens, the average strain capacity and ultimate strength of ECC were averaged from four specimens. In the case of precracked specimens, the average strain capacity and ultimate strength of ECC were calculated from a minimum of four and maximum of six specimens. The tensile properties were then compared with those measured before damage and with those after damage but before potential self-healing took place.

7.3.2 Measurement of MicroMechanical Parameters

To understand the potential effects of chloride exposure on ECC matrix and fiber/matrix interfacial properties at the micromechanical scale, matrix fracture toughness test and single fiber pullout tests were conducted. Based on the conditions for strain-hardening and saturated multiple-cracking, high tensile strain capacity requires a high

J_b'/J_{tip} ratio. The matrix toughness J_{tip} and flaw size distribution are matrix properties, while the complementary energy J_b' is mainly controlled by fiber and interface properties.

To measure the J_{tip}, matrix toughness tests were conducted on the ECC matrix (without fibers) before and after exposure to 3% NaCl solution for 30, 60 and 90 days, respectively. This test was similar to ASTM E399 "Standard Test Method for Plane-Strain Fracture Toughness of Metallic Materials". The ASTM E399 allows one to use different geometry specimens, such as bending specimens and compact tension specimens, to measure the K_m value. The fresh mix was cast into notched beam specimens measuring 305 mm (12 in.) in length, 76 mm (3 in.) in height, and 38 mm (1.5 in.) in thickness. The ECC matrix specimens were then demolded in 24 hours, and cured just as the composites tensile specimens, except that fibers were not added. Four different curing conditions were employed for these beam specimens after being demolded in 24 hours: (a) 28-day curing in air, (b) 28-day curing in air + 30-day curing in 3% NaCl solution, (c) 28-day curing in air + 60-day curing in 3% NaCl solution, and (d) 28-day curing in air + 90-day curing in 3% NaCl solution. The matrix fracture toughness K_m was measured by the three point bending test, as shown in **Figure 2.15**. The span of support is 254 mm (10 in.) and the notch depth to height ratio is 0.4. Three specimens were tested for each test series. J_{tip} was calculated from the measured K_m through Equations 2.1 and 2.2.

To calculate J_b' of the ECC mix with different curing conditions, single fiber pullouts tests were conducted to measure three important interfacial parameters: chemical bond strength G_d, frictional bond strength τ_0, and slip hardening coefficient β. As shown in **Figure 2.16**, single fiber pull-out tests were conducted on small-scale prismatic

specimens with dimensions of 10 mm × 5 mm × 0.5 mm (0.4 in. ×0.2 in. ×0.02 in.). A single fiber was aligned and embedded into the center of an ECC mortar prism with an embedment length of 0.5 mm (0.02 in.). Four different curing conditions were employed for these prismatic specimens after being demolded in 24 hours: (a) 28-day curing in air, (b) 28-day curing in air + 30-day curing in 3% NaCl solution, (c) 28-day curing in air + 60-day curing in 3% NaCl solution, and (d) 28-day curing in air + 90-day curing in 3% NaCl solution. Three specimens were tested for each test series. The load versus displacement curve was obtained through quasi-static testing and used to determine the interfacial parameters. These interfacial parameters, along with fiber volume fraction, length and diameter, were then used to calculate the fiber bridging law $\sigma(\delta)$. The resulting complimentary energy J'_b calculated from the $\sigma(\delta)$ curve combined with the matrix fracture toughness J_{tip} obtained from the K_m measurement were used as inputs to evaluate composite material behavior (i.e. strain-hardening or tension-softening) and to calculate the PSH (pseudo strain hardening, J'_b/J_{tip}) index as defined in Equation 2.4.

7.4 Experimental Results and Discussion

Table 7.1 summarizes the tensile strain capacity, tensile strength, crack width of ECC with various preloaded strain values, and NaCl exposure conditions. Typical tensile stress-strain curves obtained for specimens before and after exposure to the NaCl solution are shown in Figure 7.3. For the uncracked specimens that were not preloaded, exposure to NaCl appears to reduce the cracking strength and ultimate strength by approximately 10%. However, the tensile strain capacity does not appear to be affected after 30, 60, and 90 days of chloride exposure. Multiple microcracking behavior is retained after 30, 60,

and 90 days of chloride exposure, while the average crack width increased from 45 μm (w/o chloride exposure) to 100 μm (w/ chloride exposure). Exposure to chloride appeared to similarly affect the precracked specimens; applied tensile strain up to 1.5% did not exacerbate the deterioration.

Figure 7.3 also shows the tensile properties of ECC specimens that had been precracked to 0.5, 1.0 and 1.5% strain levels, then unloaded and reloaded 1 day after precracking. Thus, these specimens had no time to undergo the crack healing as compared to those specimens exposed to NaCl solution for 30, 60 and 90 days. Compared to the latter, the reloaded specimens without possible self-healing exhibited a remarkable loss in initial stiffness, which is defined by the initial linear part on the stress-strain curve. This can be explained by the initial low load resistance of the existing microcracks. After initial microcracks formed in the precracked ECC specimen, reloading the same specimen will simply re-open the already-formed microcracks until the crack widths initially reached before unloading are reached again and the fiber-bridges re-engage. At first, re-opening these initial microcracks without fiber-bridging behavior resulted in low initial stiffness of the ECC material. Once fiber bridging was re-engaged, however, the load capacity resumed, and further tensile straining of the intact material could take place.

In contrast, a significant recovery of the initial material stiffness was found in the precracked ECC specimens after they were exposure to chloride solution for 30, 60, and 90 days and then reloaded. This suggests that between the time of inducing precracking and the time of reloading, healing of the microcracks took place in the ECC specimens after exposure to NaCl solution. After crack healing, reloading then stressed the rehealed

products in the microcracks. Self-healing can be attributed primarily to the availability of unhydrated cement due to the high cementitious material (cement and fly ash) content and relatively low water to binder ratio within the ECC mixture. As a result of the formation of microcracks due to mechanical loading, unhydrated cementitious particles were easily exposed to the sodium chloride solution during the immersion period, which led to further initiation of hydration processes. The newly formed products not only physically sealed the microcracks, but also recovered the fiber-bridging mechanism by re-forming the fiber/matrix interfacial bond at the microcracks, and thus restored the composite tensile properties.

The ultimate tensile strength values are shown in Figure 7.4. Compared to control specimens cured in laboratory air, the test results indicate that the specimens (precracked and uncracked) immersed in sodium chloride solution show a 10% reduction in ultimate tensile strength for all exposure ages; this should be attributed to the effects of calcium hydroxide leaching on the fiber/matrix interfacial bond and fiber bridging capacity. Water not saturated with calcium hydroxide (high-calcium hydrated lime) may affect test results due to leaching of lime from the test specimens[31]. Presence of chloride ions, especially, tends to increase the leaching of calcium and opening of the porosity of the cementitious matrix[32,33].

Figure 7.5 shows the average tensile strain capacity of ECC specimens stored in NaCl solution. The tensile strain capacity reported for these specimens does not include the residual strain from the precracking load. By neglecting this residual strain, the large variability in material relaxation during unloading was avoided, and a conservative estimate of ultimate strain capacity of the material was determined. The tensile strain

capacity of uncracked and precracked ECC specimens exposed to NaCl solution averaged between 2.4% and 3.8%. This value is higher than or similar to that of air cured specimens (averaging 2.5% to 2.8%).

The influence of chloride exposure on non-preloaded ECC tensile properties can be explained by the influence of chloride exposure on the microstructure of ECC. Based on the measurements of the micromechanical parameters, a reduction in matrix fracture toughness (Figure 7.6) was found after the specimens were exposed to chloride solution for 30, 60 and 90 days, compared to no exposure to chloride solution. The reduction in ECC matrix fracture toughness, very probably due to the leaching of calcium hydroxide in the cementitious matrix to the NaCl solution and the corresponding increase in matrix porosity, explained the reduction in ECC composite first cracking strength. Additionally, from Figure 7.7 and 7.8, despite the large error bar typical of this type of test, it was observed that both the interfacial chemical bond G_d and frictional bond τ_0 tend to be reduced after 30, 60 and 60 days of exposure to 3% NaCl solution. The reduction in the fiber/matrix interfacial bonds can be due to the leaching of calcium hydroxide and increased porosity (less dense) at the fiber/matrix interfacial transition zone, and potential presence of chloride ions and moisture at the interface that might harm the interfacial bonds. The reduction in interfacial bonds explained the increase in the crack width in ECC composites from less than 45 μm before chloride exposure, to approximately 100 μm before 30, 60 or 90 days chloride exposure. Furthermore, the reduction in interfacial bonds also led to a decrease in fiber bridging capacity, resulting in the reduction (approximately 10%) in ECC composite ultimate tensile strength.

The calculated PSH index, J'_b/J_{tip}, is shown in Figure 7.9. Interestingly, it was found that the PSH index increased from 2.3 (before exposure to 3% NaCl solution), to 2.8 (30-day exposure to 3% NaCl solution), 3.1 (60-day exposure to 3% NaCl solution), and 2.7 (90-day exposure to 3% NaCl solution). This indicates that after different time-lengths of severe chloride exposure, the PSH index increased rather than declined. This clarified the underlying micromechanical mechanism of the maintenance of tensile strain capacity of ECC composites after 30, 60, and 90 days of severe chloride (3% NaCl solution) exposure. Such a mechanism does not exist in traditional concrete materials, because the leaching of calcium hydroxide only impairs concrete mechanical properties and promotes potential concrete deterioration[32,33].

7.5 Conclusions

This study revealed that ECC maintained its unique tensile ductility and multiple microcracking behavior under combined mechanical loading conditions (0.5%, 1.0%, 1.5% tensile straining and reloading to failure) and aggressive chloride exposure (30-day, 60-day, and 90-day immersion in 3% NaCl solution). This indicated that even under severe marine environment conditions, ECC remains durable and can provide reliable tensile ductility to prevent common cracking failure due to restrained volume change or stress concentration. Additionally, its self-controlled microcrack width during the strain-hardening stage can offer reliable resistance to chloride penetration, even in a severe marine environment. Although the average crack width of ECC increases from 45 μm to 100 μm, it is still below the maximum crack width limit for marine environments.

The innately tight crack width in ECC is favorable for the self-healing process to take place. This was demonstrated in this study in terms of recovery of tensile behavior, especially material initial stiffness. Specimens preloaded with up to 1.5% strain capacity showed almost complete recovery of stiffness and tensile strain capacity when reloaded in direct tensile tests, even after periods of 30, 60, and 90 days exposure to NaCl solution.

It was also found that both precracked and uncracked ECC specimens exposed to NaCl solution lost approximately 10% of their first cracking strength and ultimate tensile strength. Furthermore, average crack width during reloading increased from 45 μm (exposed to air) to 100 μm (exposed to chloride solution). These phenomena, observed at the composite scale, suggested possible changes in the fiber/matrix interfacial bond properties at the microscale due to chloride exposure. It was suspected that presence of chloride ions promoted the leaching of calcium hydroxide, and consequently increased porosity in the cementitious matrix and the fiber/matrix interfacial transition zone. Through investigation on ECC microparameters, reductions in matrix fracture toughness, fiber/matrix interfacial chemical bond and frictional bond, were observed after exposure to 3% NaCl solution for 30, 60, and 90 days, compared to those without the chloride exposure. However, the PSH index, J'_b/J_{tip}, slightly increased. These changes in matrix and fiber/matrix properties due to exposure to 3% NaCl solution explained the reduction in first-cracking strength and ultimate tensile strength, increase in crack width during the strain-hardening stage, and the maintained tensile strain-hardening behavior and tensile strain capacity.

Table 7.1 – Tensile properties of ECC under different combinations of preloading and chloride exposure conditions.

Environmental Exposure Condition	Preloaded Strain (%)	Tensile Strain Capacity (%)	Ultimate Tensile Strength (MPa)	Average Crack Width (μm)
28 days air + 30 days air or NaCl	0.0 (Air curing)	2.86 ± 0.58	4.81 ± 0.64	~ 45
	0.0 (3% NaCl)	2.79 ± 0.54	4.34 ± 0.62	~ 100
	0.5 (3% NaCl)	3.85 ± 0.61	4.59 ± 0.29	~ 100
	1.0 (3% NaCl)	2.66 ± 0.66	3.85 ± 0.09	~ 100
	1.5 (3% NaCl)	2.48 ± 0.94	3.87 ± 0.73	~ 100
28 days air + 60 days air or NaCl	0.0 (Air curing)	2.51±0.19	4.75 ± 0.45	~ 35
	0.0 (3% NaCl)	2.37±0.50	4.25 ± 0.47	~ 100
	0.5 (3% NaCl)	3.16±0.26	4.05 ± 0.47	~ 100
	1.0 (3% NaCl)	3.28± 0.42	4.18 ± 0.22	~ 100
	1.5 (3% NaCl)	2.97± 0.69	4.07 ± 0.47	~ 80
28 days air + 90 days air or NaCl	0.0 (Air curing)	3.02 ± 0.60	4.64 ± 0.32	~ 30
	0.0 (3% NaCl)	3.27 ± 0.76	4.41 + 0.45	~ 100
	0.5 (3% NaCl)	3.22 ± 0.39	4.70 ± 0.35	~ 100
	1.0 (3% NaCl)	2.61 ± 0.12	4.12 ± 0.17	~ 80
	1.5 (3% NaCl)	2.96 ± 0.87	4.12 ± 0.17	~ 90

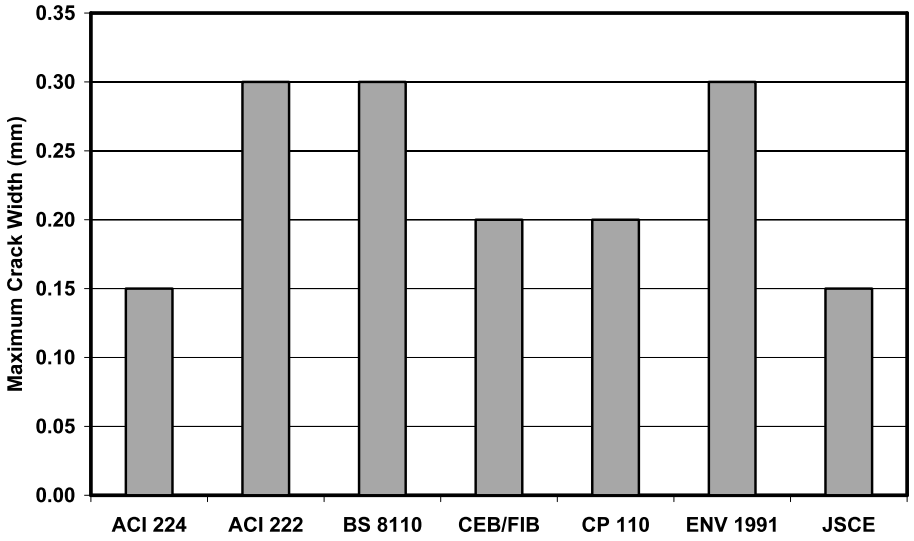

Figure 7.1 – Comparison of allowable crack widths under marine exposure.

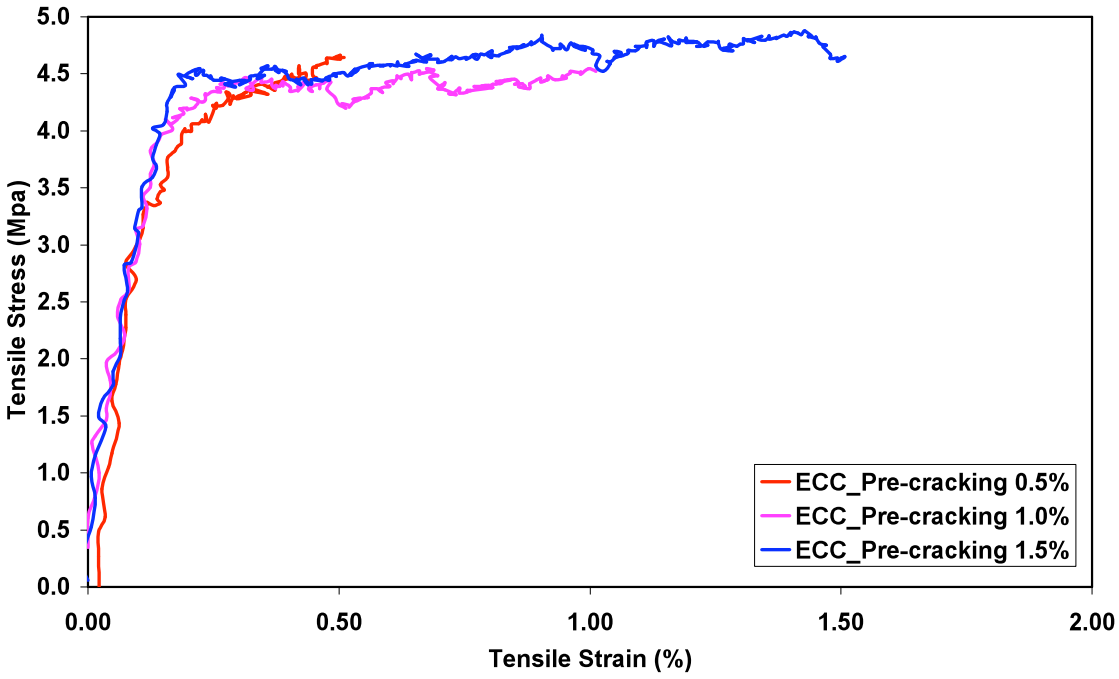

Figure 7.2 – Typical precracking tensile stress-strain curves of ECC.

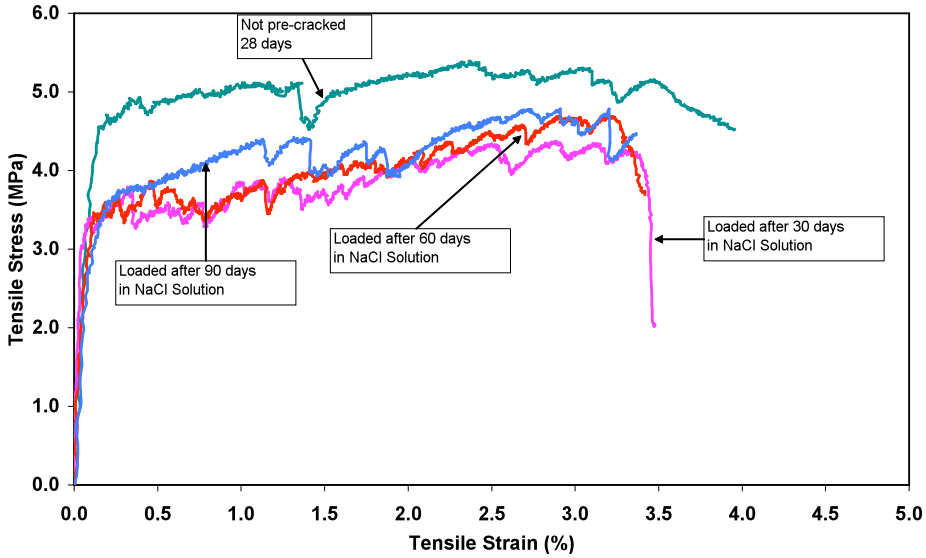

(a) Not preloaded (precracked)

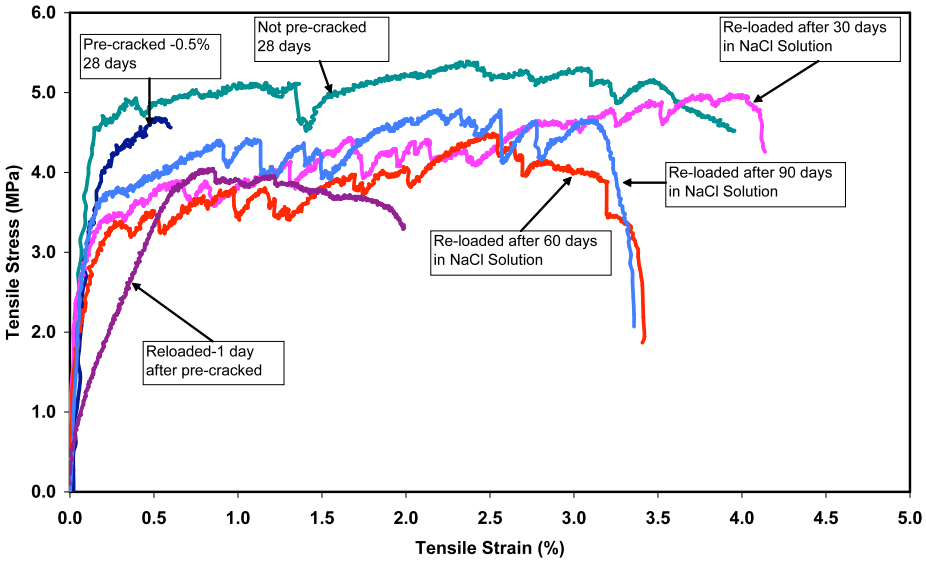

(b) Precracked to 0.5% tensile strain

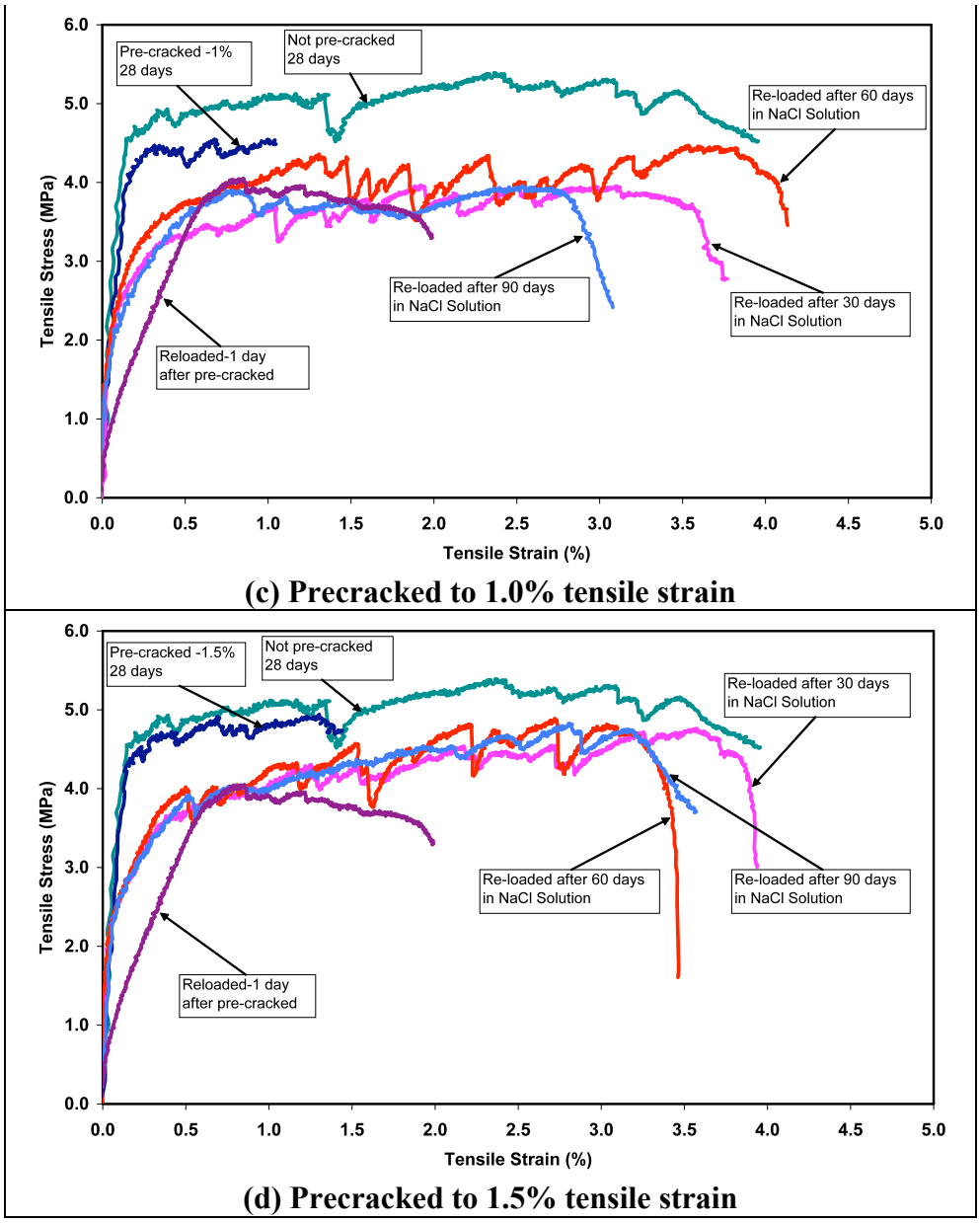

Figure 7.3 – Tensile stress-tensile strain curves of ECC specimens before and after exposure to 3% NaCl solution. (a) Not preloaded (precracked). (b) Precracked to 0.5% tensile strain. (c) Precracked to 1.0% tensile strain. (d) Precracked to 1.5% tensile strain.

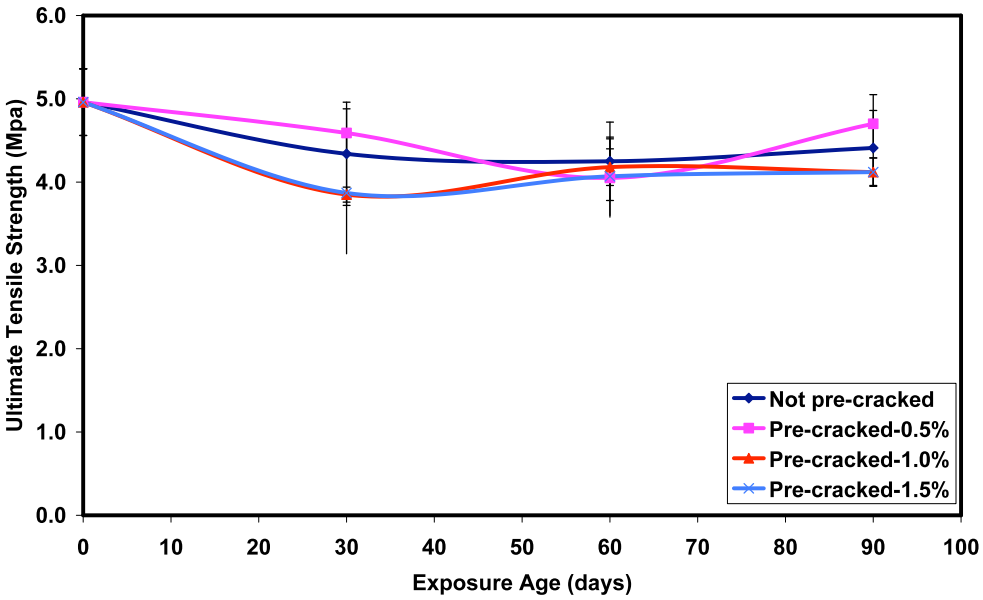

Figure 7.4 – Influence of NaCl exposure time and applied strain level on ECC ultimate tensile strength.

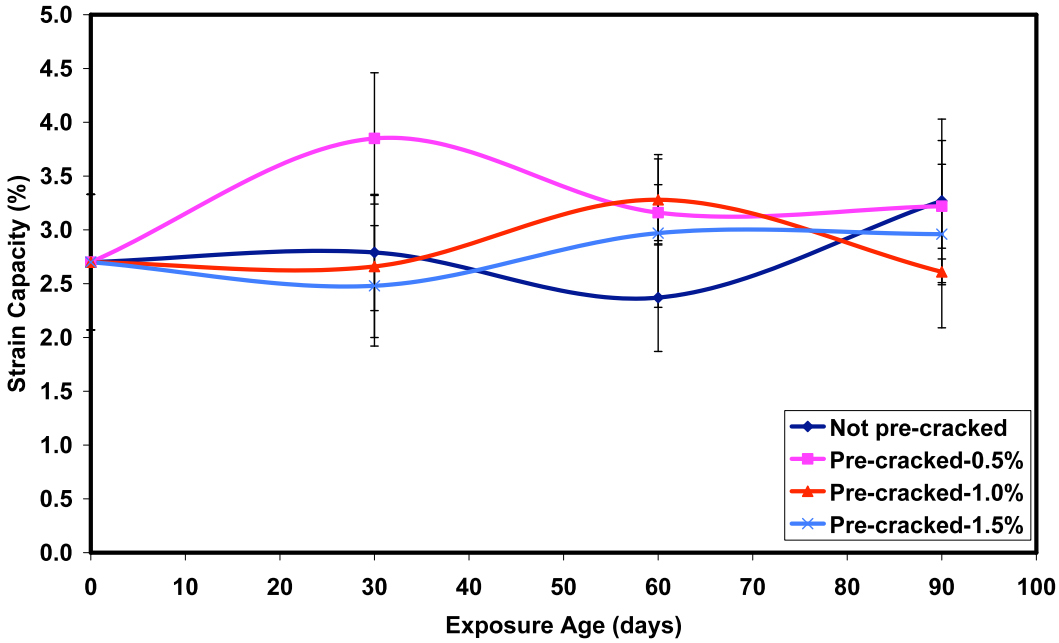

Figure 7.5 – Influence of NaCl exposure time and applied strain level on ECC tensile strain capacity.

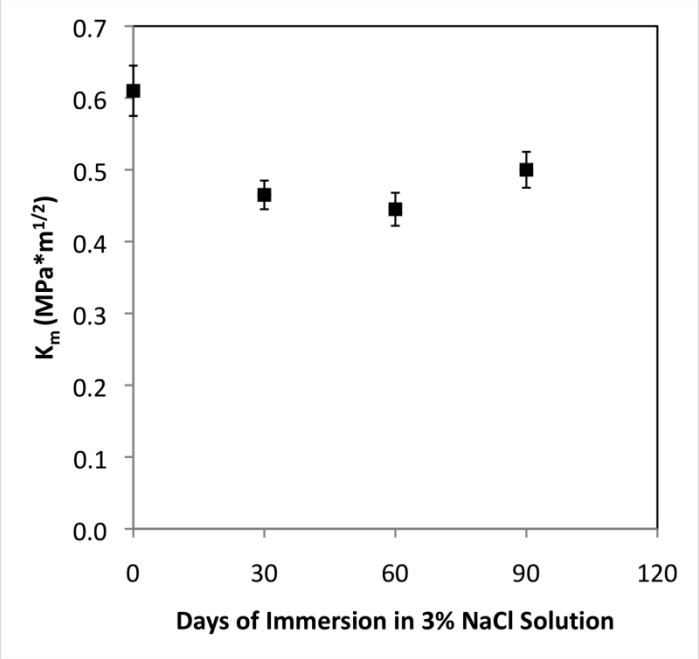

Figure 7.6 – Influence of NaCl solution exposure time on ECC matrix fracture toughness.

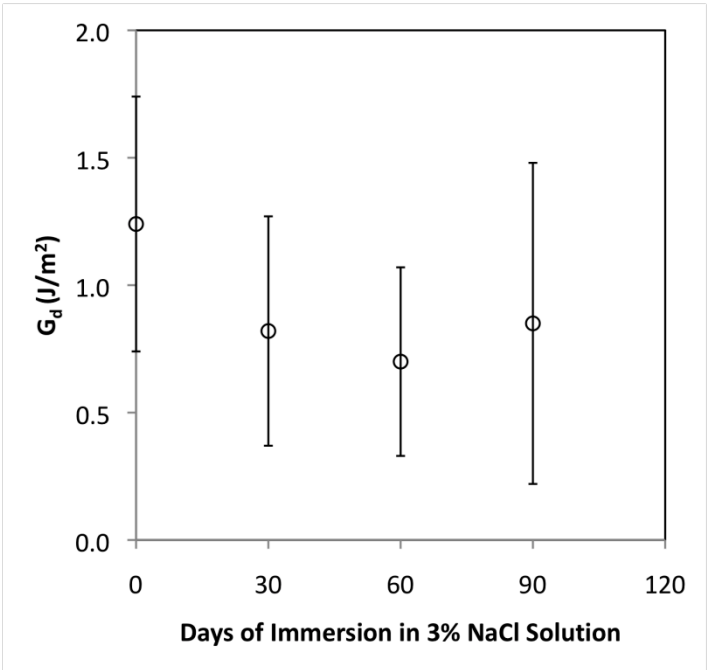

Figure 7.7 – Influence of NaCl solution exposure time on ECC matrix/fiber interfacial chemical bond.

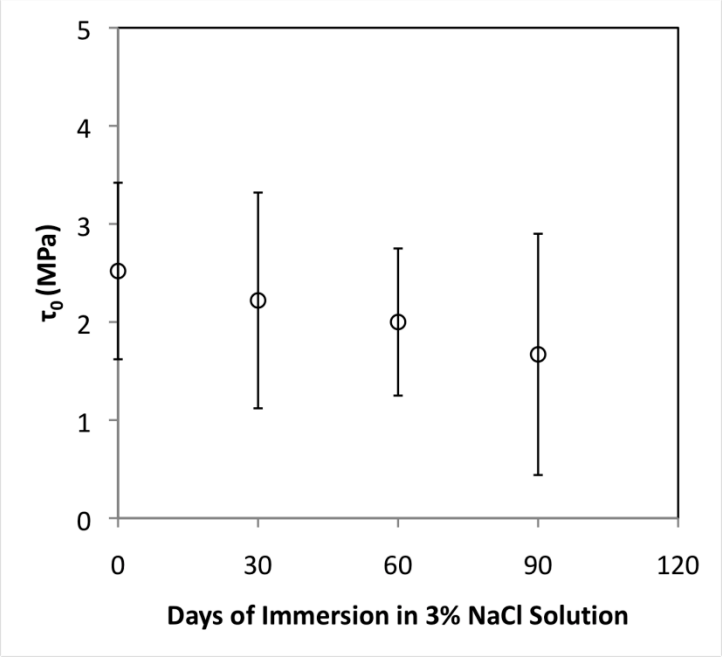

Figure 7.8 – Influence of NaCl solution exposure time on ECC fiber/matrix interfacial frictional bond.

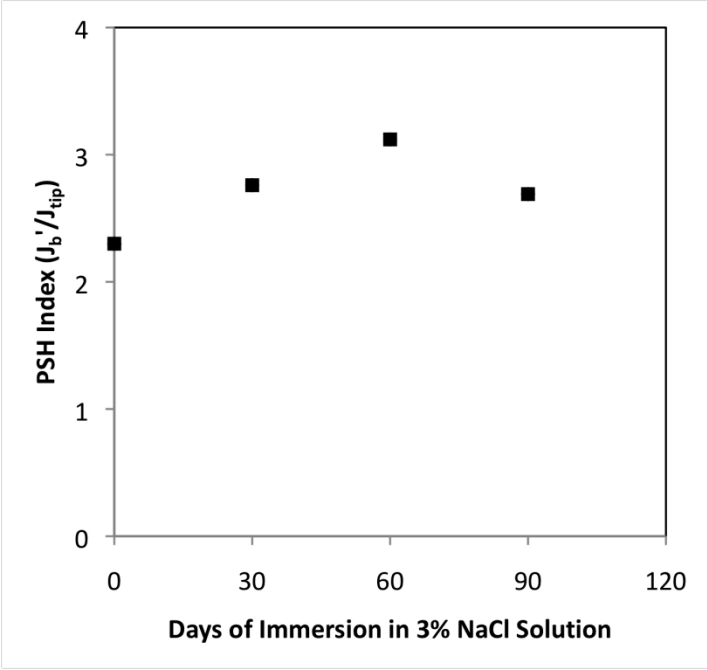

Figure 7.9 – Influence of NaCl solution exposure time on ECC PSH Index.

References:

[1] ACI Committee 224R-2001, "Control of Cracking in Concrete Structures," *ACI Manual of Concrete Practice, Part 3*, American Concrete Institute, Farmington Hills, Michigan, 2001.

[2] Tsinker, G. P., *Marine Structures Engineering: Specialized Applications*, 1995, pp. 548.

[3] Mehta, P. K., and Gerwick, B. C., "Cracking-Corrosion Interaction in Concrete Exposed to Marine Environment," *Concrete International*, Vol. 4, No. 10, pp. 45-51.

[4] Gilbride, P., Morgan, D. R., Bremner, T. W., "Deterioration and Rehabilitation of Berth Faces in Tidal Zones at the Port of Saint John," *Shortcrete*, Fall 2002, pp. 32-38.

[5] Mehta, P. K., "Durability of Concrete Exposed to Marine Environment – A Fresh Look," *ACI Special Publication*, Vol. 19, 1988, pp. 1-30.

[6] Liu, P. C., "Damage to Concrete Structures in a Marine Environment," *Materials and Structures*, Vol. 24, 1991, pp. 302-307.

[7] ACI Committee 224R-2001, "Control of Cracking in Concrete Structures," *ACI Manual of Concrete Practice, Part 3*, American Concrete Institute, Farmington Hills, Michigan, 2001.

[8] British Standards Institution. BS 8110: Pt.1, BSI, London, 1997.

[9] CEB-FIP Model Code 1990, CEB Information Report No. 213/214, *Comite Euro-International DuBeton*, Lausanne, May 1993.

[10] Code of Practice for the Structural Use of Concrete - Part 1. Design, Materials and Workmanship, British Standards Institution Publication CP 110, London, England, November 1972 (Amended May 1977).

[11] Standard Specification for Design and Construction of Concrete Structures - 1986, Part 1 (Design), Japan Society of Civil Engineers, SP-1, Tokyo, Japan, 1986.

[12] ACI Committee 222, "Corrosion of Metals in Concrete," *ACI 222R-89*, American Concrete Institute, Detroit, Michigan, 1975.

[13] Markeset, G. Rostam, S., and Klinghoffer, O., "Guild for the Use of Stainless Steel Reinforcement in Concrete Structures," *Project Report 405, Nordic Innovation Center Project – 04118: Corrosion Resistant Steel Reinforcement in Concrete Structures (NonCor)*, 2006, p. 59.

[14] Baysburd, A. M., Emmons, P. H., Mailvaganam, N. P., McDonald, J. E., and Bissommette, B., "Concrete Repair Technology – A Revised Approach is Needed," *Concrete International*, Vol. 26, No. 1, Jan. 2004, pp. 58-65.

[15] Cusson, D., and Mailvaganam, N., "Durability of Repair Materials," *Concrete International*, Vol. 18, No. 3, Mar. 1996, pp. 34-38.

[16] Grzybowski, M., and Shah, S. P., "Shrinkage Cracking of Fiber Reinforced Concrete," *ACI Materials Journal*, Vol. 87, No. 2, Mar.-Apr. 1990, pp. 138-148.

[17] Yang, E. H., "Designing Added Functions in Engineered Cementitious Composites," *Ph.D. Dissertation*, The University of Michigan, 2008.

[18] Yang, Y. Z., Lepech, M. D., and Li, V. C., "Self –Healing of Engineered Cementitious Composites under Cyclic Wetting and Drying," *Proc. Int. Workshop on Durability of Reinforced Concrete under Combined Mechanical and Climatic Loads (CMCL)*, Qingdao, China, Oct. 2005, pp. 231-242.

[19] Ramm, W., and Biscoping, M., "Autogenous healing and reinforcement corrosion of water-penetrated separation cracks in reinforced concrete." *Nuclear Engineering and Design,* Vol. 179, 1998, pp. 191-200.

[20] Li, V. C., and Yang, E. H., "Self Healing in Concrete Materials," *Self Healing Materials: An Alternative Approach to 20 Centuries of Materials*, by Sybrand van der Zwaag, 2007, pp. 160-194.

[21] Jacobsen, S., Marchand, J., and Homain, H., "SEM Observations of The Microstructure of Frost Deteriorated and Self-healed Concrete," *J. of Cement and Concrete Research*, Vol. 25, 1995, pp. 1781-1790.

[22] Ismail, M., A.Toumi, R. Francois, and R. Gagne, "Effect of crack opening on local diffusion of chloride inert materials," *Cement and Concrete Research*, Vol. 34, 2004, pp. 711-716.

[23] Reinhardt, H., Joos, M., "Permeability and Self-healing of Cracked Concrete as a Function of Temperature and Crack Width," *J. of Cement and Concrete Research*, Vol. 33, 2003, pp.981-985.

[24] Sahmaran, M., Li, M., and Li, V.C., "Transport Properties of ECC under Chloride Exposure," accepted*, ACI Materials J.*, 2007.

[25] Edvardsen, C., "Water Permeability and Autogenous Healing of Cracks In Concrete," *ACI Materials J.*, Vol. 96, 1999, pp.448-455.

[26] Aldea, C., Song, W., Popovics, J. S., and Shah, S.P., "Extent of Healing of Cracked Normal Strength Concrete," *J. of Materials In Civil Engineering*, Vol. 12, 2000, pp.92-96.

[27] Clear, C.A., "The Effects of Autogenous Healing Upon the leakage of Water through Cracks in Concrete," 1985, p. 28.

[28] Lepech, M.D., and Li, V.C., "Water Permeability of Cracked Cementitious Composites," *ICF 11,* Turin, Italy, Paper 4539 of Compendium of Papers CD ROM, 2005.

[29] Lepech, M.D., "A Paradigm for Integrated Structures and Materials Design for Sustainable Transportation Infrastructure," *Ph.D. Dissertation*, Department of Civil and Environmental, University of Michigan, Ann Arbor, PhD Thesis, 2006.

[30] Wang, K., Nelsena, D.E., and Nixon, W., "Damaging effects of deicing chemicals on concrete materials," *Cement and Concrete Composites*, Vol. 28, No. 2, 2006, pp.173-188.

[31] ASTM C 511, "Standard Specification for Moist Cabinets, Moist Rooms, and Water Storage Tanks Used in the Testing of Hydraulic Cements and Concretes," *American Society for Testing and Materials*, West Conshohocken, PA, Vol. 4, No. 2, 2002.

[32] Delagrave, A., Pigeon, M., Marchand, J., and Revertegat, E., "Influence of chloride ions and pH level on the durability of high performance cement pastes (Part II)," *Cement and Concrete Research*, Vol. 26, No. 5, May 1996, pp. 749-760.

[33] Wang, K., Nelsen, D. E., and Nixon, W. A., "Damaging Effects of Deicing Chemicals on Concrete Materials," *Cement and Concrete Composites*, Vol. 28, No. 2, February 2006, pp. 173-188.